D12.1 – TEST REPORT

Version 1.0

28.07.2021

Status: Draft

Deliverable

H2020 INFRADEV-01-2017 project "European Stratospheric Balloon Observatory *Design Study*"

Topic: INFRADEV-01-2017 Design Studies

Project Title: European Stratospheric Balloon Observatory *Design Study* – ESBO *DS*

Proposal No: 777516 – ESBO DS

Duration: Mar 1, 2018 - Feb 28, 2021

WP	WP 12
Del. No	D12.1
Title	Test Report
Lead Beneficiary	"USTUTT"
Nature	"Report"
Dissemination Level	"Public"
Est. Del. Date	31/07/2021
Version	1.0
Date	28.07.2021
Status	Draft
Lead Author	ESBO *DS* Team
Approved by	

TABLE OF CONTENTS

LIST OF ABBREVIATIONS AND DEFINITIONS

Abbreviation	Definition
ACU	Attitude Control Unit
ADCS	Attitude Determination and Control System
FEM	Finite Element Method
GPS	Global Positioning System
ISS	Image Stabilisation System
MLI	Multi-Layer Insulation
OBC	On-Board Computer
OBSW	On-Board Software
OTA	Optical Tube Assembly
P/L	Payload
PCDU	Power Control & Distribution Unit
STUDIO	Stratospheric Demonstrator of an Imaging Observatory
TBC	To be confirmed
TBD	To be determined
TCP/IP	Transmission Control Protocol/Internet Protocol
TIP	Telescope Instruments Platform
TM/TC	Telemetry/Telecommand
TV	Thermal-Vacuum
UV	Ultraviolet

REFERENCE DOCUMENTS

[RD1]	STUDIO Verification and Test Matrix, STU-IRS-A-LIS-820-01-R01-Verification-and-Tests_2020-07-24.xls
[RD2]	ECSS-E-ST-10-03C, Space Engineering – Testing, 1 June 2012
[RD3]	STUDIO Product Breakdown Structure, STU-IRS-A-LIS-000-01-R06-Product-Breakdown-Structure_2020-09-14.xlsx
[RD4]	STUDIO Product Breakdown Structure visualization, highest levels. STU-IRS-A-PBS_2020-09-14.pdf
[RD5]	STUDIO AIT Schedule, STU-IRS-A-LIS-800-01-v1.03_AIT-Schedule_2020-09-15

[RD6]	Officina Stellare, STUDIO Telescope Acceptance Review Plan, OC19031.PLN.ESBO.1000.001.pdf
[RD7]	ECSS-Q-ST-70-02C, Space Product Assurance – Thermal vacuum outgassing test for the screening of space materials, 15 November 2008
[RD8]	STUDIO Shock Test Procedure, STU-IRS-M-PRO-820-02-v1.00_Shock-Test-Procedure.docx

PART 1
General Introduction and Summary

1 INTRODUCTION

This document contains descriptions of tests carried out on the ESBO *DS* prototype platform STUDIO (Stratospheric UV Demonstrator of an Imaging Observatory). It includes detailed descriptions of the set-ups, results, and, where relevant, the detailed procedures.

The descriptions, set-ups, procedures, and results of each test are described in an individual report, keeping them together, and the individual reports are combined in this document. This document therefore consists of two parts: this part 1, summarizing all tests and the overall results and part 2, including all individual test reports.

2 SCOPE AND GOALS

The tests covered in this report primarily include functional tests of prototype subsystems and components as well as simulated operational environment tests.

A description of the general testing approach is included in chapter 3. A detailed list of the tests that were carried out, including information on who carried them out, can be found in chapter 4. An illustration of the test timeline and logic is included in chapter 5.

Chapter 6 includes a general summary of all test results, including conclusions on the approaches taken and on further tests, investigations, or adaptations that might be necessary to achieve the mid- and long-term goals of the project.

3 GENERAL TESTING APPROACH

3.1 VERIFICATION AND TEST APPROACH

STUDIO follows an adapted version of the classical V-model approach (see Figure 1) for testing. Adaptations are particularly made in the sense that the strict components – assemblies – subsystems – system test sequence it not followed everywhere, but that – wherever reasonable – tests of components are combined on assembly or even subsystem level.

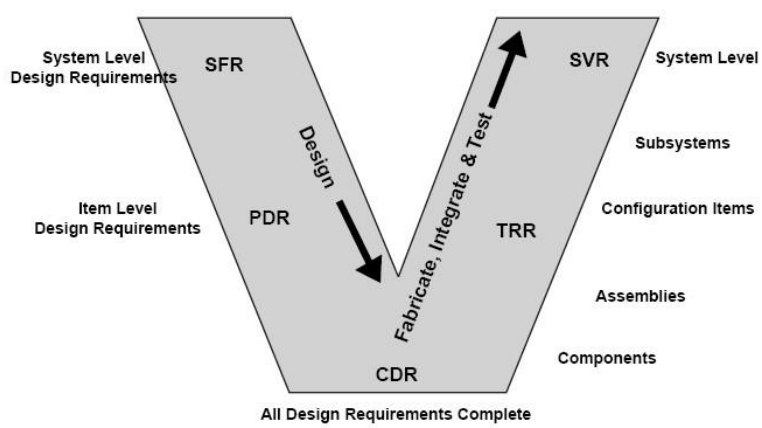

Figure 1: Classical V-model approach for development and testing

3.2 VERIFICATION PLAN AND METHODS

The detailed verification method for all requirements is documented in the STUDIO Verification Matrix [RD1]. The following verification methods are used:

Table 1: Verification methods foreseen for STUDIO

Verification method	Details
Test	Measuring performance & functions under representative simulated conditions
Functional Test	Confirming functional success by simple functional tests
Analysis/Simulation	Based on detailed theoretical or empirical evaluation, including simulation (e.g. FEM analysis of deformations under vibrational or thermal environment, analysis of controller performance)
Design	Verification by design only (e.g. choice of components, technical drawings,...)
(Physical) Inspection	Visual determination of physical characteristics or simple measurement (e.g. mass determination by weighting)

Generally, the qualities as listed in Table 2 are foreseen to be verified via test and inspection. Most other qualities / requirements will be verified by design and analysis.

Table 2: General application of test & inspection

Test / Functional Test	Inspection
• Environmental compatibility / qualification • Instrument & telescope performance • Image Stabilization & Pointing • Thermal Control • Software & OBC • (Electrical) Interface parameters	• Physical parameters (mass, sizes, etc.) • (Physical) Interface Compatibilities

3.3 TEST MODEL APPROACH

3.3.1 Protoflight Approach

A protoflight approach is used as the baseline testing approach for the STUDIO mission. Accordingly, it is foreseen to not have a separate qualification model, but to perform combined qualification and acceptance tests on the flight model itself. Testing levels are therefore chosen such as to not damage the elements / units, but to still provide evidence that the elements / equipment perform in accordance with requirements / specifications in the intended environment (see also [RD2]).

3.3.2 Additional Structural / Functional Models

To support the testing, particularly in order to allow parallel testing of different subsystems and to minimize delays originating from components delivered at later points in the project timeline, the following structural and/or functional models are foreseen:

- Structural telescope assembly model ("telescope mass dummy") for tuning and tests of the gondola attitude determination and control system (ADCS) (at DST Control[1])
- Structural and functional model of M3 for tuning and tests of the Image Stabilization System (at Ingenyo[2])
- Lab model of the tip/tilt platform for laboratory tests and the TIP vibration test
- Structural model of the UV Detector & UV Proximity Electronics ("mass dummy") for the TIP vibration test

3.4 ENVIRONMENTAL QUALIFICATION APPROACH

Environmental qualification will be performed (mostly following the protoflight model approach) via:

- Thermal vacuum tests, and
- Vibration tests.

For these tests, ECSS-adapted procedures[3] are used.

3.4.1 Payload Environmental (Thermal Vacuum) Tests on Component Level

Thermal vacuum tests on component level are foreseen for the following components:

- Visible light (PCO) camera
- Filter wheels
- Star tracker (*done by manufacturer as type test*)
- Tip-tilt actuator (*done by manufacturer as type test*)
- M2 motors (*considered qualified from previous flights*)
- Power Conversion Board
- Environmental Measurement Board
- M2 motor control electronics

3.4.2 Payload Environmental (Thermal Vacuum) Tests on Assembly Level

Thermal vacuum tests on assembly level, or in combination with other tests, are foreseen for the following components/assemblies:

- Visible camera cooling (combined with TIP thermal vacuum test)
- TIP (combined with optical alignment test)
- Electronics in pressure housing

3.4.3 Payload Environmental (Vibration) Test

A single vibration test (with 5 g loads) is foreseen for the integrated payload and electronics. The test does not include the UV instrument. In case of the UV instrument EKUT will perform own

[1] https://www.dst.se/, subcontractor of SSC for the pointing system

[2] http://www.ingenyo.es/, subcontractor of IAA for the Image Stabilization System

[3] Procedures used for STUDIO are designed based on the requirements, conditions, and test processes (where appropriate, adapted) as laid out in [RD2]. For the thermal vacuum test, this particularly concerns section 5.5.4.2 and table 5-6, no. 11 in [RD2]. For the shock test, this particularly concerns section 5.5.2.6 and table 5-6, no. 7.

tests, the detector is shock resistant by design and should be spared from further shock tests. This test will be followed by an alignment verification of the optical system.

3.5 CONTAMINATION AND CLEANLINESS

Contamination of the optical surfaces can cause serious straylight (particularly in the UV) and therefore degradation of the scientific observations in the UV. The optical compartment (inside of telescope tube, inside of TIP) therefore needs to be protected from contamination. The following general rules apply:

- Work on the (flight hardware) optical components and on the optical compartment shall only be carried out under clean room conditions according to cleanroom class ISO 6 (corresponding to the former cleanroom class 1,000);
- When work has to be performed with the telescope assembly or the TIP (or parts thereof, e.g. for on-sky pointing tests), or either of them has to be transported, they shall be sealed to prevent contamination;
- Components that were previously exposed to less clean environments shall be cleaned before being installed in the optical compartments;
- Contamination control may require bakeout of materials (e.g. of non-reflective paint).

4 TESTS RELEVANT TO THIS DOCUMENT

The tests relevant to this document are summarized in Table 3, including information on the institution that carried out the test and the location where the tests were carried out.

Table 3: Prototype tests covered in/mentioned in this test report

Test	Carried out by	Carried out at/in
Functional Tests		
Visible camera optical quality test	USTUTT/EKUT	Stuttgart/Tübingen, Germany
Non-reflective paint functional and outgassing tests[4]	USTUTT/EKUT	Stuttgart/Tübingen, Germany
Laboratory Image Stabilization System tests	IAA/Ingenyo	Malaga, Spain
Image Stabilization System Simulations	USTUTT	Stuttgart, Germany
Telescope Acceptance Tests[5]	Officina Stellare	Sarcedo, Italy
ISS Integrated Performance Test	IAA/Ingenyo/USTUTT	Stuttgart, Germany
Payload interface equipment functional test	USTUTT	Stuttgart, Germany
Environmental Tests		
Filter wheels thermal vacuum tests	USTUTT	Stuttgart

[5] Confidential, not part of this document

Visible camera thermal vacuum tests	USTUTT	Stuttgart
TIP Shock Test	USTUTT	Stuttgart, Germany
Solar panel thermal tests	SSC	Solna, Sweden

5 TEST LOGIC / SEQUENCE

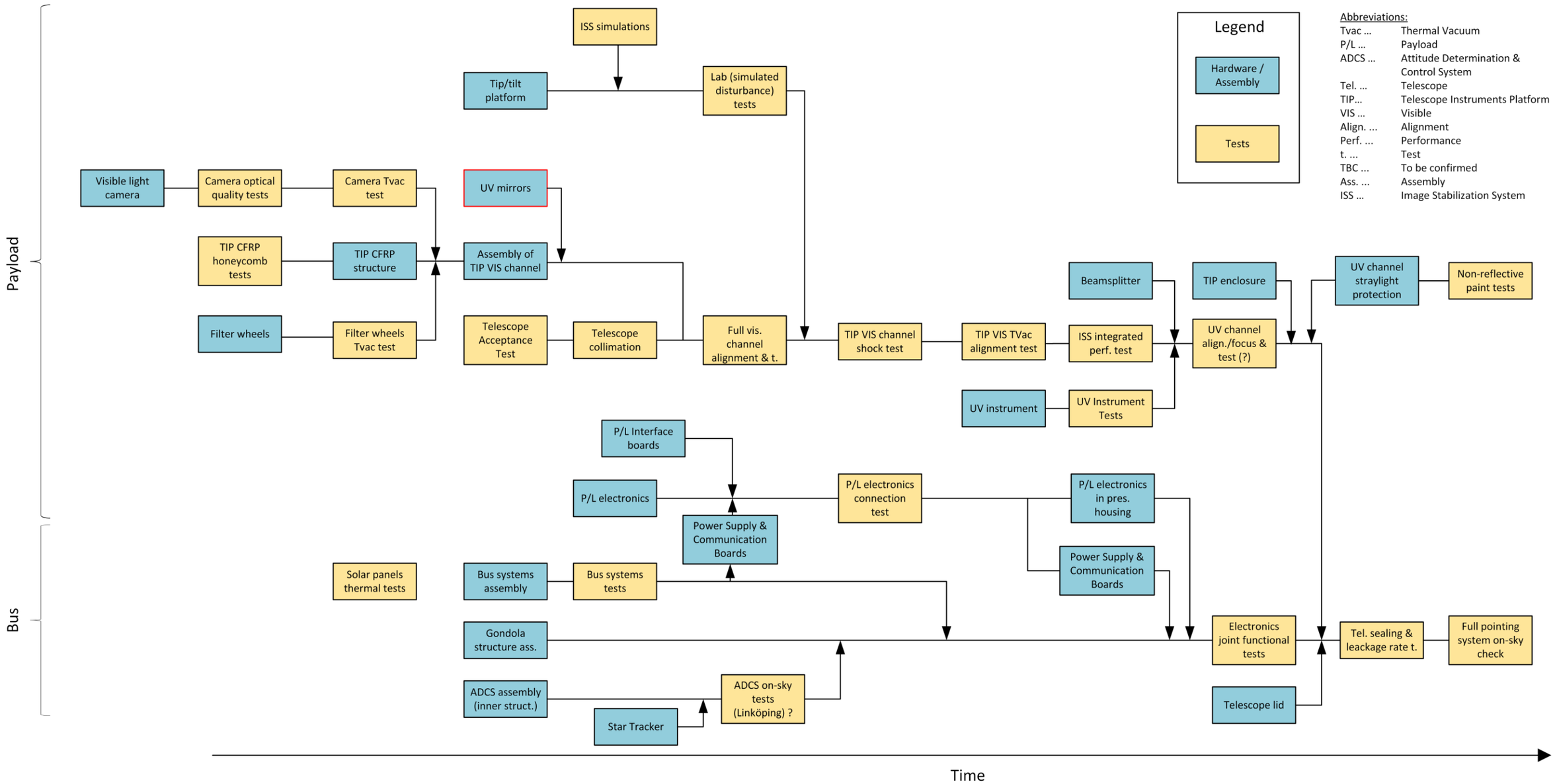

6 OVERALL SUMMARY OF TESTS

Image Stabilization

- Lab performance and simulations look promising, however, there are a couple of shortcomings and open points still to be investigated:
    - Guide star tracking accuracy on faint sources with the currently implemented centroid tracking misses the original requirement. Re-analysis of the data shows, however, that the centroid tracking algorithm itself is suitable and that minor changes in the image pre-processing improve the accuracy sufficiently to meet the requirement. The adjusted image processing still has to be implemented on the frame grabber FPGA where centroid tracking is carried out.
    - Simulations so far have been carried out based on flight disturbance data measured on a slightly different gondola. Calibration and final validation during flight will therefore be necessary.
    - Combined tests of the image stabilization system with the gondola pointing system are still outstanding.

Use of Commercial-off-the-Shelf (COTS) equipment

- Experience with using COTS has been very good. Critical aspects (particularly thermal behaviour and critical mechanical and electronic components) have been identified. A lot of this knowledge can be used to assess the potential suitability of components in the future.
- Several COTS components and materials were tested, particularly including the high-performance sCMOS camera, filter wheels, electronics components (microcontrollers, hubs), and non-reflective paints. On part of them, successful modifications were performed (exchange of bearings, of rubber parts, of capacitors) which can also be used to make other COTS equipment stratosphere-compatible.
- The tests of COTS solar panels showed that regular flexible panels as they are readily available off the shelf are not suitable for balloon applications, mostly because their typical encapsulation is not compatible with the combined high temperature and low pressure environment. Design modifications were carried out in cooperation with a manufacturer, however, leading to an economic and suitable solution.

Development of qualification and test procedures

- Test procedures for thermal vacuum tests & for outgassing tests were developed that can be used generally & that will be made available via the project website.

Bus systems tests

- Functional and interface tests of bus systems and between payload and bus systems were conducted and successful.

Payload vibration test

- The vibration test of the payload optical bench showed no damage to the equipment and resonance frequency analysis indicated no significant movement of optical components.
- Minor design changes were implemented following the test.
- The first resonance frequencies of the M3 tower (holding the tip/tilt platform) were above the requirement but lower than expected from simulations. The vibrational response behaviour of the M3 tower to excitations from the tip/tilt platform will therefore be further monitored.

PART 2
Individual Test Reports

STU-IRS-E-PRO-1230-01-v0.01_TV-Optical Test Results
PCO.Edge 4.2 Camera_2019-11-11

OPTICAL TEST OF PCO.EDGE 4.2 CAMERA

Version 1.0

11.11.2019

Status: Draft

H2020 INFRADEV-01-2017 project "European Stratospheric Balloon Observatory *Design Study*"

Topic: INFRADEV-01-2017 Design Studies

Project Title: European Stratospheric Balloon Observatory *Design Study* – ESBO *DS*

Proposal No: 777516 – ESBO DS

Duration: Mar 1, 2018 - Feb 28, 2021

WP (EU)	WP 10
WBS Item (internal)	650
PBS Item(s)	1200
Title	Optical Test of pco.edge Camera
Description	Optical test and characterization of a pco.edge 4.2
Lead Beneficiary	"USTUTT"
Nature	"Procedure"
Dissemination Level	"Confidential"
Est. Del. Date	-
Version	1.0
Date	11.11.2019
Status	Draft
Lead Author	S. Bougueroua, sbougueroua@irs.uni-stuttgart.de, USTUTT
Approved by	

VERSION HISTORY

Version #	Implemented By	Revision Date	Approved By	Approval Date	Explanation
0.01	Sarah Bougueroua	11/11/2019			First Version

TABLE OF CONTENTS

LIST OF ABBREVIATIONS AND DEFINITIONS

Abbreviation	Definition
ADU	Analog
ESBO-*DS*	European Stratospheric Balloon Observatory – *Design Study*
MPV	Mean Pixel Value
STUDIO	Stratospheric Ultraviolet Demonstrator of an Imaging Observatory

REFERENCE DOCUMENTS

[1] S. Bougueroua, "Optical Test Procedure of the pco.edge 4.2 camera," 2019.

[2] ©PCO AG, "pco.edge 4.2 scientific CMOS camera | v1.03A," Germany.

[3] P. Andreas, "THERMAL VACUUM TEST OF PCO EDGE 4.2 CAMAERA," ESBO DS, 2019.

[4] R. Berry and B. James , The Handbook of Astronomical Processing, Willmann-Bell, Inc, 2005.

[5] M. I. Corporation, *Instruction Manual 7" LX200 Maksutov-Cassegrain Telescope 8", 10", and 12" LX200 Schmidt-Cassegrain Telescopes.*

[6] S. d. Strasbourg/CNRS, "SIMBAD Strasbourg Astronomical Database," 2019. [Online]. Available: http://simbad.u-strasbg.fr/simbad/.

[7] S. Tietz, "Characterization Methods of CCD sensors for the Target Acquisition and Tracking Cameras of Sofia," March 2008.

[8] S. Lombardo, T. Behaghel, B. Chambion, W. Jahn, E. Hugot and & al., "Curved CMOS sensor: characterization of the first fully functional prototype," in *SPIE Photonics Europe*, Strasbourg, France, 2018.

LIST OF FIGURES

SCOPE

This document details the results of the optical test of the pco.edge 4.2 camera (Camera Link version) provided by PCO AG in Kehlheim, Germany.

These tests are part of the ESBO-*DS* project at the University of Stuttgart. ESBO-*DS* (European Stratospheric Balloon Observatory – *Design Study*) is a project conducted by several European partners to evaluate possibilities to observe astronomical targets from a balloon in the stratosphere. The main scientific instrument will observe targets in the ultraviolet regime of the spectrum. In order to mitigate disturbances, an active image stabilization system will take pictures through a camera in the visible regime of the spectrum. The movement of star images from picture to picture will be evaluated and used to mitigate disturbances by moving a fast tip/tilt mirror.

The objective of these tests is to characterize the CMOS sensor of the camera under ambient conditions to verify the performances given in its datasheet by the provider. The sensor is maintained at 5°C using a pump-driven cooling circuit, including a pco.aquamatic II [RD1] pump and innovatek Protect IP coolant [RD2] from also provided by PCO, in addition to hoses of 5mm inner diameter.

The tests were performed in the optics laboratory at the IRS, University of Stuttgart. The on-sky tests were performed at the University of Tübingen using one of the available telescopes there.

The results of these tests will be used as a basis for the following thermal and vacuum tests of the camera and for a visible camera selection for the STUDIO prototype mission.

The figures of merit, frames types, and procedure overview are detailed in [1].

❖ pco.edge 2.4 characteristics

The optical characteristics of the camera as provided by PCO are detailed below. [2]

image sensor	
type of sensor	scientific CMOS (sCMOS)
image sensor	CIS2020A
resolution (h x v)	2048 x 2048 active pixel
pixel size (h x v)	6.5 µm x 6.5 µm
sensor format / diagonal	13.3 mm x 13.3 mm / 18.8 mm
shutter modes	rolling shutter (RS) with free selectable readout modes, e. g. lightsheet scanning mode[1]
MTF	76.9 lp/mm (theoretical)
fullwell capacity (typ.)	30 000 e^-
readout noise[2]	$0.9_{med}/1.4_{rms}$ e- @ slow scan $1.0_{med}/1.5_{rms}$ e- @ fast scan
dynamic range (typ.)	33 000 : 1 (90.4 dB) slow scan
quantum efficiency	> 82 % @ peak
spectral range	370 nm .. 1100 nm
dark current (typ.)	< 0.5 e^-/pixel/s @ 5 °C
DSNU	< 1.0 e^- rms
PRNU	< 0.5 %
anti blooming factor	> 10000

Figure 1: Technical data of the pco.edge 4.2 sensor

camera

frame rate @ 2048 x 2048 pixel	100 fps, fast scan
exposure / shutter time	100 µs .. 10 s
dynamic range A/D[5]	16 bit
A/D conversion factor	0.46 e^-/count
pixel scan rate	272.3 MHz fast scan 95.3 MHz slow scan
pixel data rate	544.6 Mpixel/s 190.7 Mpixel/s
binning horizontal	x1, x2, x4
binning vertical	x1, x2, x4
region of interest (ROI)	horizontal: steps of 1 pixel vertical: steps of 1 pixel
non-linearity	< 1 %
cooling method	+ 5 °C stabilized selectable: peltier with forced air (fan) or water cooling (both up to 27°C ambient)
trigger input signals	frame trigger, sequence trigger, programmable input (SMA connectors)
trigger output signals	exposure, busy, line, programmable output (SMA connectors)
data interface	Camera Link Full (10 taps, 85 MHz)
time stamp	in image (1 µs resolution)

Figure 3: technical data of the pco.edge 4.2 camera

frame rate table[3]

typical examples	fast scan	slow scan
2048 x 2048	100 fps	35 fps
2048 x 1024	200 fps	70 fps
2048 x 512	400 fps	140 fps
2048 x 256	800 fps	281 fps
2048 x 128	1600 fps	562 fps
1920 x 1080	189 fps	66 fps
1600 x 1200	170 fps	60 fps
1280 x 1024	200 fps	70 fps
640 x 480	420 fps	150 fps
320 x 240	853 fps	300 fps

Figure 2: Frate rate table of the pco.edge 4.5 camera

IN-LAB TESTS

1.1 TEST SETUP

The tests were performed in the the satellite integration and optical laboratory clean room at the IRS. The laboratory offers clean and stable environmental conditions.

The optics test table was used for mounting all tests hardware.

The integrating sphere was used as a homogenous light source for the tests.

An oscilloscope was used to verify the framerate measurements.

The camera was fixed on an aluminum plate, and placed on a telescopic platform. It was then centered at a distance of 110 cm from the integrating sphere.

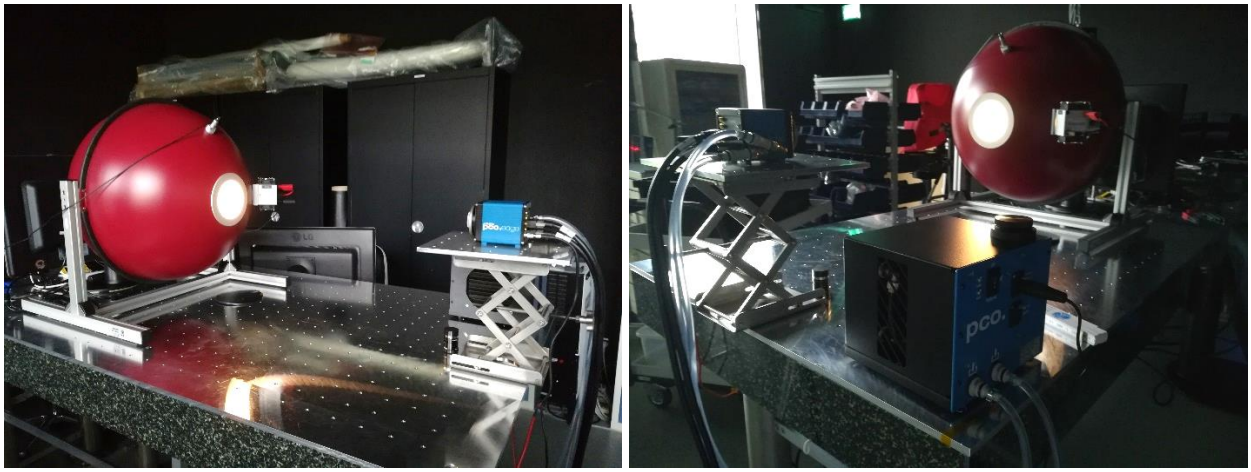

Figure 4: Setup of the in-lab tests including: the integrating sphere, the pco.edge 4.2 camera, and cooling system

The camera's software provided by PCO is a data acquisition program with basic but sufficient features to cover our needs. It allows to control the camera's settings, take and save the corresponding frames.

All acquisitions were made with slow scan to lower the noise level.

The following tools were used for data processing and analysis:

- ImageJ
- Python
- Excel

The images were saved in RAW 16bit RGB **.tif** files, and converted using a python script to **.fits**.

1.2 TEST RESULTS

1.2.1 Set 1: FRAME RATE

The objective of this set is to determine the frame rate of the pco.edge 4.2 camera for different frame size and binning factors.

The frames were not saved, and the frame rate was directly read from the camera's software as displayed on the screen and was confirmed using the oscilloscope.

	1x1	2x2	4x4
Full frame	35,12 fps	35,12 fps	35,12 fps
Half-Frame	70,18 fps	69,91 fps	69,64 fps
Quarter-Frame	140,09 fps	139,00 fps	137,94 fps

Table 1: Frame rate set results

The framerate increases significantly for smaller frame size. The binning on the other hand, slightly reduces the frame rate for frames of the same size.

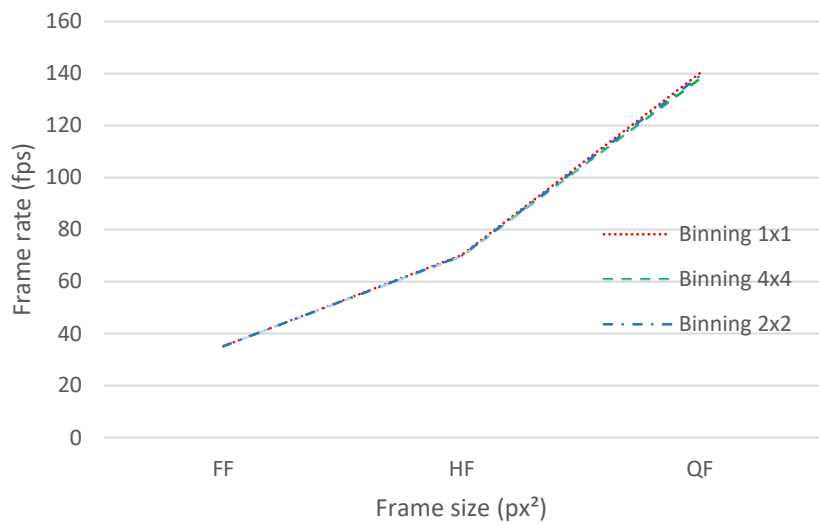

Figure 5: Frame rate Vs Frame size for different binning options

The framerates measured are close to the ones given in the datasheet provided by PCO of the pco edge 4.2.

1.2.2 Bias

The bias is an offset added to all the CCD's pixels to avoid negative values of the signal. Theoretically, it is measured form a frame taken with a closed shutter at 0 sec exposure time to make sure it only contains bias and readout noise. However, since it is not technically possible to take pictures with 0 sec of exposure time, the bias frames were be taken for the minimum exposure time allowed by the pco.edge 4.2 camera 100 µs.

For this purpose, 15 bias frames were taken and saved. The mean pixel values (MPV) were measured for each frame. The mean value was then multiplied by the gain given in the datasheet of the pco.edge 4.2 camera to obtain the bias in in electrons per pixel.

$$Bias_i = MPV_i\ [ADU]$$
$$eBias_i = MPV_i\ \times gain\ [e-/px]$$

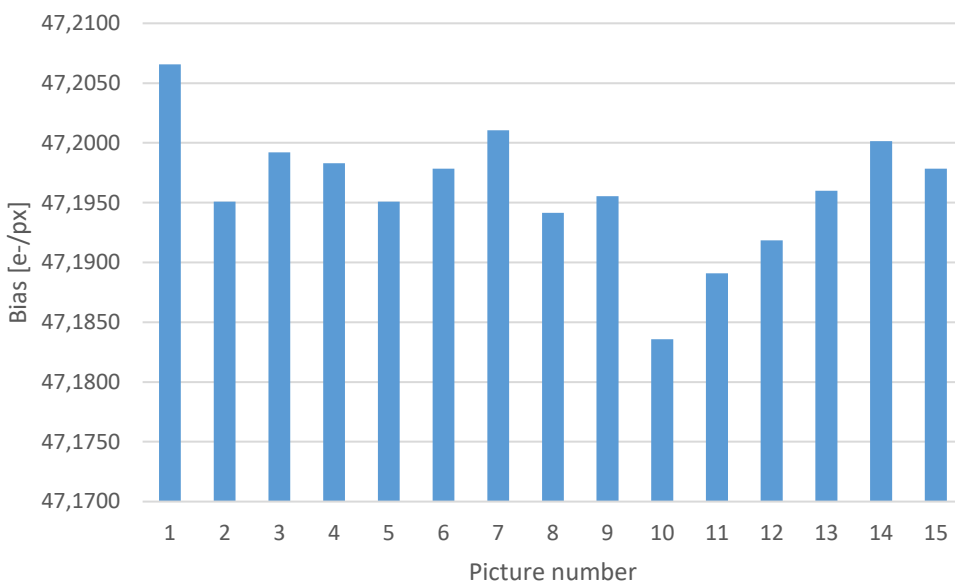

Figure 6: bias value obtained in 15 saved frames

The mean of the 15 bias values obtained was calculated to have one mean bias value of the camera, then multiplied by the gain to obtain the bias in electrons per pixel.

$$Mean\ Bias\ Value = \frac{1}{15}\sum_{i=1}^{15} Bias_i$$
$$Mean\ eBias\ Value = \frac{1}{15}\sum_{i=1}^{15} eBias_i = \frac{gain}{15}\sum_{i=1}^{15} Bias_i$$

The bias value obtained is:

$$Mean\ Bias\ Value = \ 102{,}60\ [ADU]$$
$$Mean\ eBias\ Value = \ 47{,}20\ [e-/px]$$

The median frame is obtained from the 15 bias frame using AstroImageJ, is saved as *MedBias_100.fits*, and will be used for further processing.

The histogram below of the *MedBias* frame pixel values confirms the expected Gaussian distribution of the bias around the mean value 102,60 ADUs (~47,20 e-/px). with a standard deviation of 2,6946 ADU (~1,23 e-/px).

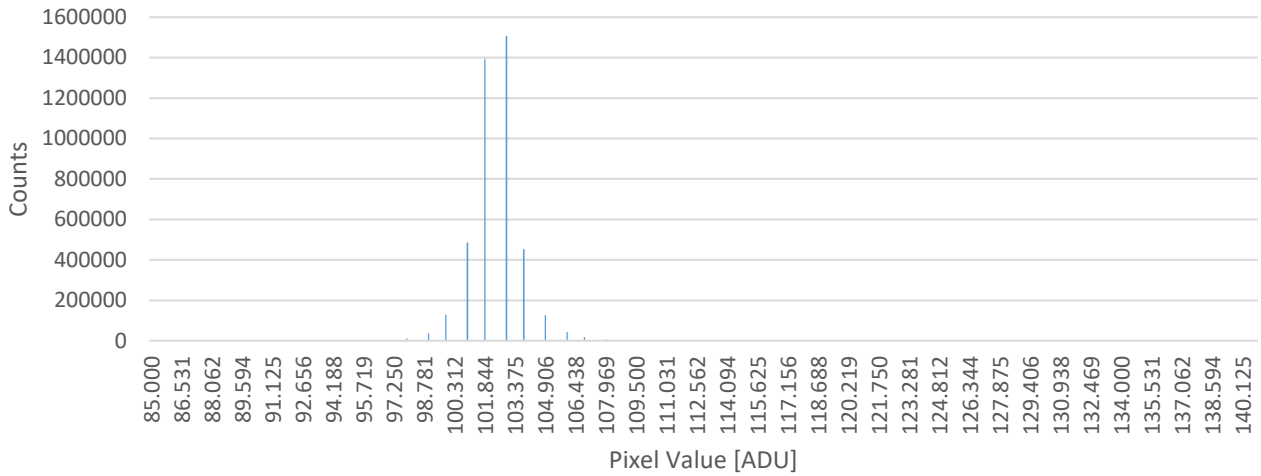

Figure 7: Counts Versus Pixel Value of MedBias_100

1.2.3 Readout Noise

The readout noise is a random noise usually caused by the electrical components during the readout.

The readout noise is measured from 2 bias frames (A and B) by subtracting one from the other to eliminate the contribution of hot regions of the sensor. The standard deviation of the resulting frame is then divided by the square root of two, and multiplied by the gain to express the readout noise in electrons.

$$\sigma_{readout} = g \times \frac{\sigma_A - \sigma_B}{\sqrt{2}}$$

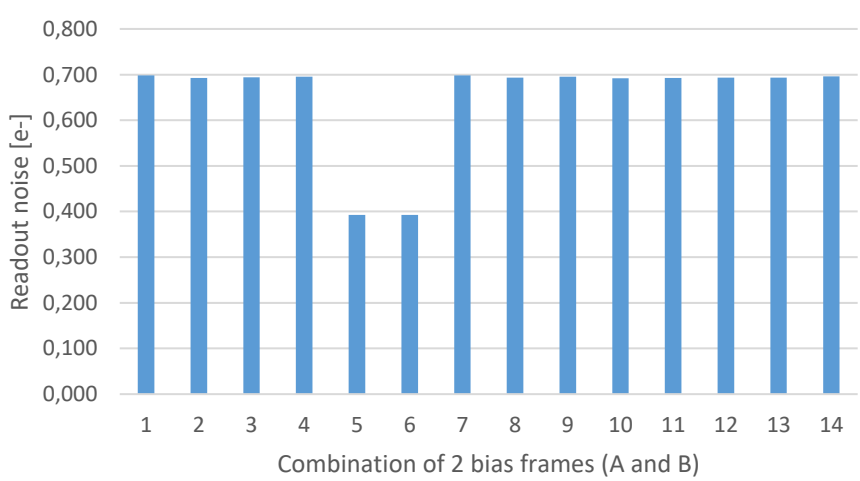

Figure 8: Calculated readout noise for different bias frames combinations

For more precision, 14 values of the readout were calculated by combining different bias frame. The mean value was then calculated.

$$Mean\ Readout\ Noise\ Value = \frac{1}{14}\sum_{i=1}^{14}\sigma_{readout\ i}$$

The obtained mean readout noise is:

$$Mean\ Readout\ Noise\ Value = 0{,}652\ e-$$

The measured readout noise is lower than the one mentioned in the pco.edge 4.2 datasheet.

1.2.4 Dark noise

The dark noise is one of the main sources of noise in most sensors images. It is caused by thermal agitation of electrons, and occurs even in absence of input light. Dark noise's temperature dependence is studied in [3]. All dark noise results shown in this section were from measurements done in ambient temperature of 25°C.

Ten dark frames were taken with a closed shutter for different integration time from 1s to 10s. For every integration time, the median of the 10 frames was combined using AstroImageJ.

For each *MedDark*, the mean pixel value was calculated and multiplied by the gain as given in the datasheet to obtain the number of dark electrons per pixel [e-/px]. These values were plotted versus the integration time.

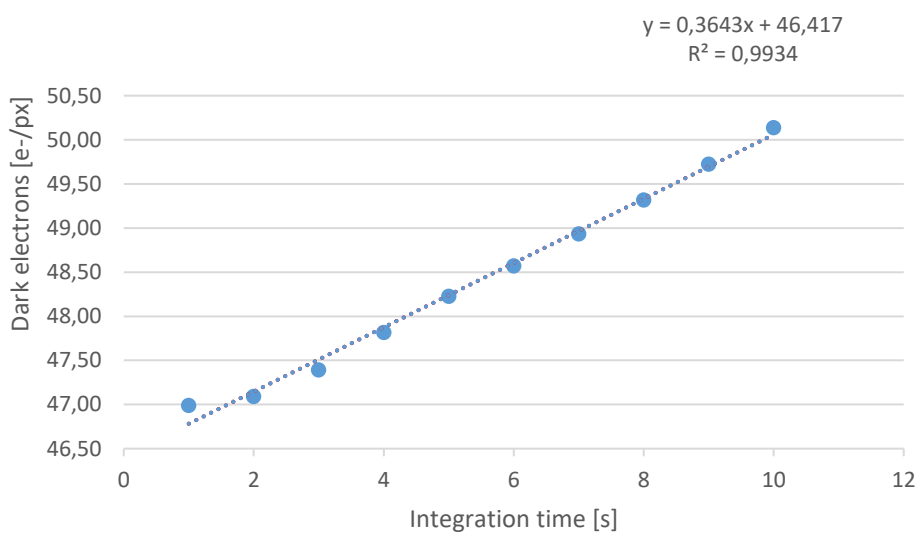

Figure 9: Dark electrons Vs integration time at 25 °C

A linear fit was applied to all data points. As shown in **Figure 9**, the dark noise has the expected linear behavior (R^2=0,99)**Fehler! Verweisquelle konnte nicht gefunden werden.**. The slope of this linear fit is the dark noise rate expressed in [e-/px/s].

The obtained dark noise rate is:

$$Dark\ Current\ Rate = \ 0{,}36\ [e-/px/s]$$

The measured dark noise is lower than the one mentioned in the pco.edge 4.2 datasheet.

The y-intercept (~ *46,41 e-)* corresponds to the bias. This value is close to the bias electrons (~*47,20 e-*) measured in 1.2.2.

- Dark Current Non-Uniformity

To investigate the existence of a dark current pattern, we calculated the deviation, expressed in percentage, of different dark current rates from the mean dark current rate.

Ten dark frames at an integration time of 10s were used for this measurements.

The histogram in Figure 10: Counts Vs Deviation to mean dark current rate**Figure 10** shows, from a total of 10 frames, the number of frames versus the deviation of their measured dark current rate to the mean dark current rate.

The majority (50%) of the dark current rates has a deviation of ~ 0% from the mean dark current. While 100% measurements have a deviation smaller than 1%, resulting in 0,03e-, which complies with the specifications given in the datasheet.

For better accuracy, the same calculations need to be done with a larger number of frame. These tests can be done again when acquiring the camera.

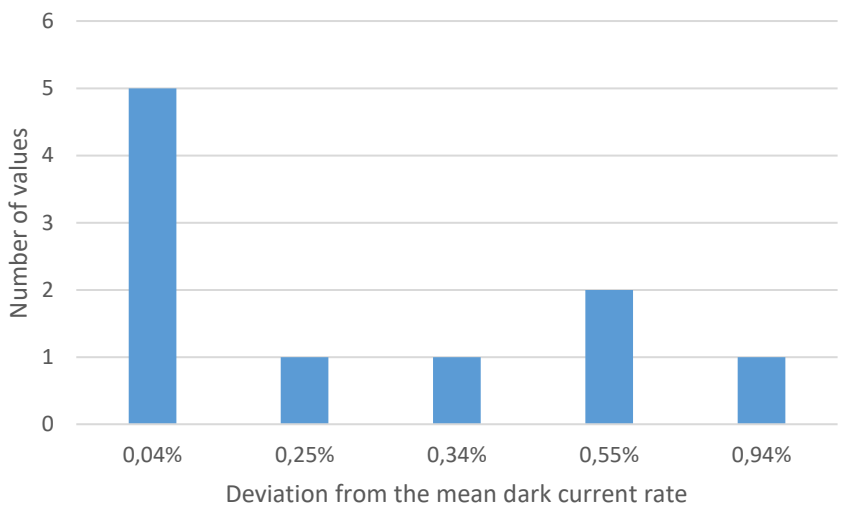

Figure 10: Counts Vs Deviation to mean dark current rate

1.2.5 Full Well Capacity and Dynamic Range

The full well capacity is maximum number of electrons that a pixel can contain.

For this measurement, flat frames are taken, and the maximum ADU observed was for a source irradiance of 5W/m², and an integration time of 4,5ms. Below are the values obtained:

$$Max\ Value = 50003\ [ADU]$$

The number of ADUs multiplied by the gain gives the

$$\boxed{Max\ Value = 23001{,}38\ [e-]}$$

The max value measured is lower than the FWC given in the datasheet (30000 [e-]). However, it might be that the acquisition duration was not sufficient to reach the maximum electrons value.

The acquisition was stopped at an integration time of 4,5 ms seeing no “visible” difference from frames taken at lower integration times and avoiding saturation of the sensor.

Further tests with longer integration time can be carried out in the future.

- Dynamic Range

The Dynamic Range defined the sensor's ability to record simultaneously low and high signals. It is the ratio between the smallest and the largest possible values contained in one pixel. The smallest being the readout noise, and the largest being the FWC. It is expressed in Decibel and measured using the following equation:

$$DR = 20 \times \log\left(\frac{FWC}{\sigma_{readout}}\right)$$

For the FWC measured above, the obtained dynamic range is:

$$DR = 90{,}95\ [dB]$$

Updated test values with potential higher FWC, from future tests, will result in a higher DR. However, for the measured FWC above, the DR is already higher than the DR given in the pco.edge 4.2 datasheet.

1.2.6 Gain

The gain is the conversion factor from the photo-electrons to ADUs.

- **Approach 1**

The gain can be measured using nine combinations of two different flat frames (A and B) at the same integration time:

- First, the sum of the two frame A and B is obtained using AstroImageJ. Then the mean pixel value of the resulting frame is noted MPV_{A+B}.
- Second, one frame is subtracted from the other, and the standard deviation of the result frame is noted σ_{B-A} .
- The gain can then be calculated using the equation:

$$Gain_i = \frac{MPV_{A_i+B_i}}{(\sigma_{B_i-A_i})^2 - (\sigma_{readout})^2}$$

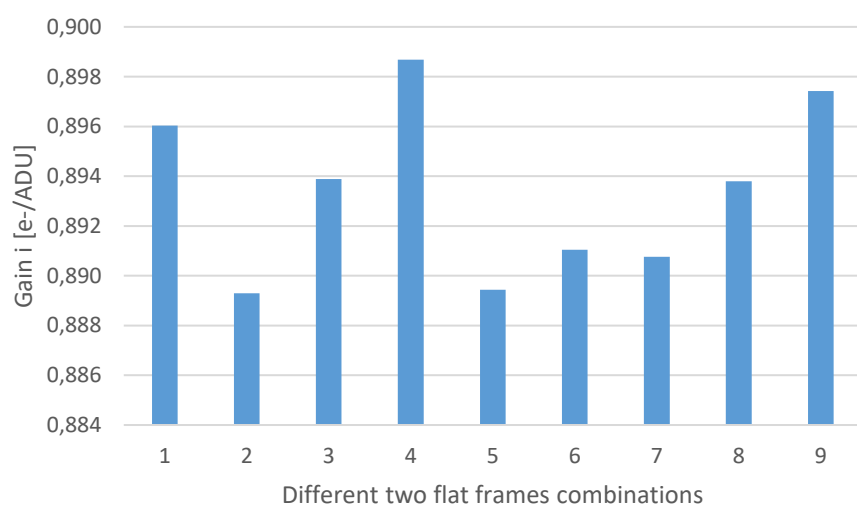

Figure 11: Obtained Gain values for different flat frames combinations with approach1

- Finally, the mean gain is calculated from the nine gain values obtained from the nine combinations

$$Gain = \frac{1}{9}\sum_{i=1}^{9} Gain_i$$

$$Gain = 0{,}893\ [e-/ADU]$$

The gain measured is considerably lower than the one given in the datasheet (0,46 [e-/ADU]). Therefore, a second approach is necessary to confirm the result of the first one.

- **Approach 2**

For this approach, 9 different combinations of 2 flat frames and 2 bias frames were used.

- First, two flat frames (A and B) are summed using AstroImageJ. The mean pixel value of the resulting frame is noted MPV_{A+B} .
- Second, one flat frame is subtracted from the other. The standard deviation of the resulting frame is noted σ_{B-A} .
- Next, two bias frames (B1 and B2) are summed using. The mean pixel value of the resulting frame is noted MPV_{B1+B2} .
- Then, one bias frame is subtracted from the other. The standard deviation of the resulting frame is noted σ_{B2-1} .
- Later, the gain for each combination is calculated using the equation:

$$Gain_i = \frac{MPV_{A_i+B_i} - MPV_{B1_i+B2_1}}{(\sigma_{B_i-A_i})^2 - (MPV_{B1_i+B2_i})^2}$$

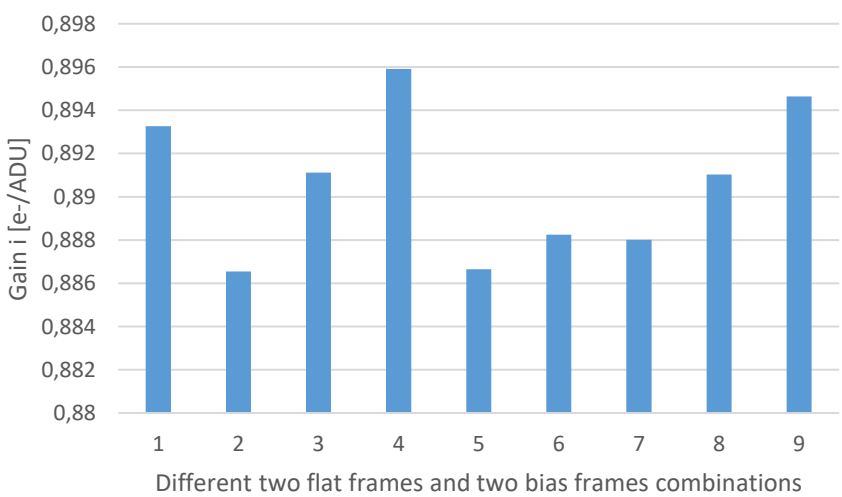

Figure 12: Obtained Gain values for different flat frames combinations with approach2

- Finally, the the mean gain is calculated from the nine gain values obtained from the nine combinations

$$Gain = \frac{1}{9}\sum_{i=1}^{9} Gain_i$$

$$Gain = 0{,}890\ [e-/ADU]$$

- **Comparison between the two approaches**

The gain calculated with the two approaches are quite similar, to a precision of 10^{-3}.

The gain measured is considerably lower (almost half) than the one given in the pco.edge 4.2 datasheet.

A high gain is useful when observing faint objects, as it will help producing more ADUs thus reducing the roundoff effect. On the other hand, a low gain is useful when observing very bright objects by decreasing the number of ADUs produced for a number of photons, which results in the possibility of containing more electrons in one pixel without reaching saturation (FWC).

Since the visible camera will mainly be used for centroid tracking, it will be looking at bright stars. Therefore, a lower gain might be more appropriate for our application. However, we might need to discuss these results with PCO.

1.2.7 Photo Response Non-Uniformity

The Photo Response Non-Uniformity describes the differences in sensitivity between pixels.

From a first look at the dark frames, an obvious difference in sensitivity between the upper half from the lower one. The presence of horizontal line in the middle of the frames shows that the sensor is in reality composed of two halves which are exposed and read out simultaneously.

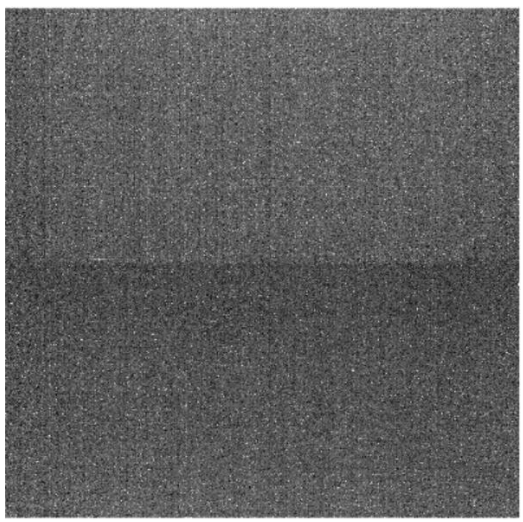

Figure 13: Dark frame at 1s of integration time

The PRNU is defined as the standard deviation of a frame divided by its mean pixel value. It depends on the wavelength of the observed source. With absence of light sources with unique wavelengths, the integrating sphere with halogen lamp was used.

- *MedFlat* frames with different integration time are used.
- The standard deviation and mean pixel value in calculated from each frame using AstroImageJ.
- The PRNU for every integration time is calculated with the equation:

$$PRNU_i = \frac{\sigma_i}{MPV_i}$$

- The mean PRNU is then calculated from the ten $PRNU_i$ measured above.

$$PRNU = \frac{1}{9}\sum_{i=1}^{9} PRNU_i$$

The obtained PRNU is:

$$PRNU = 7{,}53\ \%$$

This value is quite larger than the one given in the pco.edge 4.2 (<0,5%).

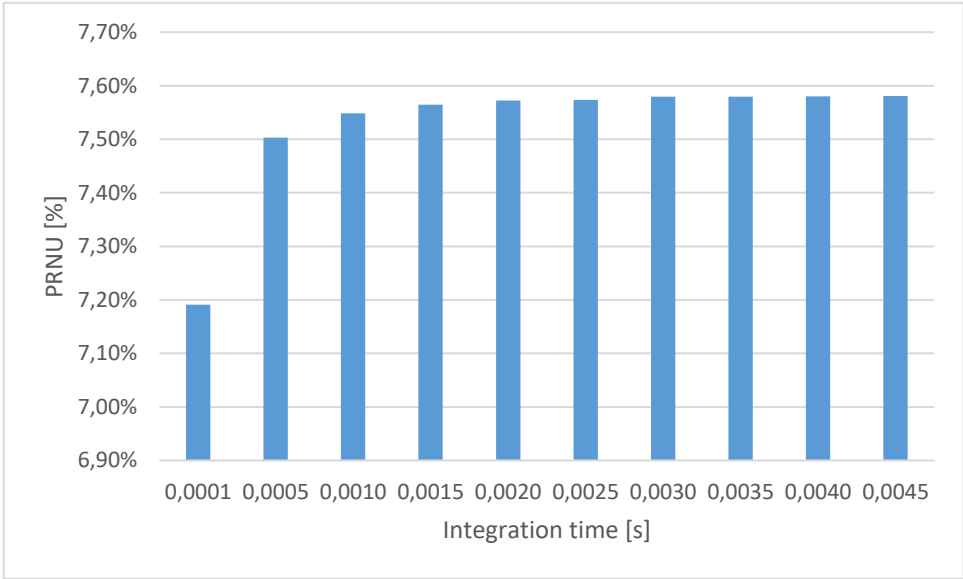

Figure 14: Photo Response Non-Uniformity Versus Integration time

When having another look at the flat frames used for this test, we noticed that the last 10 columns of pixels on the right side of the frames were completely dark.

Figure 15: Flat image taken at 4,5 ms

This might have been caused by a physical obstruction when placing baffles around the optical path. Otherwise, the CMOS sensor skipped reading the last columns of each line. Since this anomaly didn't show in other pictures (during the on-sky tests), It is assumed that due to the

baffles. The frames were then cropped, and the calculations done a second time, without the dark parts.

The mean PRNU calculated with corrected flat frames was found:

$$PRNU = 0{,}90\ \%$$

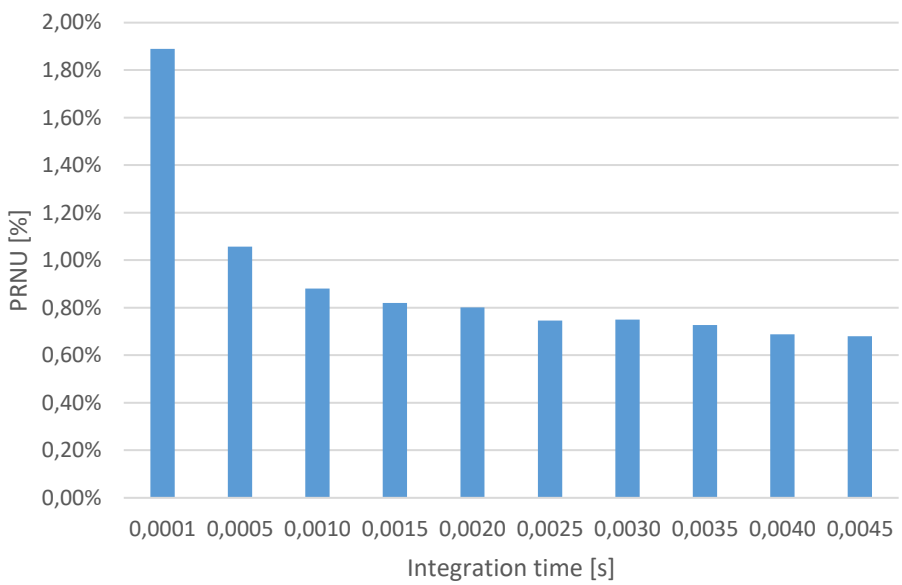

Figure 16: Photo Response Non-Uniformity Versus Integration time (Corrected frame)

This time, the values seem to be more coherent, in comparison with the value given by the manufacturer. However, it remains slightly higher. The uniformity between pixels decreases with higher integration time.

As the PRNU depends on the source's wavelength, this difference might be due to the inappropriate light used for this test. It is better to redo the test with a light source that has a unique wavelength, or use filters.

In the meantime, the wavelength at which PCO certifies a PRNU of < 0,5% should be discussed with PCO.

1.2.8 Photo Response Non-Linearity (PRNL)

The Photo Response Non-Linearity helps checking the linearity of the CMOS.

- **Rate of increase**

As a first step, we observe the rate at which the pixel value increases for different integration times.

- First, from the 10 flat frames taken at the same integration time 1 median image is obtained using AstroImageJ. The resulting frames are saved as *MedFlat.*
- Then, *MedFlat* frames are bias corrected by subtracting MedBias from them. The mean pixel value of the resulting frames are noted MPV_i.

- The MPV_i are divided by their corresponding integration times and plotted versus the integration time.

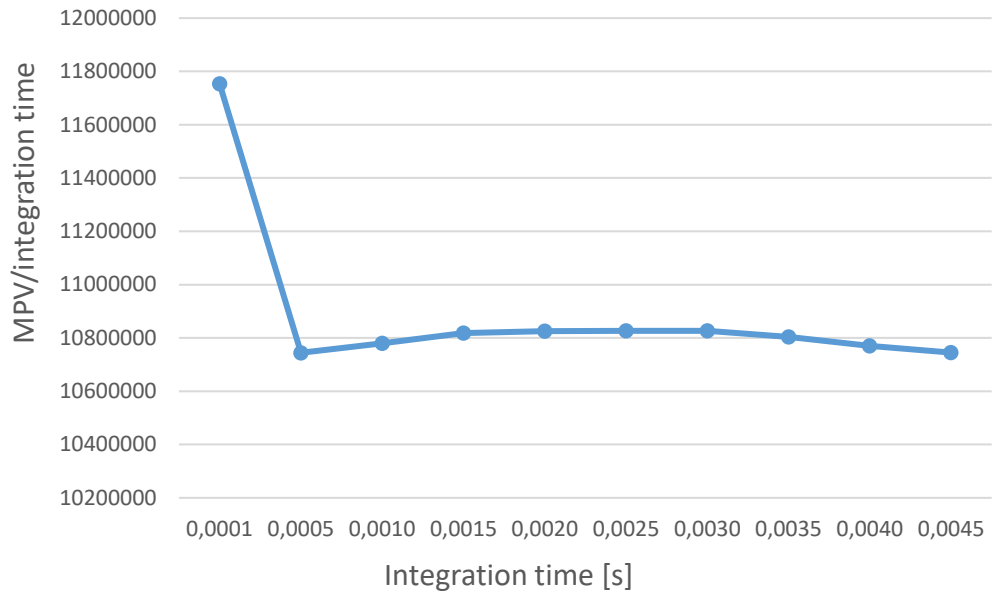

Figure 17: Linearity of the rate of increase

From the plot, it looks like that first value is abnormal. There might have been a problem during the frame acquisition. Ignoring the first acquisition at the smallest integration time, the plot would be as follow:

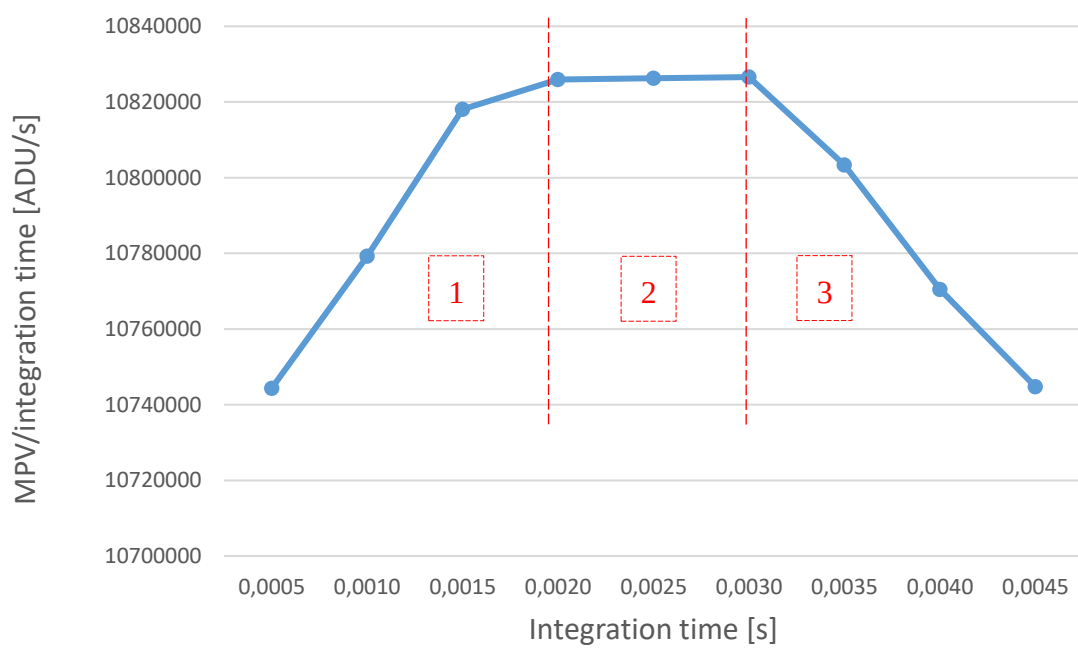

Figure 18: Linearity of the rate of increase (Without the frame at 0,0001 s)

The rate of increase of a perfect sensor would be a horizontal line. However, many sensors don't have a "perfectly" linear behavior.
The first part of the plot shows an ascending line which become horizontal in the second part, which then drops off in the third one.
During the first part, the sensor is taking at each step more electrons until reaching stability during the second part. At high pixel values, the rate decreases as the senor approaches saturation.
It is known that the rate might decrease when reaching half of the FWC. In our case this would correspond to ~ 14854 [e-] at 0,003 [s]. Which is indeed close to the FWC given in the pco.edge 4.2 datasheet.
Non-linear behavior as this one would result in poor photometric performance, as it would prevent accurate image corrections with flat fields. [4]

Next step would be to have a closer look at this non-linearity.

- **Photo Response Non-Linearity**

For this part, flat and dark frames are used.

- First, *MedFlat* are dark corrected by subtracting a dark frame from the corresponding flat frame.
- The mean pixel value of the resulting frames are noted MPV_i, and are plotted versus the integration time.
- A linear regression is then applied to obtain the best linear fit to describe the plot.

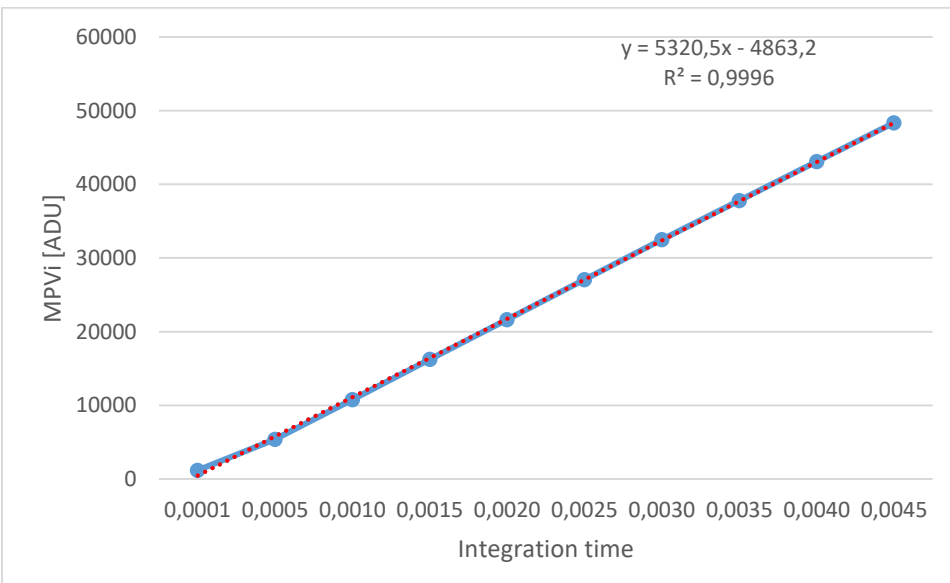

Figure 19: Mean Pixel Values of dark corrected flat fields Versus integration time

The coefficient of regression (R^2=0,9996) shows how well the measured values are close to a linear behavior.

- Next, the non-linearity at each integration time is calculated by comparing the expected values to the measured ones. The absolute value is expressed in percentage using the equation:

$$Non - Linearity = 100 \times \left(1 - \frac{eMPV_i}{MPV_i}\right)$$

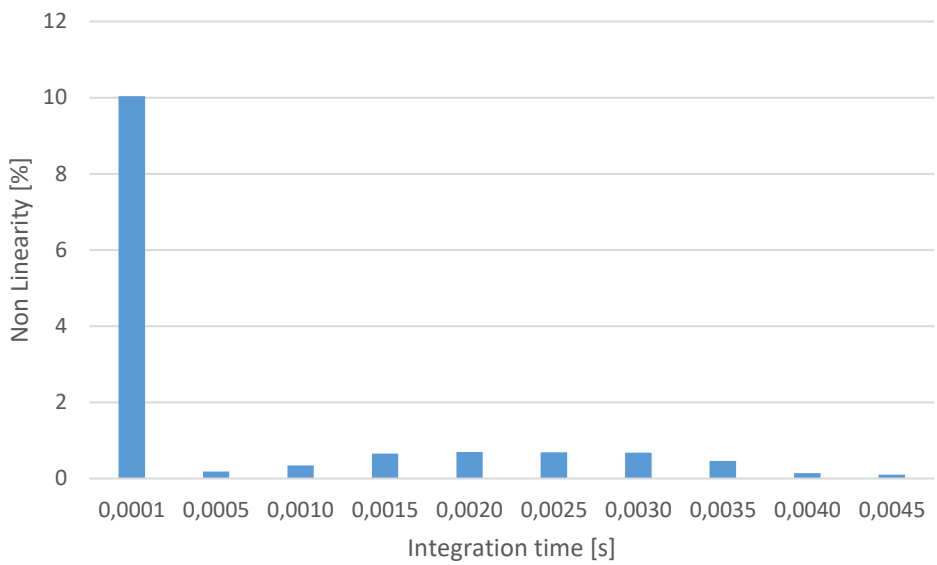

Figure 20: Non-linearity Versus integration time

As mentioned before, the first value might be an aberration. It will be ignored.

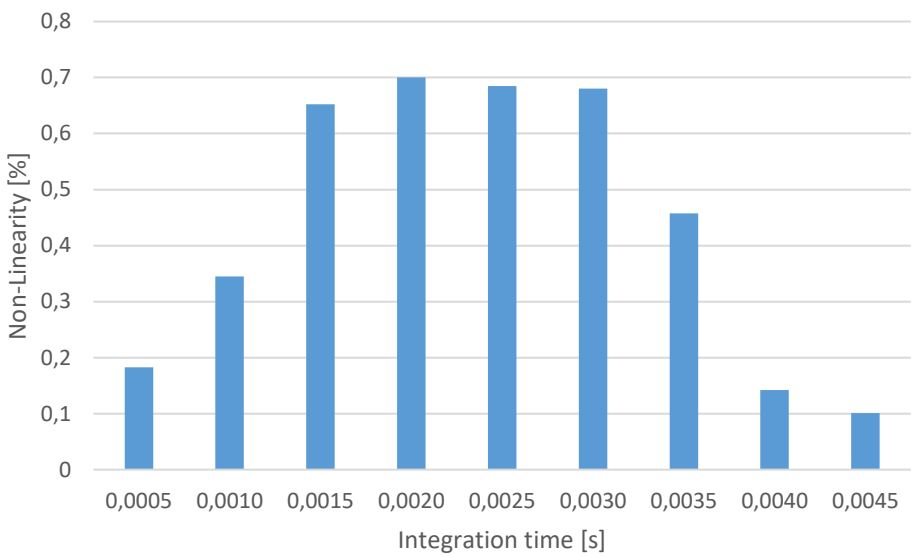

Figure 21: : Non-linearity Versus integration time (without the first value)

From this plot, we can see that the non-linearity is lower than 0,7 %, which complies with the non-linearity given in the pco.edge 4.2 datasheet. (< 1%).

1.2.9 Quantum Efficiency

The quantum efficiency is defined by the ratio of number of generated electrons to the number of incoming photons. It is expressed in percentage.

$$\eta = \frac{n_{electrons}}{n_{photons}}$$

The number of electrons can be deduced by multiplying the ADUs read on every pixel by the gain. However, the number of photons has to be calculated with the equation:

$$n_{photons} = \frac{A\,.\,E\,.\,t_i}{\frac{hc}{\lambda}}$$

With : $\begin{cases} A: pixel\ area \\ E: irradiance \\ t_i: integration\ time \\ h: Planck's\ constant \\ c: speed\ of\ light \\ \lambda: source's\ wavelength \end{cases}$

As the number of photons depends on a specific wavelength, it is impossible to measure the quantum efficiency from the flat fields taken with the halogen lamp.

The calculation need to be done with new flat fields taken with a unique wavelength source.

ON-SKY TESTS

1.1 TEST SETUP

The on-sky tests took plate in Tübingen using the 8” Meade telescope available there.

The original plan was to use the Takahashi FS-128 telescope. However, an appropriate mount to fix the camera to the telescope at the focal plane was not available.

For a better image quality, a UV/IR blocking filter was used.

Figure 22: Setup of the on-sky tests including: the meade telescope, the pco.edge 4.2 camera, and cooling system

Table 2: Specifications of the Meade 8" Telescope [5]

Telescope	8" LX200 f/6.3
Optical Design	Schmidt-Cassegrain Catadioptric
Focal Length	1280mm
Primary Mirror diameter	203 mm,
Focal Ratio	f/6.3
Resolution	0.56 arcsec
Camera pixel size	6,5 µm
Angular pixel size	0,426 arcsec

The field observed was selected for the bright stars it had. The observed stars are as follow:

Star	Apparent Magnitude V
mu, Lyr	5,12
TYC 3108-1150-1	10,72
TYC 3108-95-1	11,24
TYC 3108-11-1	11,24
TYC 3108-1808-1	11,29
TYC 3108-2061-1	11,30
TYC 3108-357-1	11,34
TYC 3108-2002-1	11,40
TYC 3108-1921-1	11,44
TYC 3108-129-1	11,49

Table 3: List of observed stars and their corresponding magnitudes (V) as given in Simbad catalog [6]

1.2 TEST RESULTS

1.2.1 Limiting magnitude

For these measurements, 10 frames were taken and save at each integration time.

A median frame of the 10 frames was obtained using AstroimageJ and saved as *MedScience*.

Again, using *AstroImageJ* and Astrometry.net we were able to solve the images and recognize the stars we observed.

The frames taken at 0,001 seconds were too noisy to detect any star of the field of view.

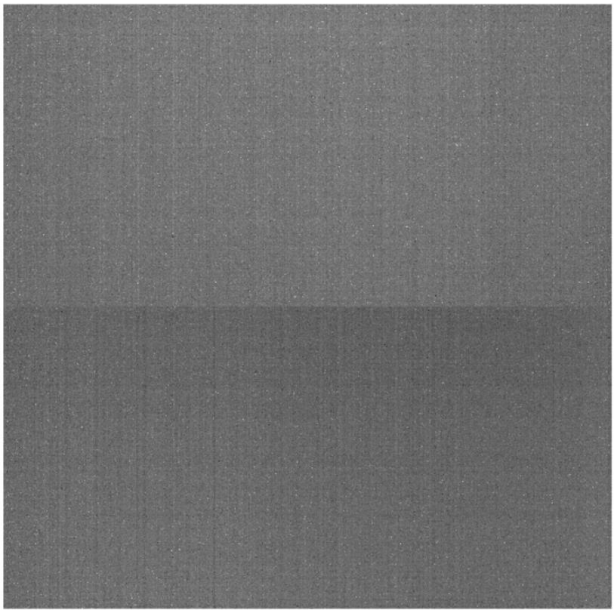

Figure 23: Science Frame at 0,001 s of integration time

From a first look at the *MedScience* frames, it is noticeable that the telescope's position was not stable. We can clearly see the movement of the stars on the images: towards the right-down with longer integration times. Some stars appear in some integration times and others disappear in other integration times, making it harder to make a comparison between the frames.

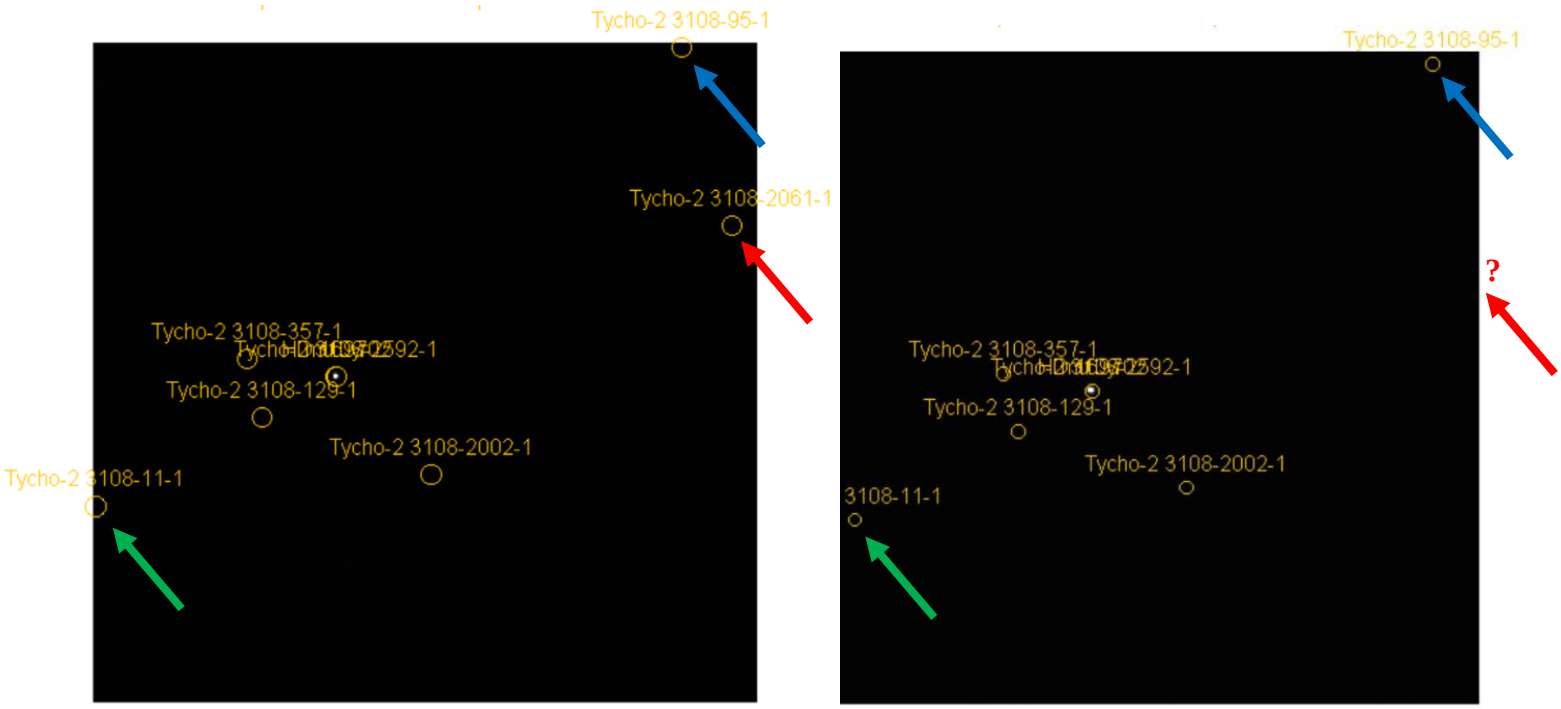

Figure 24: Stars movement on Science Frames at 0,5s and 1s integration times

Table 4: List of appearing stars for every integration time

Star	Integration time [s]							
	0,001	0,005	0,01	0,05	0,1	0,2	0,5	1
mu, Lyr	ND	Y	Y	Y	Y	Y	Y	Y
TYC 3108-1150-1	ND	ND	ND	Y	Y	Y	N	N
TYC 3108-95-1	ND	ND	ND	N	N	N	Y	Y
TYC 3108-11-1	ND	ND	ND	N	N	N	Y	Y
TYC 3108-1808-1	ND	ND	ND	N	Y	Y	N	N
TYC 3108-2061-1	ND	ND	ND	Y	Y	Y	Y	N
TYC 3108-357-1	ND	ND	ND	Y	Y	Y	Y	Y
TYC 3108-2002-1	ND	ND	ND	Y	Y	Y	Y	Y
TYC 3108-1921-1	ND	ND	ND	N	Y	Y	N	N
TYC 3108-129-1	ND	ND	ND	Y	Y	Y	Y	Y

Y: Yes, the start appears in the frame
N: No, the star does not appear in the frame
ND: Star unsolved using *Astrometry.net*

In this case, only the frame with an integration time equal or higher than 0,05 seconds can be used.

Only the stars appearing in all frames will be used for future calculations.

The frames at 1s of integration time could not be exploited and will therefore be discarded for the calculations as well.

Table 5:Stars used for the calculations and their apparent magnitudes

#	Star	Apparent Magnitude V
1	mu, Lyr	5,12
2	TYC 3108-357-1	11,34
3	TYC 3108-2002-1	11,40
4	TYC 3108-129-1	11,49

- Signal to Noise Ratio

For a first step, the signal to noise ratio for each star at different integration times was calculated.

The SNR is calculated by dividing the peak signal registered from each star by the noise on each frame, measured by the standard deviation of the dark background.

$$SNR_{s,t} = \frac{S_{s,t}}{\sigma_{s,t}}$$

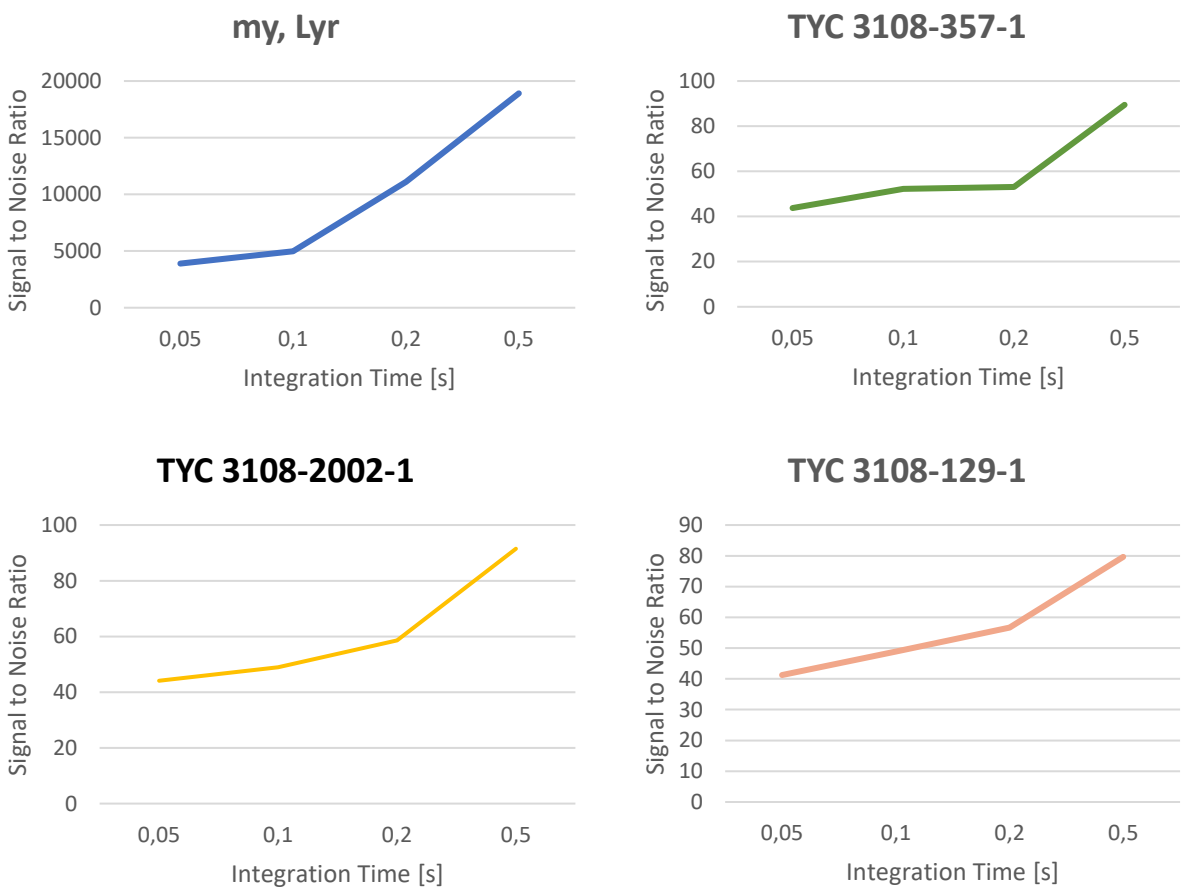

Figure 25: Signal to Noise Ratio measured for different stars for different integration times

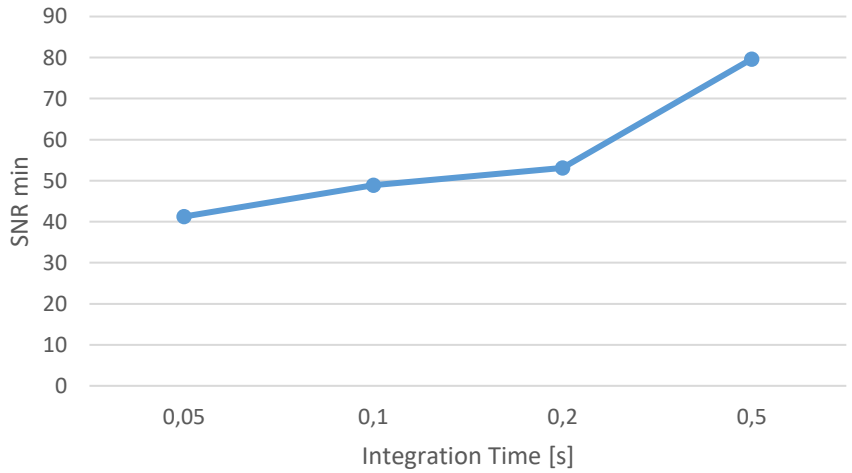

Figure 26: Minimum Signal to Noise Ratios Vs. Integration time

As expected the signal to noise ratio increases with increasing the integration time.

The brighter the star is, the higher the SNR is. However, for a small integration time (0,05 s) we can already have a minimum signal to noise ratio of ~ 41.

Next, is to stack images for one integration time (0,2 s). Using *AstroImageJ*, different number of frames (from 2 to 10) at 0,2 s of integration time were stacked and summed. The resulting stacked frames were saved as *SUM_Stack_#*. The last digit refers to the number of frames stacked.

Then the signal to noise ratio was measured for each stacked *SUM_Stack* frame and will be used for the limiting magnitude calculations.

Figure 27: Minimum Signal to Noise Ratio measured for different stars for different number of stacked frames

The longer the integration time the better the signal to noise ratio. However, for this camera, the integration time is limited to 10s. The purpose of stacking images is to improve the SNR despite the integration time limitation.

For each integration time, the SNR increases with higher number of stacked frames.

- Limiting Magnitude

The limiting magnitude defines the faintest magnitude that can be detected by the instrument.

In our case, all mentioned magnitudes are in the visible band.

The observed magnitude defined as m_r is calculated using the following equation:

$$m_r = m_0 - 2{,}5 \,.\log(S)$$

m_0 being the zero magnitude, and S the signal.

m_0 has to varied for each star, at each integration time until m_r is equal to the apparent magnitude of the star.

For each of the signal to noise ratios calculated in the section above, the minimum SNR is used to calculate the minimum magnitude or limiting magnitude. Assuming that the noise for all frames from the same integration time is constant, we can replace S in the previous equation by

$$S = \sigma \,.\, SNR_{min} \,.$$

The equation becomes then:

$$m_{limiting} = \; m_0 - 2{,}5 \,.\log(\sigma \,.\, SNR_{min})$$

Finally, the mean limiting magnitude is calculated from the limiting magnitudes calculated for each star.

$$m_{limit} = \frac{m_{limit\,1} \,.SNR_1 + m_{limit\,2} \,.SNR_2 + m_{limit3} \,.SNR_3 + m_{limit\,4} \,.SNR_4}{SNR_1 + \; SNR_2 + \; SNR_3 + \; SNR_4}$$

The numbers 1,2,3,4 refer to the stars numbers as given in **Table 5**.

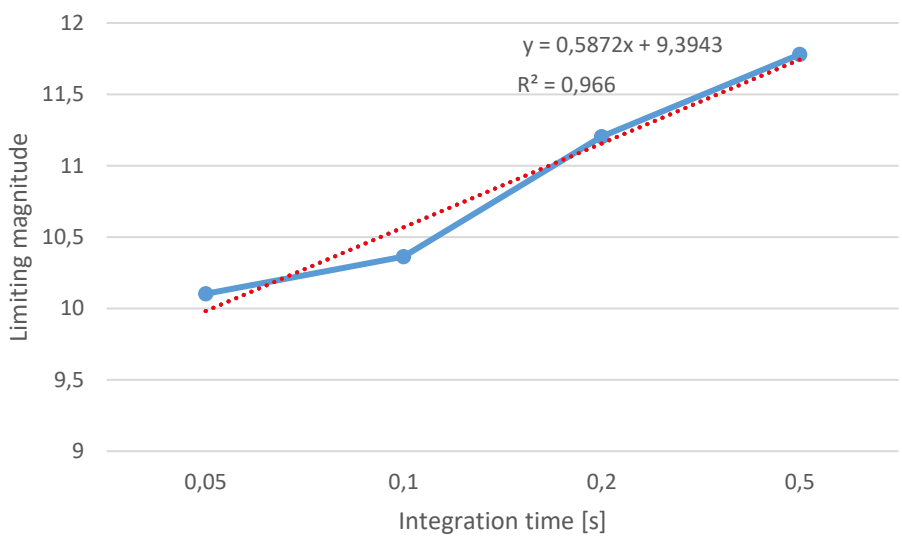

Figure 28: Limiting magnitude Vs. Integration time

The average limiting magnitudes for each integration time are given in **Figure 28** for each integration time shows a linear behavior with a minimum magnitude of 10,10 at 0,05 s.

Using the equation of the linear fit applied to the limiting magnitude as function of integration time, a theoretical limiting magnitude figure for longer integration times is given below.

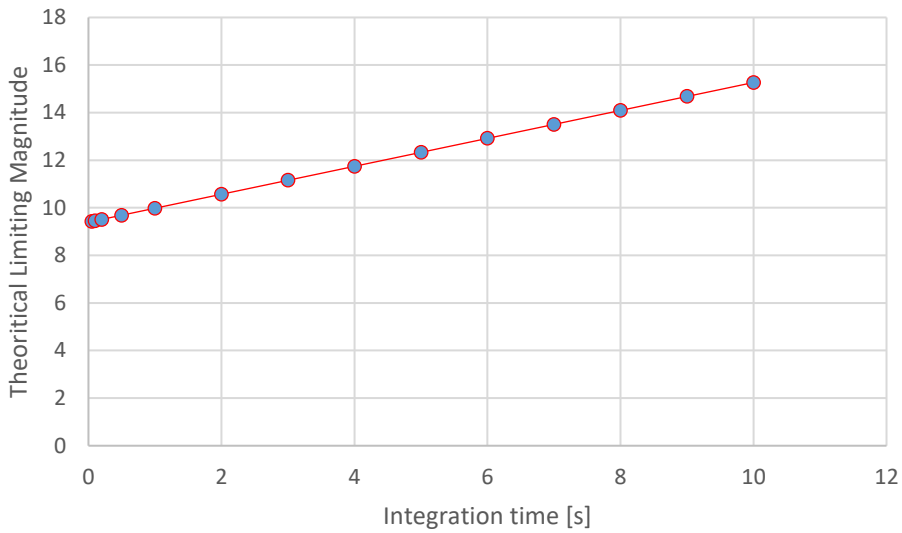

Figure 29: Theoretical limiting magnitude Vs. Integration time

Based on the limiting magnitudes measured for short exposures, the pco.edge 4,2 is expected to have a limiting magnitude of 15,27 at 10 s of integration time.

The camera's integration time limitation (10s) prevents from improving further the limiting magnitude. A way to overcome this issue is to stack multiple images. Thus increasing the SNR and the limiting magnitude at low integration times, with the objective of reaching the numbers of long exposures, or better.

The same calculations were done for stacked frames (from 1 to 10 frames stacked in one single frame).

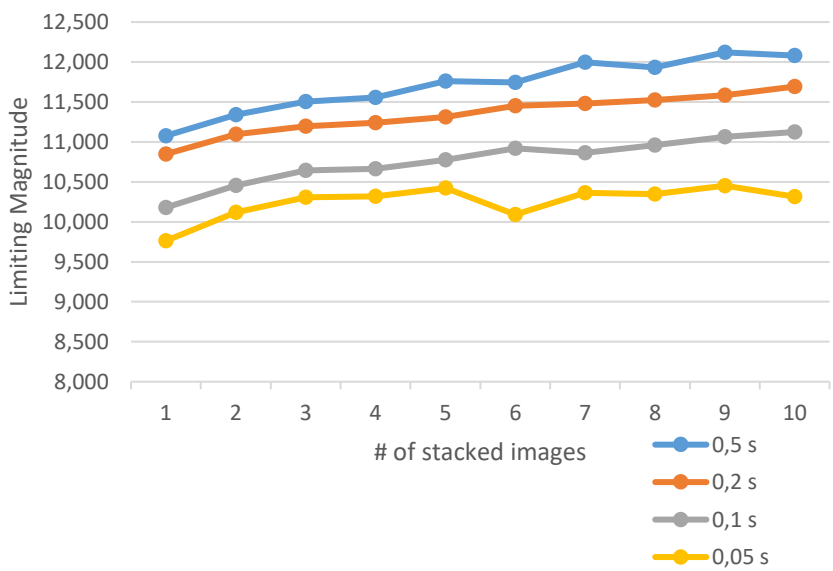

Figure 30: Limiting magnitude Vs. Number of stacked images at 0,2s of integration time

Signal to noise ratio and limiting magnitude measurement have been done using the Meade 8" (~20,32 cm) telescope in Tübingen. The camera is foreseen to be used with ESBO DS' 50 cm telescope with having a larger collecting area. Therefore, factor of 4 of the collected signal. Since the magnitude is an order of 2,5 of the signal, we would gain 1,6 magnitudes with the 50 cm telescope. The new theoretical limiting magnitude is given in below**Fehler! Verweisquelle konnte nicht gefunden werden.**.

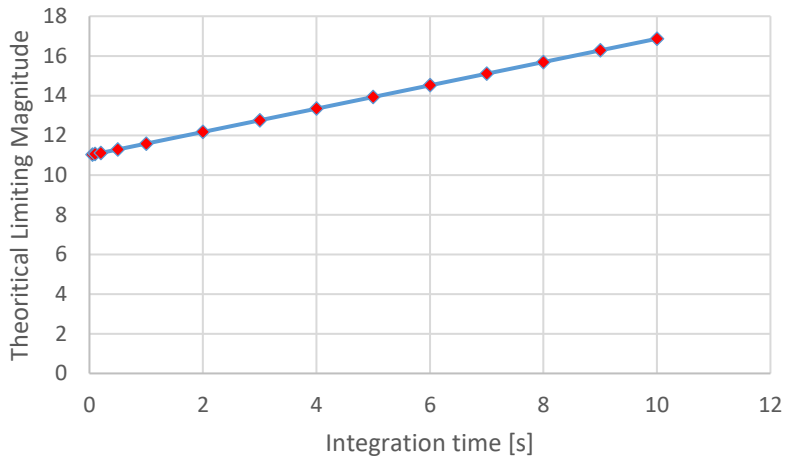

Figure 31: Theoretical Limiting Magnitude for ESBO DS 50 cm telescope Vs. Integration time

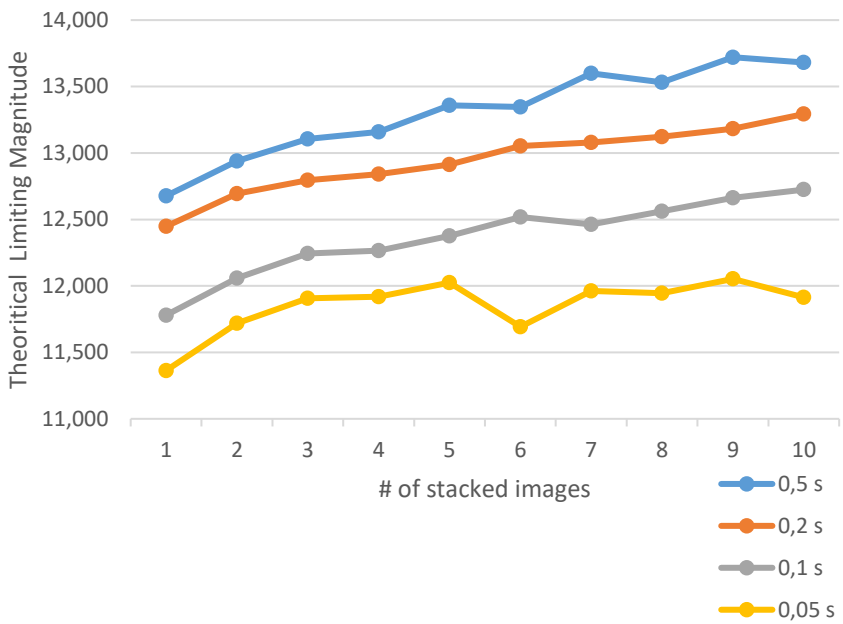

Figure 32: Theoretical Limiting Magnitude for ESBO DS 50 cm telescope Vs. the number of stacked images

Additionally, the image acquisition at 40km will provide a better image quality with less seeing. However, the jitter of the gondola will have to be taken into consideration, since the image stabilization system achieves a stability of only 0,5 arc.

CONCLUSION

The pco.edge 4.2 camera was tested both in-lab and on-sky Figure 28: Limiting magnitude Vs. Integration timeto verify the specifications provided by the manufacturer and confirm its performance.

- In-lab tests

The results of the test are summarized in **Table 6**.

Table 6: Summary of the test results compared with the datasheet

	Measurement	**Data sheet**
Frame rate [FPS] (Full Frame & slow scan)	35,12	35
Bias [e-/px]	47,20	Not provided
Readout noise [e-] (rms @ slow scan)	0,652	1,4
Dark current [e-/px/s]	0,36	< 0,5
Dark Current Non-Linearity [%]	< 0,1	Not provided
Dark Current Non-Uniformity [e-]	0,03	< 1
Full Well Capacity [e-]	23001,38 (Incomplete tests!)	30000
Dynamic range [dB]	90,95 (Incomplete tests!)	90,4
Gain [e-/ADU]	0,893	0,46
Photo Response Non-Uniformity [%]	0,9	<0,5
Photo Response Non-Linearity [%]	< 0,7	< 1%
Quantum Efficiency [%]	Not measured	82

The obtained results are quite close to the data given by the camera manufacturer, and are even better for most figures of merit.

The results that show different performance than the one expected, such as the PRNU and the gain, will be investigated and discussed with the manufacturer.

Some tests need to be completed when purchasing the camera, such as the full well capacity and dynamic range measurements. The quantum efficiency tests will be completed when a monochromatic calibrated light source is available at the IRS.

- On-sky tests

Signal to noise ratio and limiting magnitude measurement have been done using the Meade 8” (~20,32 cm) telescope in Tübingen. The camera is foreseen to be used with ESBO DS’ 50 cm telescope with having a larger collecting area. Therefore, factor of 4 of the collected signal. Since the magnitude is an order of 2,5 of the signal, we would gain 1,6 magnitudes with the 50 cm telescope.

Additionally, the image acquisition at 40km will provide a better image quality with less seeing. However, the jitter of the gondola will have to be taken into consideration, since the image stabilization system achieves a stability of only 0,5 arc.

Complementary tests with longer integration times (up to 10s), a stable telescope positioning, and with a higher number of frames for each acquisition (up to a 1000) for stacking purposes will need to be done.

STU-IRS-O-TN-612-01_v1.00- Nonreflective-Paint-Outgassing-Tests_2020-11-12

OUTGASSING TESTS OF STUDIO NON-REFLECTIVE PAINT SAMPLES

Version 1.0

12 November 2020

Status: As run

H2020 INFRADEV-01-2017 project "European Stratospheric Balloon Observatory *Design Study*"

Topic: INFRADEV-01-2017 Design Studies

Project Title: European Stratospheric Balloon Observatory *Design Study* – ESBO *DS*

Proposal No: 777516 – ESBO DS

Duration: Mar 1, 2018 - Feb 28, 2021

WP (EU)	WP 10
WBS Item (internal)	612
PBS Item(s)	1223-600
Title	Outgassing Test of Non-Reflective Paint
Description	Outgassing tests of non-reflective paint candidates for the TIP straylight protection
Lead Beneficiary	"USTUTT"
Nature	"Report"
Dissemination Level	"Public"
Est. Del. Date	-
Version	1.00
Date	12.11.2020
Status	As run
Lead Author	Julienne Böttger, boettgerj@irs.uni-stuttgart.de, USTUTT
Approved by	Philipp Maier, pmaier@irs.uni-stuttgart.de, USTUTT

VERSION HISTORY

Version #	Implemented By	Revision Date	Approved By	Approval Date	Explanation
1.00	Julienne Böttger	06.10.2020			First Version

TABLE OF CONTENTS

LIST OF ABBREVIATIONS AND DEFINITIONS

Abbreviation	Definition
TVC	Thermal Vacuum Chamber
ESBO *DS*	European Stratospheric Balloon Observatory *Design Study*
STUDIO	Stratospheric Ultraviolet Demonstrator of an Imaging Observatory

REFERENCE DOCUMENTS

[RD1]	ECSS-Q-ST-70-02C
[RD2]	Shimadzu Datasheet of AUW-D/AUW/AUX/AUY Series
[RD3]	
[RD4]	
[RD5]	

1 SCOPE

This procedure documents outgassing tests of non-reflective paint samples in a thermal vacuum chamber (TVC) at the Institute of Space Systems (IRS) of the University of Stuttgart. The objective of this test is to evaluate the suitability of several paints for the straylight protection hardware on the Telescope Instruments Platform (particularly around the UV channel).

These tests are part of the ESBO *DS* project at the University of Stuttgart. ESBO *DS* (European Stratospheric Balloon Observatory *Design Study*). ESBO *DS* is a project conducted by several European partners to evaluate possibilities to observe astronomical targets from a balloon in the stratosphere. The main scientific instrument will observe targets in the ultraviolet regime of the spectrum. The purpose of this test is to evaluate the suitability of different paints for the straylight protection hardware regarding their outgassing properties in a vacuum environment.

2 OVERVIEW

2.1 THERMAL VACUUM CHAMBER

The tests were carried out in the thermal vacuum chamber available at the IRS. The chamber provides a temperature-controlled copper plate for installing test items with a size of 400 mm x 500 mm and a two-pump system (with a rotary vane pump used for generating a coarse vacuum and a subsequent turbo pump for creating a finer vacuum).

The operational temperature range in stratospheric conditions is -40 °C to 40 °C. Critical with regard to outgassing is the maximum expected temperature. The maximum temperature of the testing platform reachable in the given TVC is 90°C, which is, given the operational temperature range, enough to gain reliable results.

The expected pressure at flight altitude is down to approx. 3 mbar. This coincides well with the minimum pressure of approx. 1 mbar reachable in the TVC with only one pump operating, so that the tests were carried out in this configuration.

2.2 TEST SETUP

2.2.1 Overview

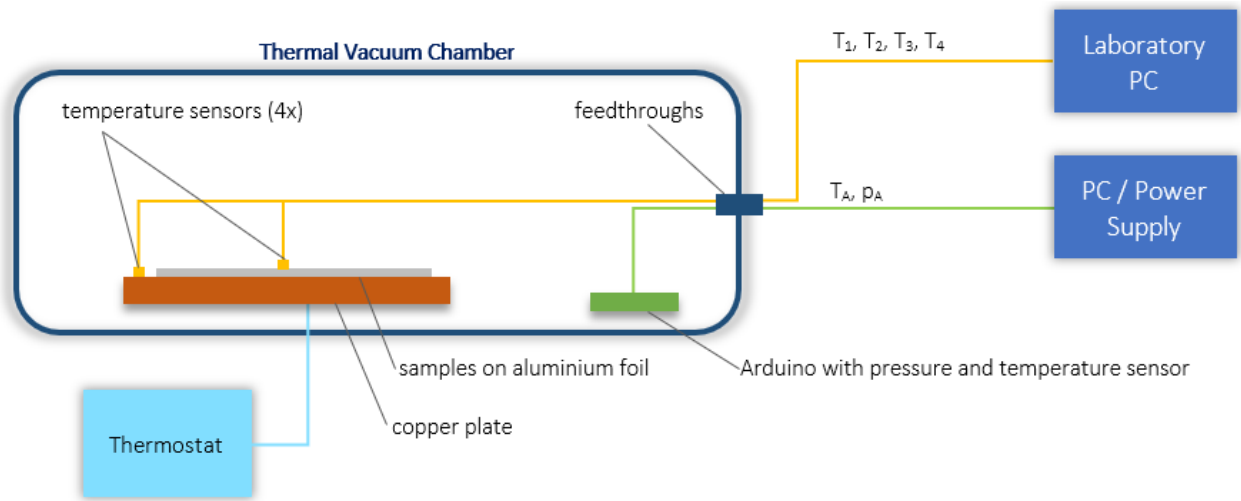

Figure 2.1: Sketch of the test setup in the thermal vacuum chamber

As shown in Figure 2.1, the aluminium foil paint samples were located inside the TVC, directly on a copper plate whose temperature could be controlled by a thermostat outside of the chamber. To measure the temperature distribution, four temperature sensors in total were distributed over the copper plate and the sample and were recorded by a laboratory computer. Additionally, an Arduino board with a pressure and a temperature sensor was put inside the chamber to provide a combined measurement of the temperature and pressure inside of the chamber. The samples were clamped on the copper plate using washers and screws.

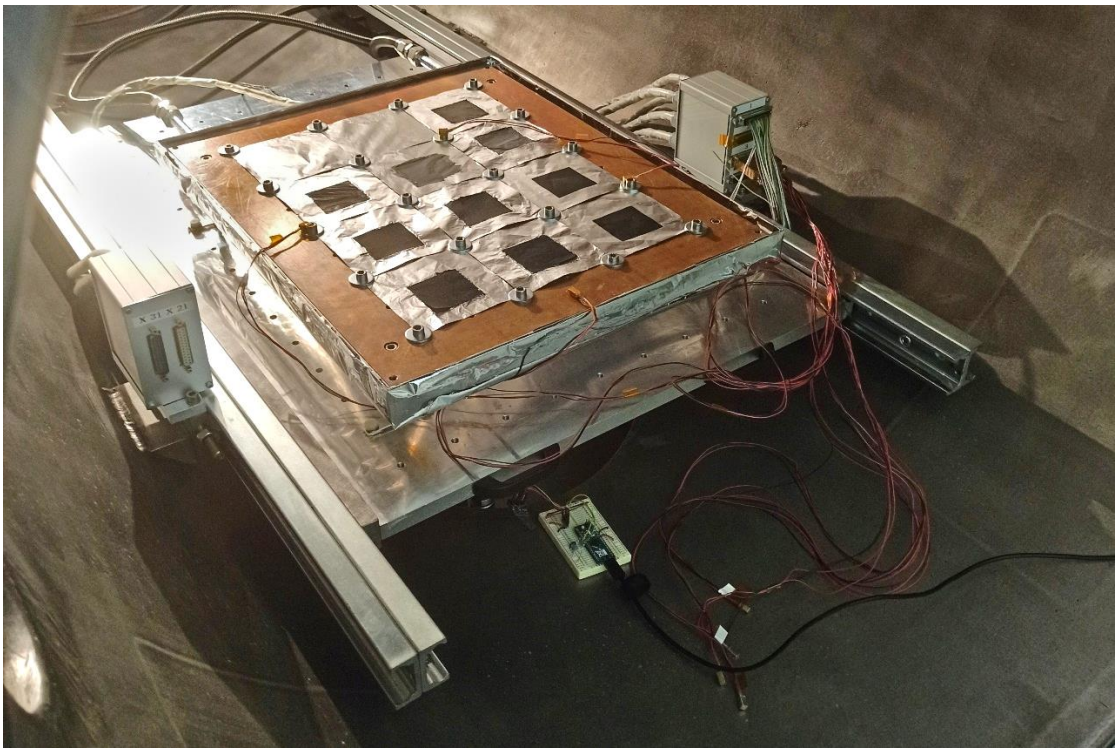

Figure 2.2: Test setup in the thermal vacuum chamber

2.2.2 Temperature Sensors

Four temperature sensors were used to record temperatures throughout the tests, three on the samples and one the copper plate, as shown in Figure 2.3.

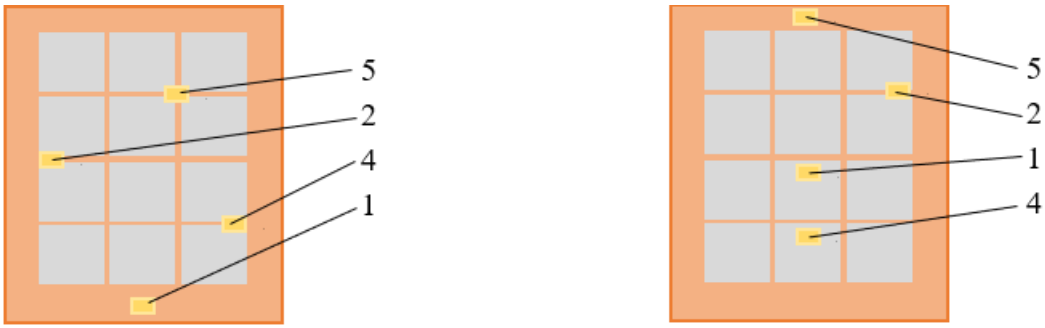

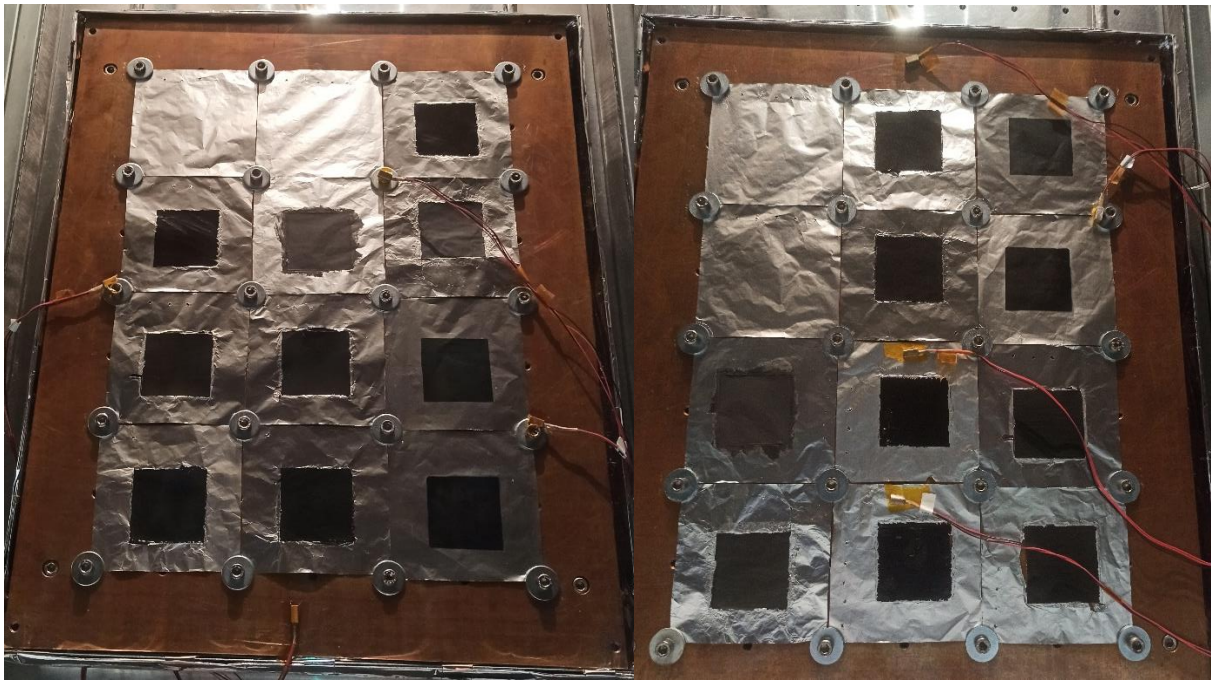

Figure 2.3: Sensor Application (left: Bakeout, right: Outgassing)

2.2.3 Scale

The scale used for the mass measurements is model AUW220D by Shimadzu. The standard deviation for this model is given as $\sigma \leq 0.1\ mg$. [RD2]

A reference measurement to determine the accuracy by two successive measurement series of each sample gives an average deviation of 0.07 mg to the mean value. This value confirms the given standard deviation. To follow a conservative approach, a deviation of 0.1 mg is used for error estimation.

2.3 TEST PROCEDURE OVERVIEW

Thermal vacuum outgassing tests are conducted according to ECSS-Q-ST-70-02C [RD1]. The variable names are chosen in accordance with that standard.

2.3.1 Sample Preparation

The process of sample preparation and initial measurements is shown in Figure 2.4.

Step 4 “Apply paint to sample holders” is different for each paint sample. See section 3.1.2 for the detailed processes.

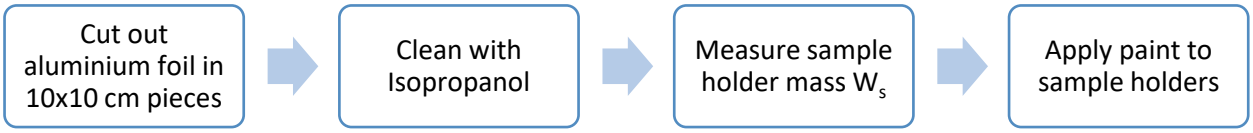

Figure 2.4: Flow chart of specimen preparation

2.3.2 Test Process

The test process shown in Figure 2.5 is the same for the bakeout and the outgassing procedure. Therefore, it needs to be performed two times.

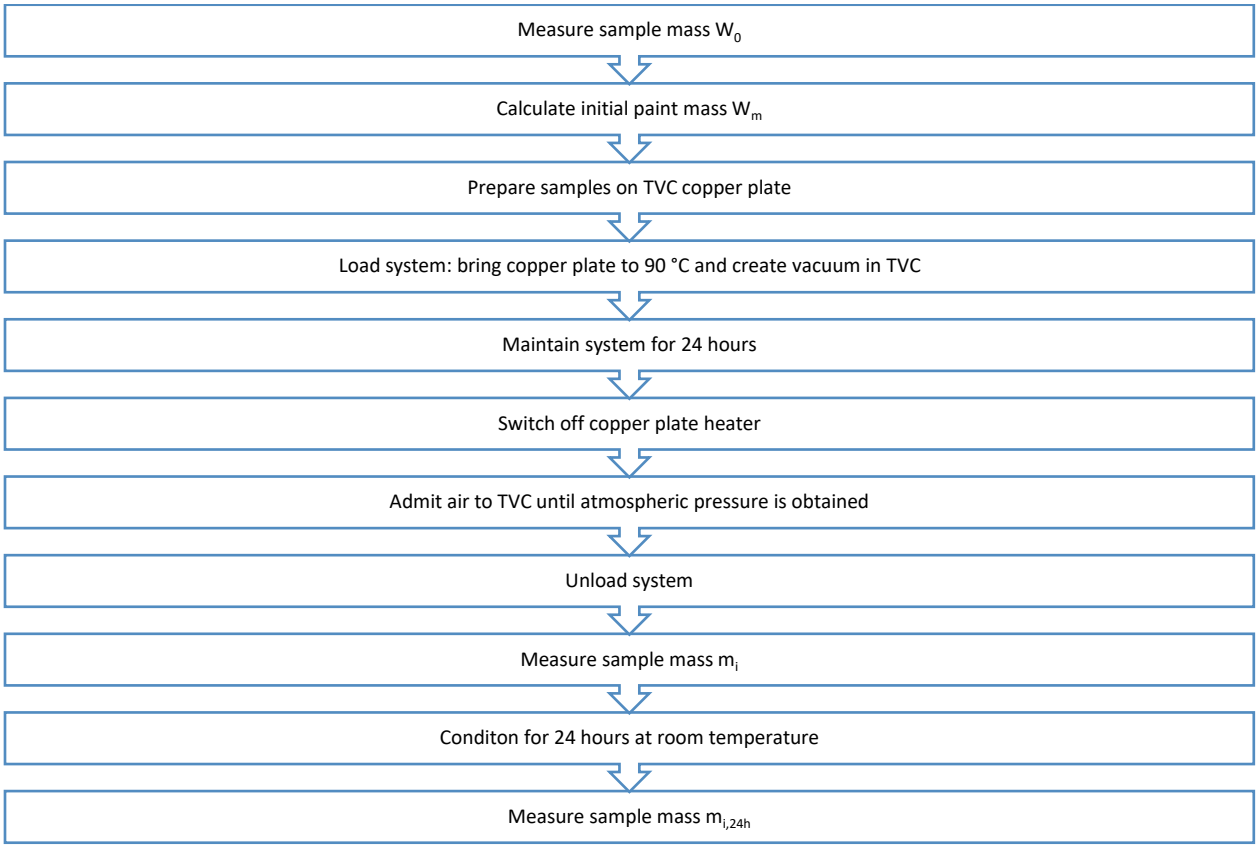

Figure 2.5: Flow chart of test process

2.4 SUCCESS CRITERIA

Recovered mass loss (RML):	<1%
Total mass loss (TML):	<1%
Maximum limits on standard deviation (according to ECSS-Q-ST-70-02C)	
TML	0.05%
RML	0.05%

3 DETAILED TEST PROCEDURE

3.1 PREPARATION

3.1.1 Sample Holders

The sample holders are cut out of aluminium foil in 10 x 10 cm large pieces. Depending on the sample's number, a corresponding number of holes are pierced through the foil, starting in the top left corner going to the right. There are two samples for each paint, specified as "0" and "1". For the "x-1" samples there is an additional hole in the bottom right corner, as shown in Figure 3.1.

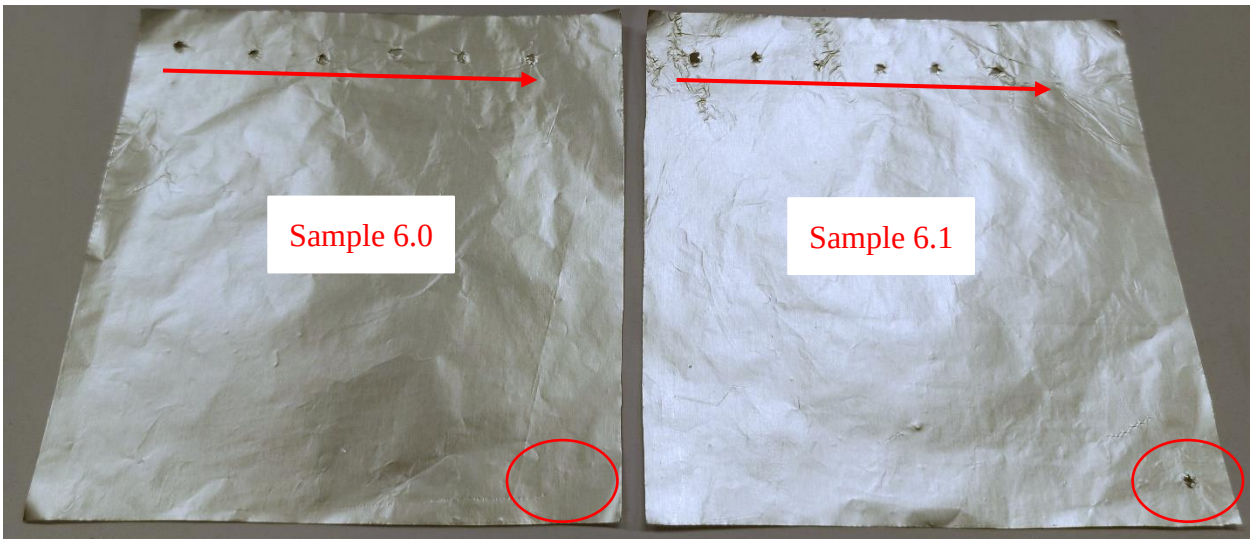

Figure 3.1: Sample identification scheme

3.1.2 Paint Application

First, the samples are cleaned with isopropanol, then they are put into cardboard stencils, which allow them to be handled more easily and to get an equal 5x5 cm square of paint on all samples.

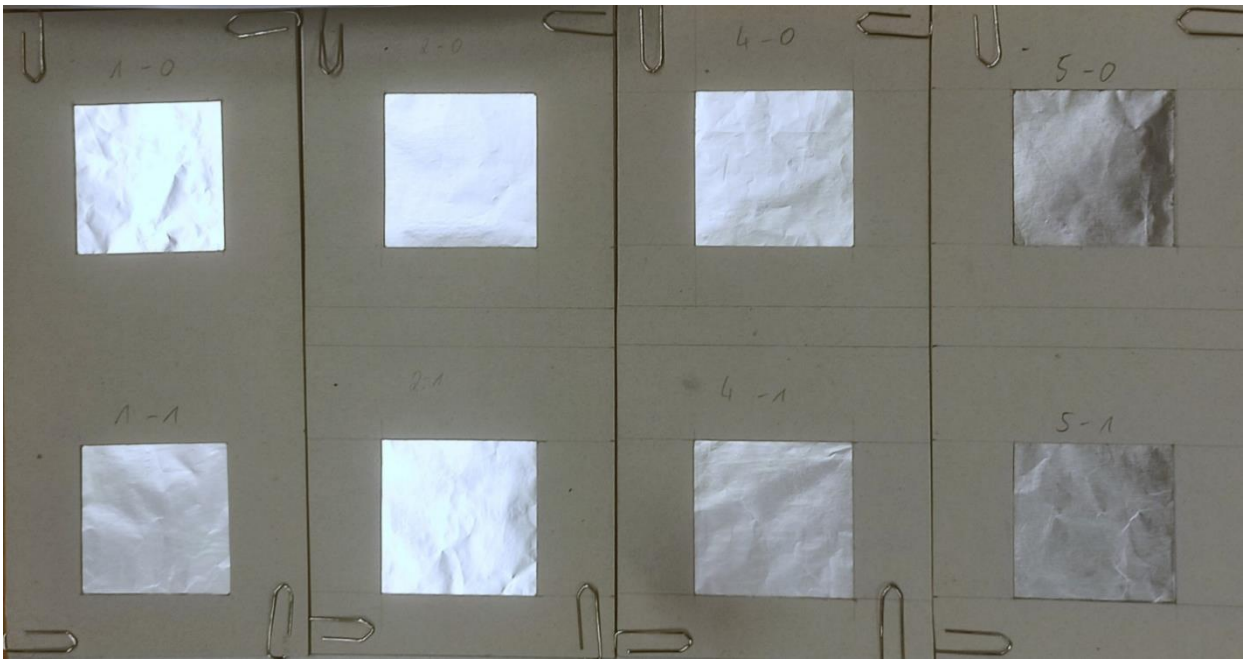

Figure 3.2: Cardboard stencils for paint application

The paints differ in their application methods; therefore, each is listed separately in the following table:

Table 1: Paint application method

Item No.	Name	Paint Application Method
1.x	Tetenal Camera Varnish Spray	- spraypainted
2.x	Black 3.0	- basecoat of Black 2.0 with brush, dried overnight - topcoat of Black 3.0 with brush, dried overnight - second topcoat of Black 3.0, dried overnight
4.x	"Schultafellack" mixed with flour	- 1:1 mix of paint and flour type 405 applied with brush
5.x	Glyptal Paint Black (10021-1)	- applied with brush
6.x	Aluminium reference sample	- no paint applied
7.0	Nextel Suede Black	- basecoat of NEXTEL Primer 5523 (anthracite) + 10% hardener (10:1) + 20% (of total) thinner - put under vacuum (~3 mbar) for 1.5 h after coating (ca. 10-15 min delay) - baked at 110 °C for 1 h after ~2 days. - topcoat of NEXTEL Suede Black (with additional hardener (8:1) +10% (of total) thinner - put under vacuum (~3 mbar) for 1 h after coating. - all applied with brush
7.1	Nextel Suede Black	- basecoat of NEXTEL Primer 5523 (anthracite) + 10% hardener (10:1) + 20% (of total) thinner - baked at 110 °C for 1 h after ~ 2 days - NO vacuum curing - topcoat of NEXTEL Suede Black + hardener (8:1) + 10% (of total) thinner. - NO vacuum curing. - All applied with brush

3.1.3 Initial Measurements

W_s ……. Substrate Mass

Table 2: Initial sample holder mass measurement [mg]

Item No.	Description	W_s
1.0	Tetenal Camera Varnish Spray	330.35
1.1	Tetenal Camera Varnish Spray	334.55
2.0	Black 3.0	326.97
2.1	Black 3.0	326.90
4.0	Schultafellack mixed with flour	325.53
4.1	Schultafellack mixed with flour	330.24
5.0	Glyptal Paint Black (10021-1)	322.80
5.1	Glyptal Paint Black (10021-1)	317.24
6.0	Aluminium reference sample	326.78
6.1	Aluminium reference sample	329.37
7.0	Nextel Suede Black	326.30
7.1	Nextel Suede Black	325.04

3.2 PHASE 1: BAKEOUT

Conducted from 05.08.2020 to 07.08.2020.

3.2.1 Protocol

The test follows the procedure as in Figure 2.5. The protocolled steps during this test are:

05.08.2020:

- 13:00 vacuum pump on, pressure decrease
- 13:30 0.155 mbar
- vacuum pump continues working overnight

06.08.2020:

- 12:51 temperature back at 20°C
- 12:52 open pressure valve
- 12:57 room pressure in TVC
- 13:19 samples removed from TVC
- 13:40 mass measurements

07.08.2020:

- 13:00 mass measurements

3.2.2 Temperature and Pressure Curves

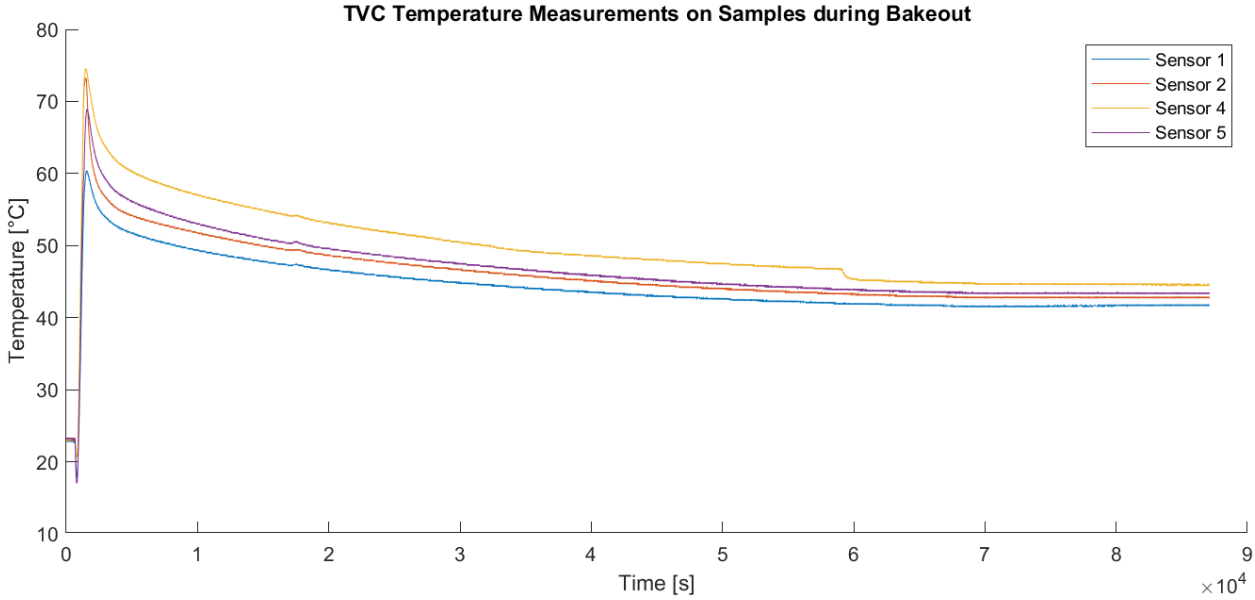

Figure 3.3: Temperatures during bakeout on the copper plate

The temperature of the copper plate was set to 90°C for the whole time but as the diagram shows the sensors did not measure that temperature. This could be due to the fixation of the sensors on the washers, instead of directly on the samples. Also, sensor 1 was not fixated properly on the copper plate and therefore had air between itself and the plate. Therefore, it is assumed that the measured temperature does not correspond with the real sample temperature.

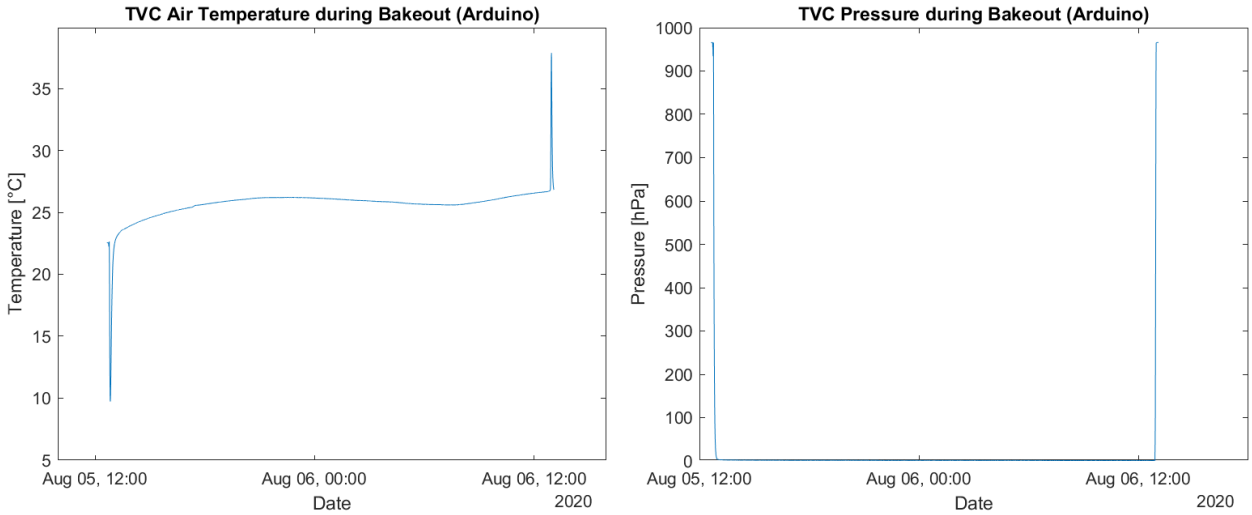

Figure 3.4: Temperature and pressure in the chamber (Arduino)

3.2.3 Measurements

W_{01} ……. Total specimen mass before bakeout
W_{m1} ……. Material (paint) mass before bakeout $W_{m1} = W_{01} - W_s$
W_{f1} ……. Total specimen mass just after bakeout
W_{r1} ……. Total specimen mass after bakeout and after 24 hours

Table 3: Bakeout measurements [mg]

Item No.	Description	W_{01}	W_{m1}	W_{f1}	W_{r1}
1.0	Tetenal Camera Varnish Spray	357.04	26.69	356.44	356.96
1.1	Tetenal Camera Varnish Spray	369.75	35.20	368.74	369.30
2.0	Black 3.0	476.00	149.03	469.13	470.35
2.1	Black 3.0	481.91	155.01	474.29	475.35
4.0	Schultafellack mixed with flour	1040.70	715.17	1019.10	1032.40
4.1	Schultafellack mixed with flour	967.24	637.00	949.65	961.06
5.0	Glyptal Paint Black (10021-1)	547.42	224.62	544.50	545.72
5.1	Glyptal Paint Black (10021-1)	537.25	220.01	533.89	535.12
6.0	Aluminium reference sample	328.29	328.29*	328.18	328.55
6.1	Aluminium reference sample	330.93	330.93*	330.85	331.22
7.0	Nextel Suede Black	606.19	279.89	605.05	605.77
7.1	Nextel Suede Black	616.62	291.58	614.69	615.62

*As the aluminium does not carry any paint, W_{m1} is set equal to W_{01} to determine how much of the weightloss might come from the substrate itself.

3.2.4 Screening Properties

Table 4: Bakeout screening properties - calculation formulas

TML_1	Total Mass Loss during bakeout	$TML_1 = \frac{W_{01} - W_{f1}}{W_{m1}}$
RML_1	Recovered Mass Loss during bakeout	$RML_1 = \frac{W_{01} - W_{r1}}{W_{m1}}$
WVR_1	Water Vapor Regained after 24h at room atmosphere	$WVR_1 = \frac{W_{r1} - W_{f1}}{W_{m1}}$
$\lvert\Delta_{max}\rvert$	Max. error due to error propagation for $f = \frac{a-b}{c}$ with $\Delta a = \Delta b = \Delta c = 0.1\ mg$*	$\lvert\Delta_{max,f}\rvert = \left\lvert\frac{1}{c}\right\rvert \Delta a + \left\lvert\frac{1}{c}\right\rvert \Delta b + \left\lvert\frac{b-a}{c^2}\right\rvert \Delta c$

*see 2.2.3

Table 5: Calculation of bakeout screening properties and maximum error

Item No.	TML_1	$\lvert\Delta_{max,TML1}\rvert$	RML_1	$\lvert\Delta_{RML1}\rvert$	WVR_1	$\lvert\Delta_{WVR1}\rvert$
1.0	2.248%	0.758%	0.300%	0.750%	1.948%	0.757%
1.1	2.869%	0.576%	1.278%	0.572%	1.591%	0.573%
2.0	4.610%	0.137%	3.791%	0.137%	0.819%	0.135%
2.1	4.916%	0.132%	4.232%	0.132%	0.684%	0.129%
4.0	3.020%	0.028%	1.161%	0.028%	1.860%	0.028%
4.1	2.761%	0.032%	0.970%	0.032%	1.791%	0.032%
5.0	1.300%	0.090%	0.757%	0.089%	0.543%	0.089%
5.1	1.527%	0.092%	0.968%	0.091%	0.559%	0.091%
6.0	0.034%	0.061%	-0.079%	0.061%	0.113%	0.061%
6.1	0.024%	0.061%	-0.088%	0.061%	0.113%	0.061%
7.0	0.407%	0.072%	0.150%	0.072%	0.257%	0.072%
7.1	0.662%	0.069%	0.343%	0.069%	0.319%	0.069%

As Table 5 shows, the reference sample's mass loss during the Bakeout is much smaller than all the paint's mass losses and is in the range of measurement uncertainties. Therefore, it is considered negligible in further calculations.

3.2.5 Notations

During the TVC procedure, the Glyptal paint samples form bubbles of trapped air. By choosing another application method other than a paint brush, it could be possible to create a thinner layer of paint that does not trap any air inside. If the final application to the straylight protection shield relies on paint brushes, the Glyptal paint is not considered as suitable for the process.

Also, some other samples get fine cracks or deform as in some cases the aluminium foil was damaged while removing the cardboard stencils from the samples.

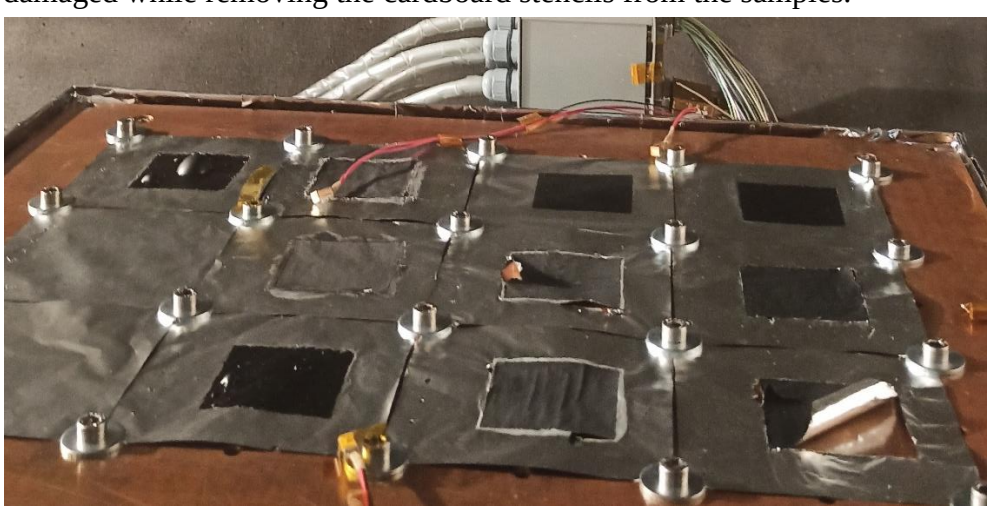

Figure 3.5: Bubbles and deformation of samples during TVC procedure

3.3 PHASE 2 - OUTGASSING

Conducted from 12.08.2020 to 14.08.2020.

3.3.1 Protocol

The test follows the procedure as in Figure 2.5. The protocolled steps during this test are:

12.08.2020:

- 16:32 start data recording on Arduino, forgot time stamp → 16:39 with time stamp
- 16:33 start temperature recording on lab PC
- 16:35 start heating
- 16:37 vacuum pump on, pressure decrease
- vacuum pump continues working overnight

13.08.2020:

- 16:56 open pressure valve
- 16:58 room pressure
- 17:09 stop data recording
- 17:15 samples removed from TVC

14.08.2020:

- 17:00 mass measurements

3.3.2 Temperature and Pressure Curves

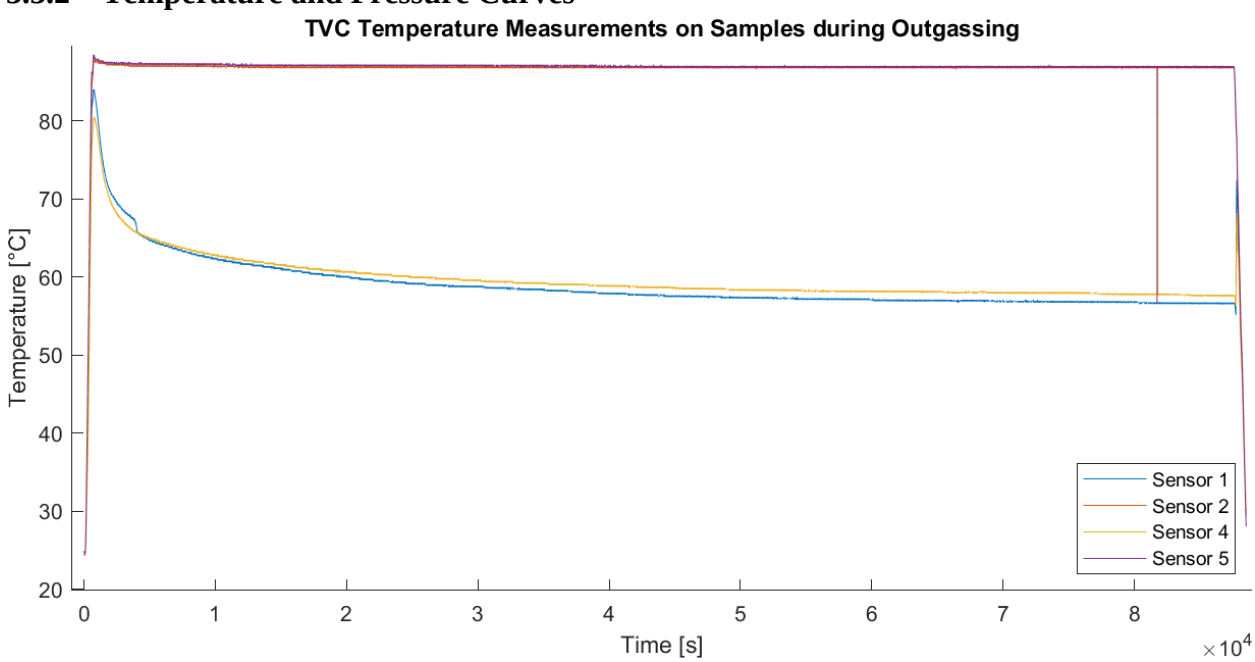

Figure 3.6: Temperature during outgassing on the copper plate

This time, sensors 2 and 5 were fixated properly but in sensors 1 and 4 the temperature again does not match the copper plate temperature. Those sensors were fixated directly to two samples. Due to a slight twist in the cables, the sensors as well as the sample area around them were slightly lifted from the copper plate, which might explain the deviation from the target temperature. It is assumed that the samples reached the temperature as set.

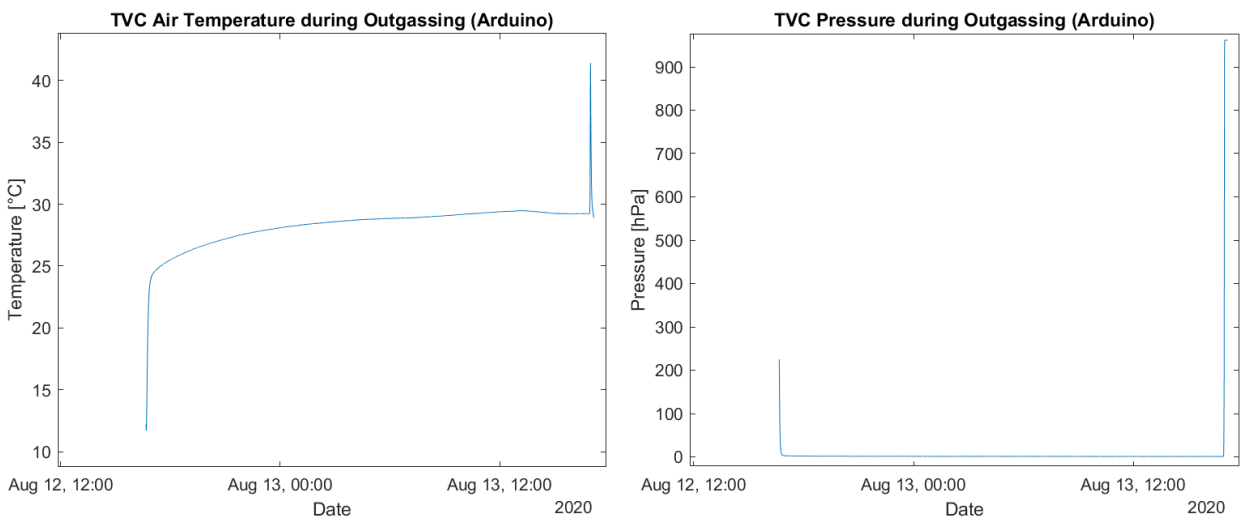

Figure 3.7: Temperature and pressure during outgassing in the chamber (Arduino)

3.3.3 Measurements

W_{02} ……. Total specimen mass before outgassing
W_{m2} ……. Material (paint) mass before outgassing: $W_{m2} = W_{02} - W_s$
W_{f2} ……. Total specimen mass just after outgassing
W_{r2} ……. Total specimen mass after outgassing and after 24 hours

Table 3: Outgassing measurements [mg]

Item No.	Description	W_{02}	W_{m2}	W_{f2}	W_{r2}
1.0	Tetenal Camera Varnish Spray	356.52	26.17	356.46	356.66
1.1	Tetenal Camera Varnish Spray	368.85	34.30	368.67	369.03
2.0	Black 3.0	470.10	143.13	470.16	470.38
2.1	Black 3.0	475.18	148.28	475.02	475.52
4.0	Schultafellack mixed with flour	1030.66	705.13	1020.92	1034.03
4.1	Schultafellack mixed with flour	957.88	627.64	953.27	961.84
5.0	Glyptal Paint Black (10021-1)	544.68	221.88	544.56	544.90
5.1	Glyptal Paint Black (10021-1)	534.86	217.62	534.09	534.71
6.0	Aluminium reference sample	328.17	1.39	328.36	328.25
6.1	Aluminium reference sample	330.85	1.48	330.76	330.88
7.0	Nextel Suede Black	605.50	279.20	605.60	606.02
7.1	Nextel Suede Black	615.13	290.09	615.44	615.78

3.3.4 Screening Properties

Table 6: Outgassing Screening Properties – Calculation Formulas

TML_2	Total Mass Loss during outgassing	$TML_2 = \frac{W_{02} - W_{f2}}{W_{m2}}$
RML_2	Recovered Mass Loss during outgassing	$RML_2 = \frac{W_{02} - W_{r2}}{W_{m2}}$
WVR_2	Water Vapor Regained after 24h at room atmosphere	$WVR_2 = \frac{W_{r2} - W_{f2}}{W_{m2}}$
$\lvert\Delta_{max}\rvert$	Max. error due to error propagation for $f = \frac{a-b}{c}$ with $\Delta a = \Delta b = \Delta c = 0.1\ mg$*	$\lvert\Delta_{max,f}\rvert = \left\lvert\frac{1}{c}\right\rvert \Delta a + \left\lvert\frac{1}{c}\right\rvert \Delta b + \left\lvert\frac{b-a}{c^2}\right\rvert \Delta c$

*see 2.2.3

Table 7: Calculation of outgassing screening properties and maximum error

Item No.	TML_2	$\lvert\Delta_{max,TML}\rvert$	RML_2	$\lvert\Delta_{RML2}\rvert$	WVR_2	$\lvert\Delta_{WVR2}\rvert$
1.0	0.229%	0.765%	-0.535%	0.766%	0.764%	0.767%
1.1	0.525%	0.585%	-0.525%	0.585%	1.050%	0.586%
2.0	-0.042%	0.140%	-0.196%	0.140%	0.154%	0.140%
2.1	0.108%	0.135%	-0.229%	0.135%	0.337%	0.135%
4.0	1.381%	0.029%	-0.478%	0.028%	1.859%	0.029%
4.1	0.734%	0.032%	-0.631%	0.032%	1.365%	0.032%
5.0	0.054%	0.090%	-0.099%	0.090%	0.153%	0.090%
5.1	0.354%	0.092%	0.069%	0.092%	0.285%	0.092%
6.0	-0.058%	0.061%	-0.024%	0.061%	-0.034%	0.061%
6.1	0.027%	0.060%	-0.009%	0.060%	0.036%	0.060%
7.0	-0.036%	0.072%	-0.186%	0.072%	0.150%	0.072%
7.1	-0.107%	0.069%	-0.224%	0.069%	0.117%	0.069%

3.3.5 Notations

Sample 1.0 got in contact with the superglue that was used to stick the temperature sensors to their respective surface. Also, the adhesive tape from one of the sensors could not be completely removed from sample 5.0. The mass measurements of those samples could therefore be influenced by residues of the superglue or the adhesive tape respectively.

4 EVALUATION

4.1 PAINT MASS LOSS IN PERCENTAGE OF ORIGINAL PAINT MASS

The following diagrams show the mass development over the steps of the experiment:

1: before bakeout, **2:** after bakeout, **3:** 24h after bakeout
4: before outgassing, **5:** after outgassing, **6:** 24h after outgassing

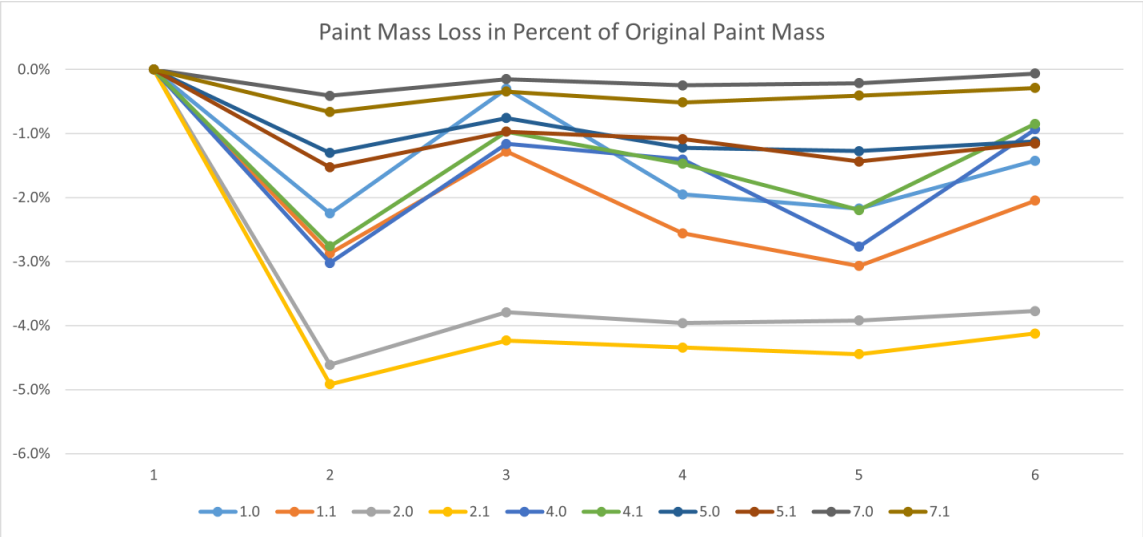

Figure 4.1: Paint mass loss of all samples

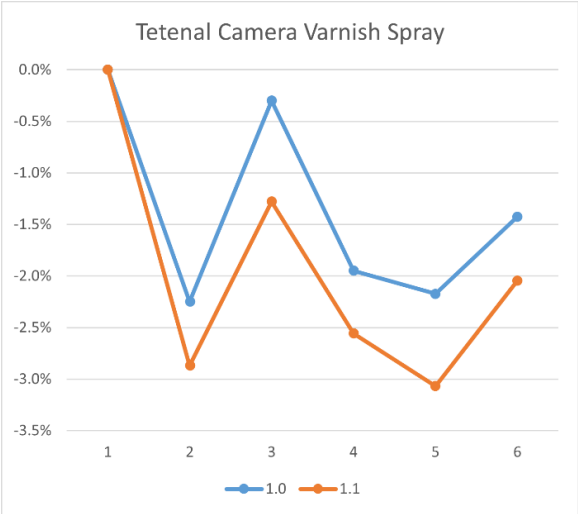

Figure 4.2: Paint mass loss of samples 1.x

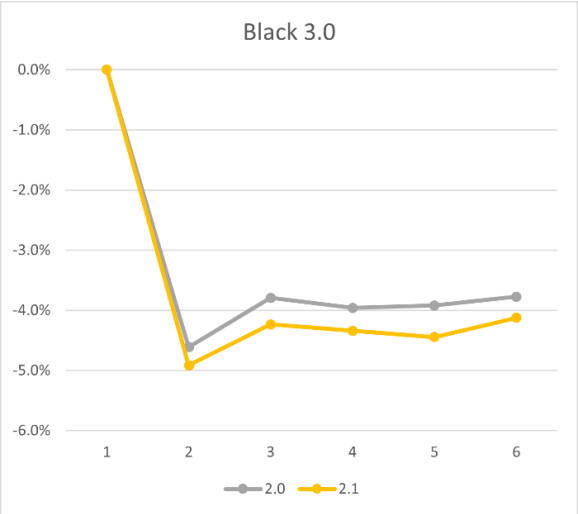

Figure 4.3: Paint mass loss of samples 2.x

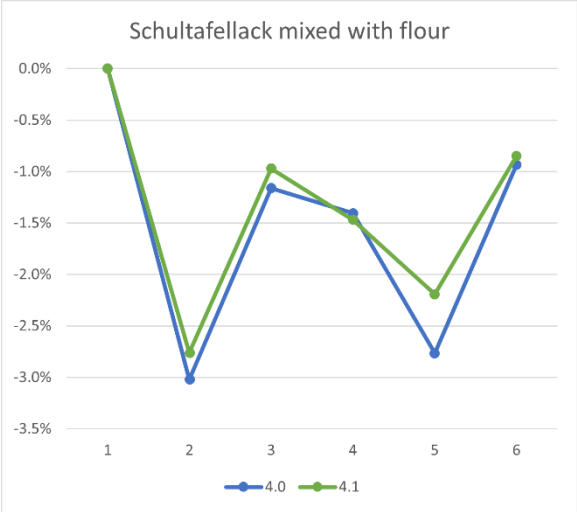

Figure 4.4: Paint mass loss of samples 4.x

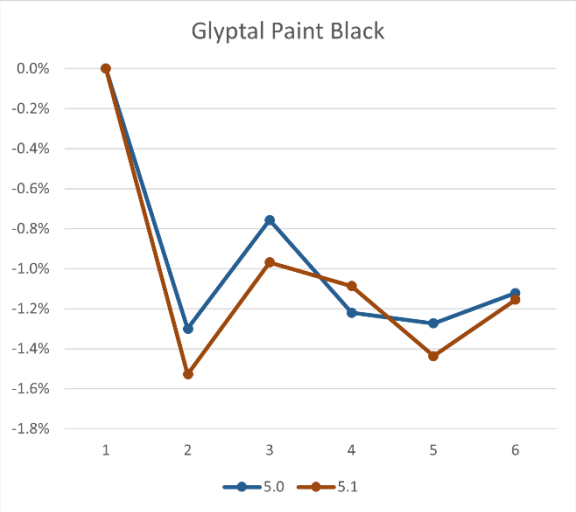

Figure 4.5: Paint mass loss of samples 5.x

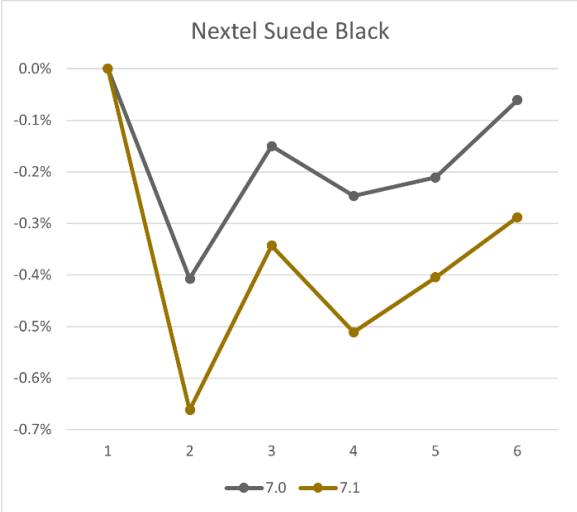

Figure 4.6: Paint mass loss of samples 7.x

4.2 SCREENING PROPERTIES

The following diagrams show the screening properties in percent as calculated in chapters 3.2.4 and 3.3.4 for each sample.

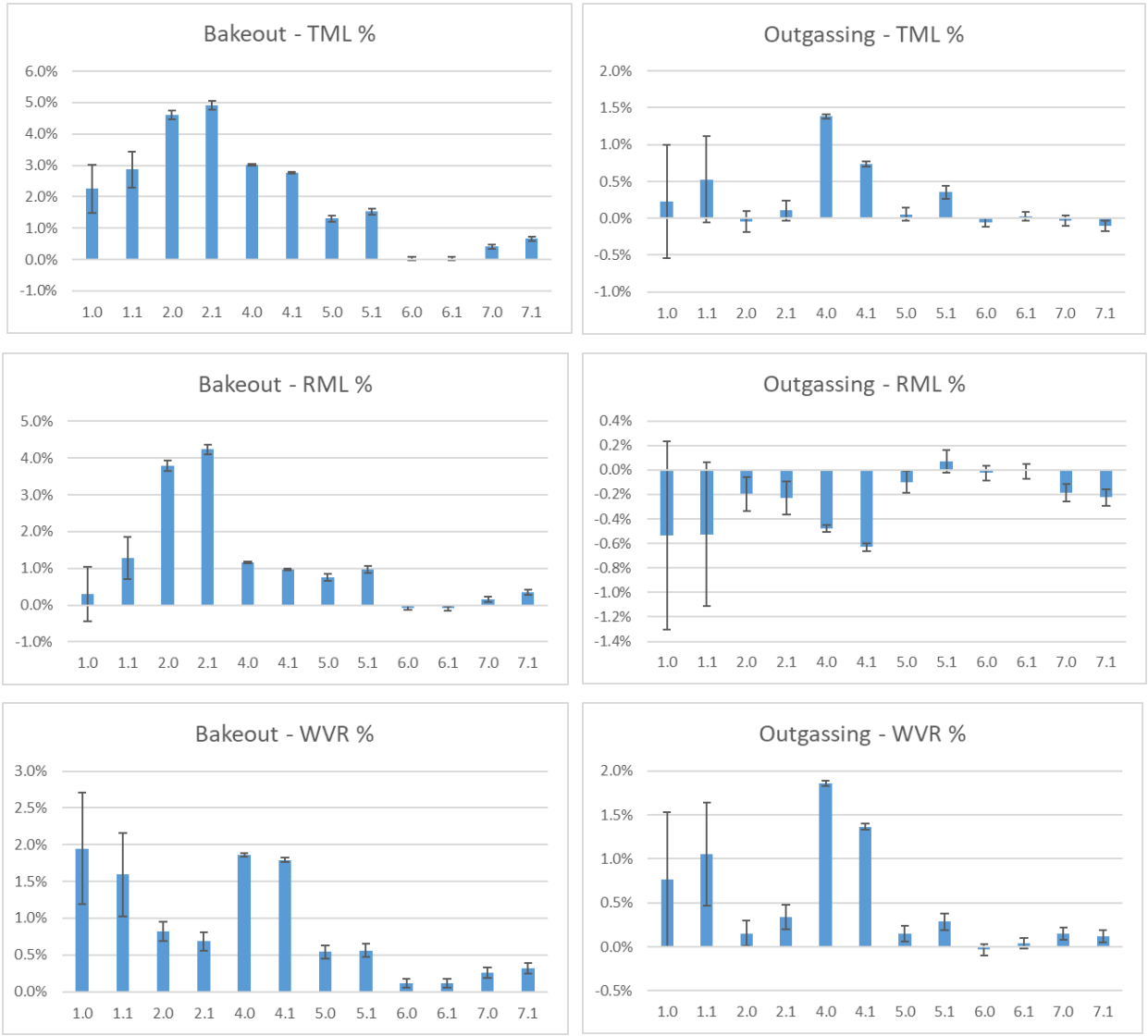

Figure 4.7: Graphical representation of screening properties

5 RESULTS

The success criteria are, as defined earlier, RML and TML getting lower than 1 %. The following tables compare the results of both phases to those criteria. Green marks compliance with the success criteria, yellow marks a potential compliance as the maximum error would lead to non-compliance.

Table 8: Comparison of bakeout trial values with success criteria.

Sample No.	Description	$TML_1 + \Delta TML_1$ [%]		$RML_1 + \Delta RML_1$ [%]		Outgassed mass / area [mg/cm²]
1	Tetenal Camera Varnish Spray	2.559	±0.667	0.789	±0.661	0.0322
2	Black 3.0	4.763	±0.135	4.012	±0.134	0.2898
4	Schultafellack mixed with flour	2.891	±0.030	1.065	±0.030	0.7838
5	Glyptal Paint Black (10021-1)	1.414	±0.091	0.862	±0.090	0.1256
6	Aluminium reference sample	0.029	±0.061	-0.084	±0.061	-
7	Nextel Suede Black	0.535	±0.070	0.247	±0.070	0.0614

Table 9: Comparison of outgassing-after-bakeout trial values with success criteria.

Sample No.	Description	$TML_1 + \Delta TML_1$ [%]		$RML_1 + \Delta RML_1$ [%]		Outgassed mass / area [mg/cm²]
1	Tetenal Camera Varnish Spray	0.377	±0.675	-0.530	±0.675	0.0048
2	Black 3.0	0.033	±0.137	-0.212	±0.137	0.0020
4	Schultafellack mixed with flour	1.058	±0.030	-0.554	±0.030	0.2870
5	Glyptal Paint Black (10021-1)	0.204	±0.091	-0.015	±0.091	0.0178
6	Aluminium reference sample	-0.015	±0.061	-0.017	±0.061	-
7	Nextel Suede Black	-0.071	±0.070	-0.205	±0.070	-0.0082

The trials show that the bakeout procedure is essential to reach the demand of maximum 1% total and recovered mass loss, respectively. The outgassed mass/area columns clearly show a reduction of outgassed mass in the order of at least one magnitude, except for sample 4.

The *Schultafellack mixed with flour* was still not able to meet the requirements, even with the previous bakeout. The *Glyptal Paint Black* shows good results in the outgassing-after-bakeout trial but already got disqualified due to forming bubbles of trapped air inside of the TVC during the bakeout trial (see 3.2.5). *Tetenal Camera Varnish Spray* does comply with the result only if the maximum error is not met, and therefore is not considered optimal. *Nextel Suede Black* reaches the lowest outgassing values, followed by *Black 3.0*. Therefore, those two are the recommended choice for the straylight protection. However, for the final decision the results of the reflection tests need to be considered.

The Material Identification cards and Micro VCM Sheets of both trials are included in the appendix.

6 SUMMARY

This test procedure showed outgassing tests of non-reflective paint samples in a thermal vacuum chamber (TVC) at the Institute of Space Systems (IRS) of the University of Stuttgart. The objective was to evaluate the suitability of several paints for straylight protection hardware. Five different paints were tested by measuring their total and recovered mass losses during a bakeout trial and an outgassing-after-bakeout trial. It was shown that the bakeout is essential to reach the maximum allowed outgassing values, as for all samples but one only the outgassing-after-bakeout trials met the requirements of maximum total and recovered mass loss. The paints that are considered most suitable for the straylight protection hardware from an outgassing point of view were shown to be *Black 3.0* and *Nextel Suede Black.*

7 APPENDIX

Table 10: Micro VCM Sheet of Bakeout

Item no.	Commercial identification or standard designation	W_o total before	W_s substr.	W_m material before	W_f total after	W_r total cond.	TML %	RML %	WCR %	Observations
1	Tetenal Camera Varnish Spray	357.04	330.35	26.69	356.44	356.96	2.25	0.3	1.95	
		369.75	334.55	35.20	368.74	369.30	2.87	1.28	1.59	
						average	**2.56**	**0.79**	**1.77**	
2	Black 3.0	476.00	326.97	149.03	469.13	470.35	4.61	3.79	0.82	
		481.91	326.90	155.01	474.29	475.35	4.92	4.23	0.68	
						average	**4.77**	**4.01**	**0.75**	
4	Schultafellack mixed with flour	1040.70	325.53	715.17	1019.10	1032.40	3.02	1.16	1.86	
		967.24	330.24	637.00	949.65	961.06	2.76	0.97	1.79	
						average	**2.89**	**1.07**	**1.83**	
5	Glyptal Paint Black (10021-1)	547.42	322.80	224.62	544.50	545.72	1.30	0.76	0.54	Formed bubbles of trapped air
		537.25	317.24	220.01	533.89	535.12	1.53	0.97	0.56	
						average	**1.42**	**0.87**	**0.55**	
6	Aluminium Reference Sample	328.29	326.78	328.29	328.18	328.55	0.03	-0.08	0.11	
		330.93	329.37	330.93	330.85	331.22	0.02	-0.09	0.11	
						average	**0.03**	**-0.09**	**0.11**	
7	Nextel Suede Black	606.19	326.30	279.98	605.05	605.77	0.41	0.15	0.26	
		616.62	325.04	291.58	614.69	615.62	0.66	0.34	0.32	
						average	**0.54**	**0.25**	**0.29**	

Table 11: Micro VCM Sheet of Outgassing after Bakeout

Item no.	Commercial identification or standard designation	W_o total before	W_s substr.	W_m material before	W_f total after	W_r total cond.	TML %	RML %	WCR %	Observations
1	Tetenal Camera Varnish Spray	356.52	330.35	26.17	356.46	356.66	0.23	-0.53	0.76	
		368.85	334.55	34.30	368.67	369.03	0.52	-0.52	1.05	
	Instant glue drop could not be removed completely from sample 1					**average**	**0.38**	**-0.53**	**0.91**	
2	Black 3.0	470.10	326.97	143.13	470.16	470.38	-0.04	-0.20	0.15	
		475.18	326.90	148.28	475.02	475.52	0.11	-0.23	0.34	
						average	**0.04**	**-0.22**	**0.25**	
4	Schultafellack mixed with flour	1030.66	325.53	705.13	1020.92	1034.03	1.38	-0.48	1.86	
		957.88	330.24	627.64	953.27	961.84	0.73	-0.63	1.37	
						average	**1.06**	**0.56**	**1.62**	
5	Glyptal Paint Black (10021-1)	544.68	322.80	221.88	544.56	544.90	0.05	-0.10	0.15	
		534.86	317.24	217.62	534.09	534.71	0.35	0.07	0.28	
	Tape was not completely removable from sample 1 after TVC					**average**	**0.2**	**0.3**	**0.22**	
6	Aluminium Reference Sample	328.17	326.78	328.17	328.36	328.25	-0.06	-0.02	-0.03	
		330.85	329.37	330.85	330.76	330.88	0.03	-0.01	0.04	
						average	**-0.01**	**-0.02**	**0.01**	
7	Nextel Suede Black	605.50	326.30	279.20	605.6	606.02	-0.04	-0.19	0.15	
		615.13	325.04	290.09	615.44	615.78	-0.11	-0.22	0.12	
						average	**-0.08**	**-0.21**	**0.14**	

Preparation details in *e.)* only describe the processing steps taken before the outgassing trial, and don't include the steps of the outgassing trial itself.

Material identification card			
Sample description and history a. Trade name + number b. Manufacturer c. Type of product d. Chemical nature e. Preparation details: e.g. - joining method - heat treatment - cure and postcure - cleaning method - relevant spec. no	a. Tetenal Camera Varnish Spray	b. Tetenal	
	c. Spray-paint, black	d.	
	e. Cleaned with IPA Spray-painted Outbake for 24h in TVC Left at room atmosphere for 24 hours		
Sample quantity / sample size / paint area Preparation date Prepared by	2 / 10 x 10 cm / 5 x 5 cm 30/07/20 J. Böttger	Material density Substrate density Substrate material	Unknown 2,70 kg/m³ Aluminium foil 13 µm
Application	Spray-painted		
	Type: Results	Average of evaluation and control sample TML = 0.377 +/- 0.675 % RML = -0.530 +/- 0.675 % ❑ Accept ❑ Reject	

Material identification card			
Sample description and history a. Trade name + number b. Manufacturer c. Type of product d. Chemical nature e. Preparation details: e.g. - joining method - heat treatment - cure and postcure - cleaning method - relevant spec. no	a. Black 3.0	b. CultureHustle	
	c. Paint, black	d.	
	e. Cleaned with IPA Base Coat of Black 2.0, dried overnight Topcoat of Black 3.0, dried overnight Second Topcoat of Black 3.0, dried overnight Outbake for 24h in TVC Left at room atmosphere for 24 hours		
Sample quantity / sample size / paint area Preparation date Prepared by	2 / 10 x 10 cm / 5 x 5 cm 27/07/20 J. Böttger	Material density Substrate density Substrate material	Unknown 2,70 kg/m³ Aluminium foil 13 µm
Application	Paint Brush		
	Type: Results:	Average of evaluation and control sample TML = 0.0330 +/- 0.137 % RML = -0.212 +/- 0.137 % ❑ Accept ❑ Reject	

Material identification card			
Sample description and history a. Trade name + number b. Manufacturer c. Type of product d. Chemical nature e. Preparation details: e.g. - joining method - heat treatment - cure and postcure - cleaning method - relevant spec. no	a. Schultafellack + flour		b. albrecht
	c. Paint, black, flour		d.
	e. Cleaned with IPA Mix ratio: 1 : 1, paint : flour type 405, dried overnight Bakeout for 24h in TVC Left at room atmosphere for 24 hours		
Sample quantity / sample size / paint area Preparation date Prepared by	2 / 10 x 10 cm / 5 x 5 cm 27/07/20 J. Böttger	Material density Substrate density Substrate material	Unknown 2,70 kg/m³ Aluminium foil 13 µm
Application	Paint Brush		
	Type: Average of evaluation and control sample Results: TML = 1.06 +/- 0.0303 % RML = 0.554 +/- 0.0302 % ❑ Accept ❑ Reject		

Material identification card			
Sample description and history a. Trade name + number b. Manufacturer c. Type of product d. Chemical nature e. Preparation details: e.g. - joining method - heat treatment - cure and postcure - cleaning method - relevant spec. no	a. Glyptal Paint Black		b. Glyptal
	c. Paint, black		d.
	e. Cleaned with IPA painted, dried overnight Bakeout for 24h in TVC Left at room atmosphere for 24 hours		
Sample quantity / sample size / paint area Preparation date Prepared by	2 / 10 x 10 cm / 5 x 5 cm 27/07/20 J. Böttger	Material density Substrate density Substrate material	Unknown 2,70 kg/m³ Aluminium foil 13 µm
Application	Paint Brush		
	Type: Average of evaluation and control sample Results: TML = 0.204 +/- 0.0911 % RML = -0.0151 +/- 0.0911 % ❑ Accept ❑ Reject		
Material identification card			

Sample description and history a. Trade name + number b. Manufacturer c. Type of product d. Chemical nature e. Preparation details: e.g. - joining method - heat treatment - cure and postcure - cleaning method - relevant spec. no	a. Nextel Suede Black	b. Mankiewicz	
	c. Paint, black	d.	
	e. Cleaned with IPA Base coat: Nextel Primer 5523 : hardener + thinner → 10:1 + 20% Sample .0 : 1.5 h of vacuum curing, Sample .1 : no vacuum curing Baked at 110 °C for 1 h Top coat: Nextel Suede Black : hardener + thinner → 8:1 + 10% Sample .0 : 1 h of vacuum curing, Sample .1 : no vacuum curing Bakeout for 24h in TVC Left at room atmosphere for 24 hours		
Sample quantity / sample size / paint area Preparation date Prepared by	2 / 10 x 10 cm / 5 x 5 cm 27/07/20 J. Böttger	Material density Substrate density Substrate material	Unknown 2,70 kg/m³ Aluminium foil 13 µm
Application	Paint Brush		
	Type: Average of evaluation and control sample Results: TML = -0.0713 +/- 0.0703 % RML = -0.205 +/- 0.0704 % ❑ Accept ❑ Reject		

STU-IRS-E-PRO-1230-01-v1.2_TV-Test Report PCO Edge_AsRun_2019-10-21

THERMAL VACUUM TEST OF PCO EDGE 4.2 CAMAERA

Version 1.2

21.10.2019

Status: As run

H2020 INFRADEV-01-2017 project "European Stratospheric Balloon Observatory *Design Study*"

Topic: INFRADEV-01-2017 Design Studies

Project Title: European Stratospheric Balloon Observatory *Design Study* – ESBO *DS*

Proposal No: 777516 – ESBO DS

Duration: Mar 1, 2018 - Feb 28, 2021

WP (EU)	WP 10
WBS Item (internal)	650
PBS Item(s)	1200
Title	Thermal Vacuum Test of pco.edge 4.2 Camera
Description	Test of a pco.edge 4.2 Camera in thermal vacuum chamber
Lead Beneficiary	"USTUTT"
Nature	"Report"
Dissemination Level	"Public"
Est. Del. Date	-
Version	1.2
Date	21.10.2019
Status	As run
Lead Author	Andreas Pahler, apahler@irs.uni-stuttgart.de, USTUTT
Approved by	

VERSION HISTORY

Version #	Implemented By	Revision Date	Approved By	Approval Date	Explanation
1.00	Andreas Pahler	27/03/2019			First version of procedure
1.01	Andreas Pahler	12/04/2019			Layout changes
1.1	Andreas Pahler	01/07/2019			Changed to as-run version
1.2	Andreas Pahler	21/10/2019			Converted to report

TABLE OF CONTENTS

LIST OF ABBREVIATIONS AND DEFINITIONS

Abbreviation	Definition
TV	Thermal Vacuum
ESBO *DS*	European Stratospheric Balloon Observatory *Design Study*
STUDIO	Stratospheric Ultraviolet Demonstrator of an Imaging Observatory
FFT	Full Functional Test
RFT	Reduced Functional Test

REFERENCE DOCUMENTS

[RD1]	pco.edge 4.2 data sheet v1.03A, PCO AG, Germany
[RD2]	pco.edge family User Manual v2.24, PCO AG, Germany, 2017
[RD3]	ECSS-E-ST-10-03C, Space Engineering – Testing, 1 June 2012
[RD4]	https://www.edmundoptics.com/resources/application-notes/testing-and-detection/choosing-the-correct-test-target/
[RD5]	EMVA Standard 1288 – Standard for Characterization of Image Sensors and Cameras, Release 3.1, 30. December 2016

1 SCOPE

This document documents the tests conducted of a pco.edge 4.2 camera (Camera Link version) in a thermal vacuum chamber at the Institute of Space Systems (IRS) of the University of Stuttgart. The objective of this test was to evaluate the suitability of said camera for conditions in the stratosphere. The camera was provided by PCO AG in Kehlheim, Germany.

These tests are part of the ESBO *DS* project at the University of Stuttgart. ESBO *DS* (European Stratospheric Balloon Observatory *Design Study*). ESBO *DS* is a project conducted by several European partners to evaluate possibilities to observe astronomical targets from a balloon in the stratosphere. The main scientific instrument will observe targets in the ultraviolet regime of the spectrum. In order to mitigate disturbances, an active image stabilisation system will take pictures through a camera in the visible regime of the spectrum. The movement of star images from picture to picture will be evaluated and used to move a fast tip/tilt mirror. The purpose of this test is to evaluate the suitability of the pco.edge 4.2 camera for use within the image stabilization system for STUDIO (Stratospheric Ultraviolet Demonstrator of an Imaging Observatory).

The objective of this test series is to evaluate the suitability of the pco.edge 4.2 camera to operate under stratospheric conditions. This includes near-vacuum conditions as well as low temperatures. The operating temperature of the camera as stated in [RD1] is +10 °C to +40 °C under standard conditions. However, the camera was tested for an operational temperature range down to -30 °C – 34 °C at a pressure of 3 mbar. The lower limit might seem optimistic since temperatures during ascent of the STUDIO flight might reach as low as -60 °C. On the other hand, the coldest temperature layers are passed in a rather short period of time during ascent and operability of the camera is not required during this part of the flight. Also, heat exchange is limited due to lower atmospheric pressure at those altitudes and it is possible to add heaters in order to keep the camera cosy and warm. Therefore, a temperature range of -30 – 40 °C should be enough.

2 OVERVIEW

2.1 TEST SETUP

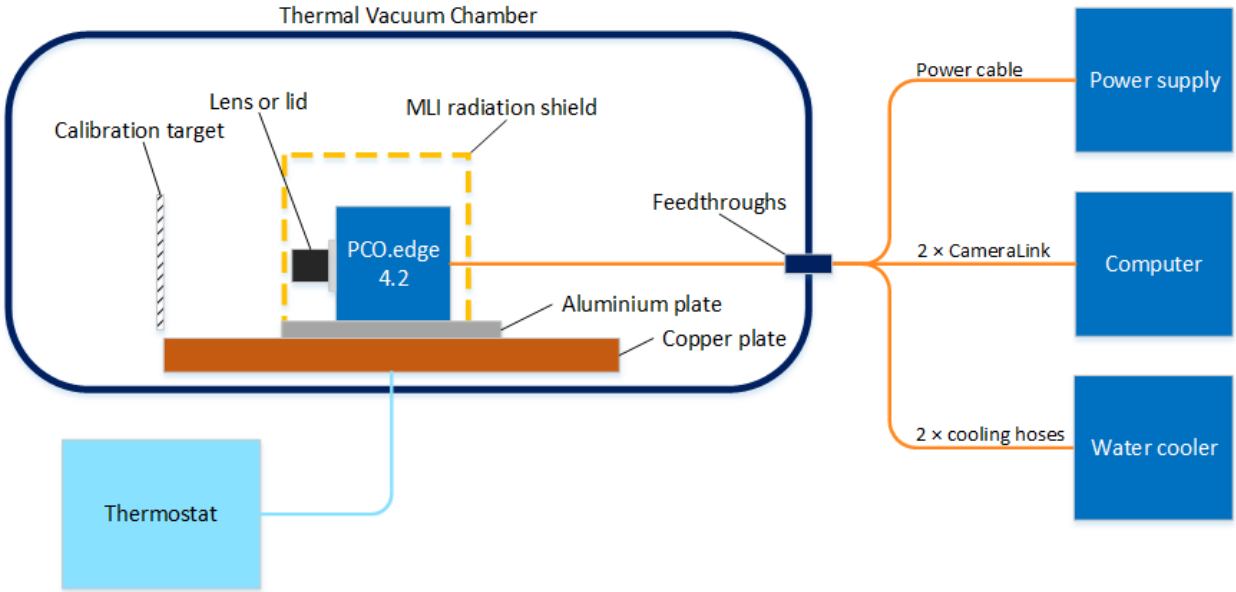

Figure 1: Sketch of the test setup in the thermal vacuum chamber

As sketched in Figure 1, the pco.edge 4.2 camera was located inside the thermal vacuum chamber on a copper plate, the temperature of which can be controlled by a thermostat. In order to match the bolt pattern of the copper plate, an aluminium adapter plate was located between the camera and the copper plate. The camera was connected to the outside world through a power cable, two camera link cables and two cooling hoses. During cycle 1 and 2, the camera was facing a USAF-1951 calibration target in order to judge if the camera was still able to take useful pictures. A selection of different targets can be found in [RD4].

During the following cycles dark frames were taken. For the dark frames, the lens was removed and the camera was closed with a lid.

The camera was mounted on the copper heating/cooling plate using an adapter plate made from the aluminium alloy AlMg4,5Mn. The plate had a thickness of 8 mm. It was mounted in the centre of the copper plate using M6 screws around the outer edge of the adapter plate and around the camera. All M6 screws were fixed with a torque of 4.5 Nm.

For the low temperature tests, the camera was shielded from thermal radiation from the thermal vacuum chamber's walls using a radiation shield made from multilayer insulation (MLI).

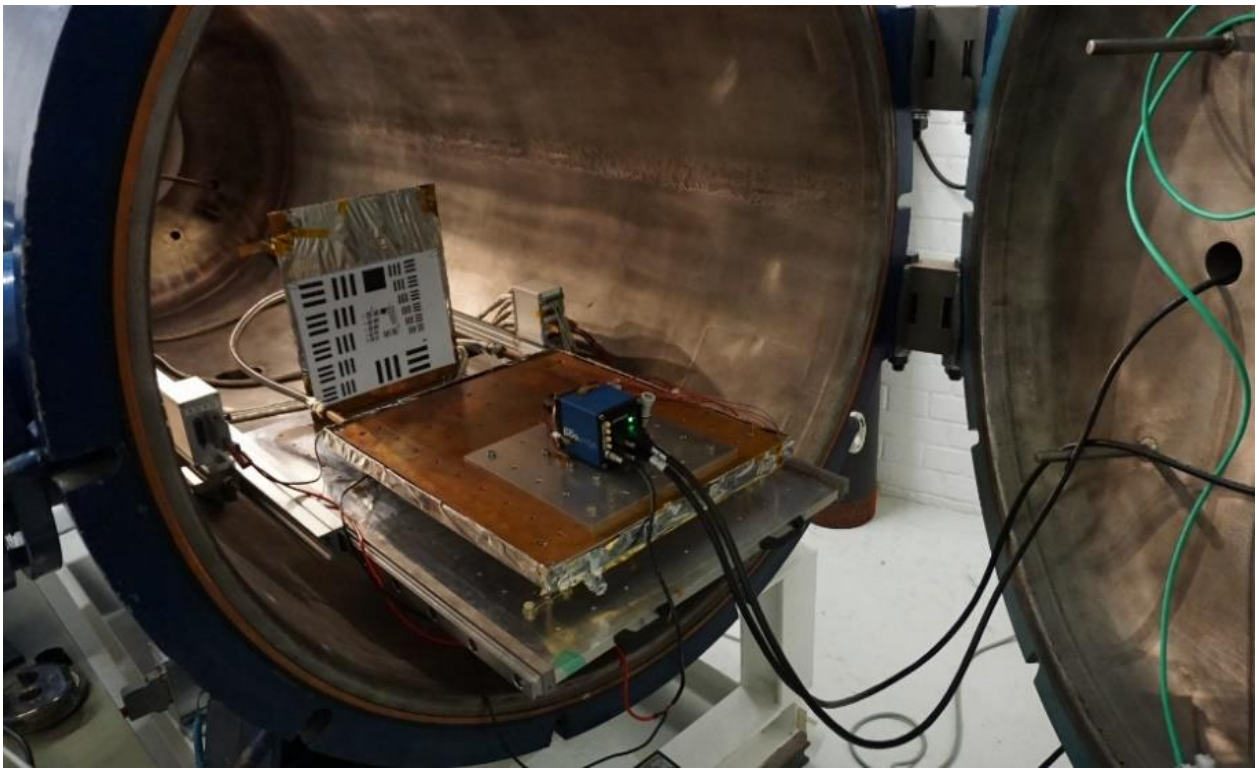

Figure 2: Test setup of the camera in the thermal vacuum chamber

2.1.1 Sensors

Several temperature sensors were used to record temperatures of the camera and the copper plate throughout the tests. Sensor 3 is integrated in the copper plate and measures the temperature inside of the plate. This sensor is also used by the thermostat to control the temperature of the copper plate. Sensor 9 was mounted on top of the aluminium adapter plate and thus measured the interface temperature between the camera and its surroundings. Until end of cycle 4, there were three temperature sensors mounted on the camera (sensors 10, 12, and 13). Since the camera had to be removed from the chamber between cycle 4 and 5, the sensors were removed from the camera. Figure 3 and Figure 4 show the positions of the sensors.

For cycle 5, care was taken to place the sensors as close as possible to their previous position. Additionally, a fourth sensor was added on top of the camera to better measure temperature distribution over the camera (sensor 14). This sensor is not visible in the figures, however the number 14 has been added at the place where the sensor was located.

Pressure was measured using a digital pressure sensor. It was not possible to read out this sensor automatically, so handwritten notes of the pressure readings were taken.

The PCO.edge 4.2 camera provides three internal temperature readings: one of the camera electronics, one of the sensor and one of the camera's internal power supply. These temperatures were also recorded in handwritten notes and added to the tables below.

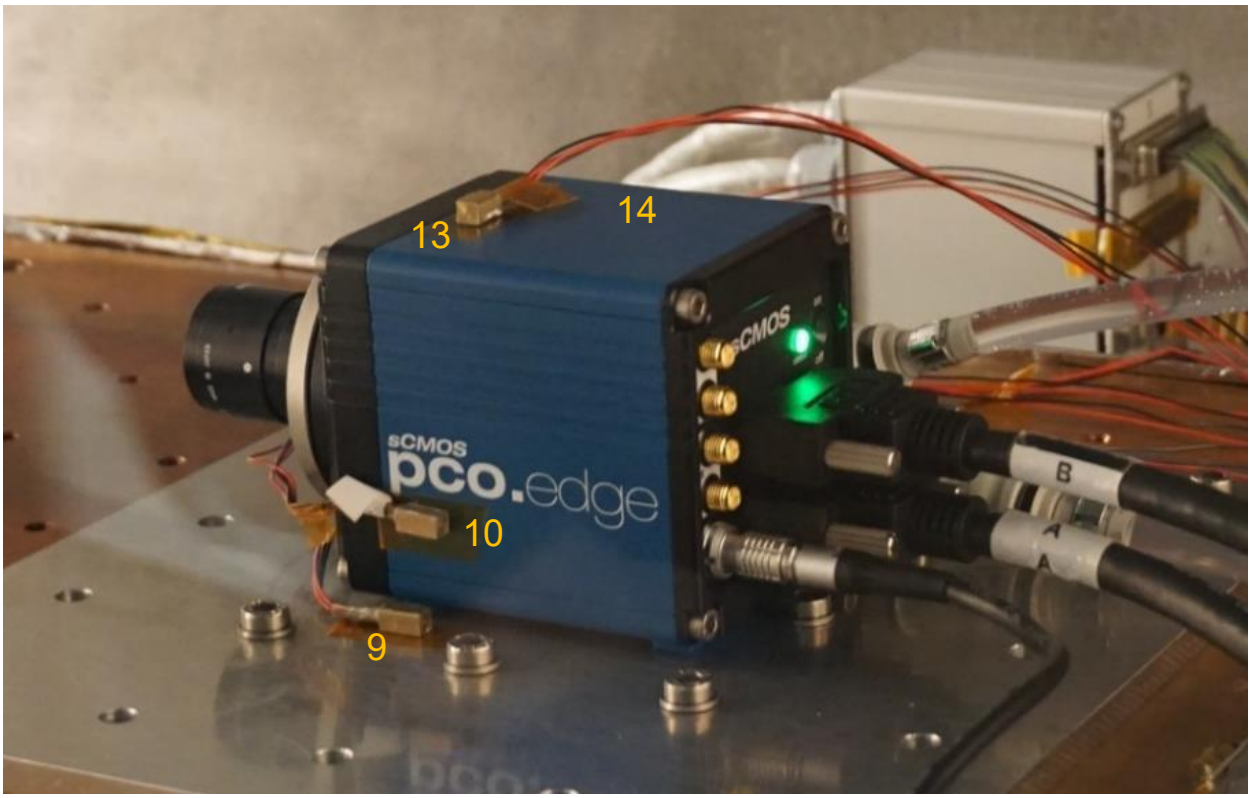

Figure 3: Location of sensors on the camera and the copper plate. Sensor 14 was added before cycle 5 and is not visible in this picture

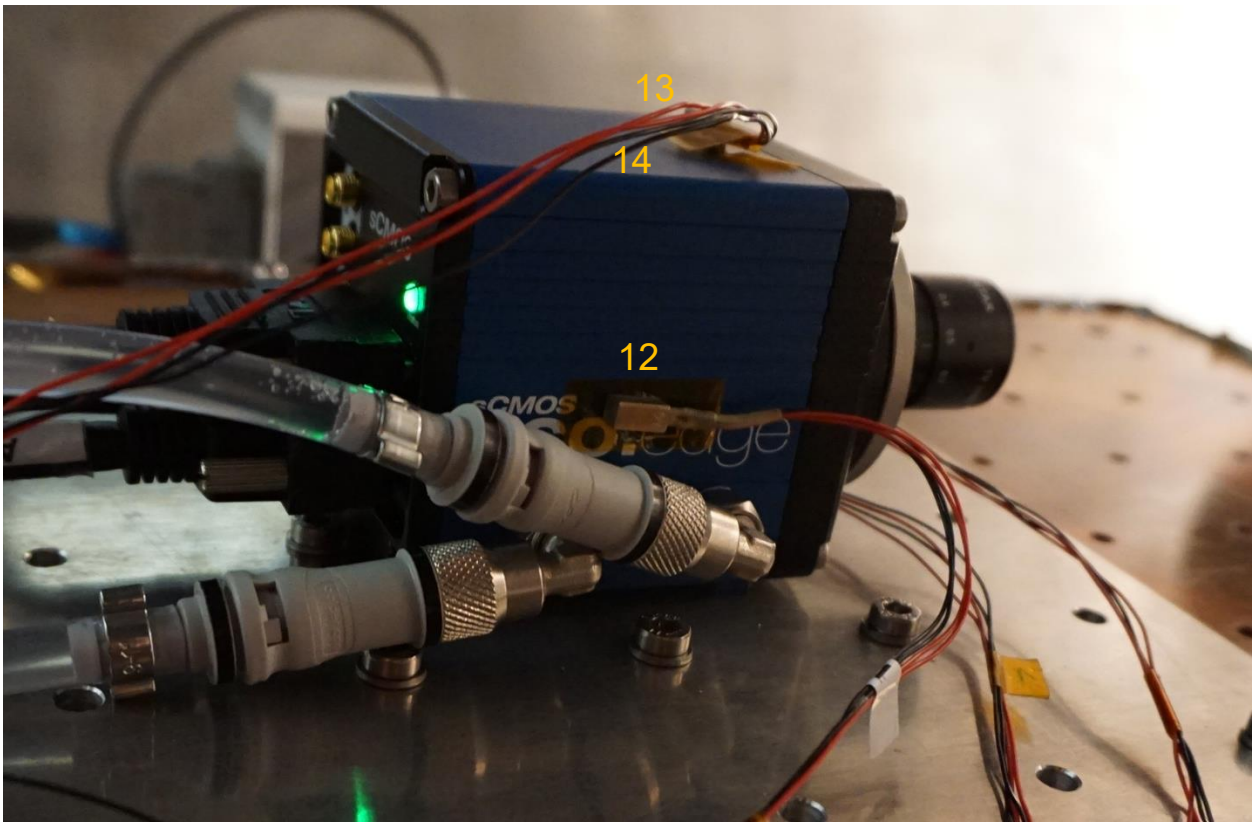

Figure 4: Location of sensors on the camera. Sensor 14 was added before cycle 5 and is not visible in this picture

2.2 TEST PROCEDURE OVERVIEW

Thermal ambient tests were conducted according to table 5-6 no. 11 of ECSS-E-ST-10-03C [RD3]. The protoflight approach was used.

The main difference between the two qualification approaches is that in protoflight testing, four ambient pressure cycles are conducted, while qualification testing requires eight ambient pressure cycles. However, since for the STUDIO flight, there will be only one pressure cycle, four ambient pressure cycles were deemed sufficient to build reasonable confidence in the camera's ability to survive the STUDIO flight. Therefore, in order to keep test effort and cost reasonable, the protoflight approach was used for the test of the PCO.edge 4.2.

The following cycles were conducted with the camera. A detailed description can be found in section 3.

Cycle 1: Operability at low pressure

Leak Test: Pressure cycle to evaluate the leakage rate of the test setup

Cycle 2: Confirmation of operating temperatures

Cycle 3: Extension of operational temperatures

Cycle 4: Pressure cycle, no thermal tests due to failure of the thermostat

Cycle 5: Extension of operational temperatures to the limits of the thermal vacuum chamber

2.2.1 Full Functional Test

As suggested by [RD3], a Full Functional Test (FFT) was performed every time a new environmental condition is applied to the camera for the first time. At the beginning of a FFT a power on test was conducted to demonstrate that the camera is able to power on from a cold (i.e. non-operational) state under the respective conditions. Furthermore, a set of images of a test target or dark frames were taken to determine if the camera electronics operate correctly. The temperature of the Peltier-cooled sCMOS sensor was monitored throughout the test.

The FFT was considered successful if the camera could power on under the respective environmental conditions while the temperature of the SCMOS was kept stable by the Peltier element, and if the pictures taken did not show any sign of an electronics malfunction.

2.2.2 Reduced Functional Test

If successful operation of the camera at certain environmental conditions had already been demonstrated earlier in the test, a Reduced Functional Test (RFT) was conducted. During an RFT, pictures were taken at 80 FPS.

The RFT was considered successful if the camera was able to take accurate pictures at 80 FPS and the temperature of the sCMOS sensor did not indicate a leak of the cameras internal pressure housing around the sensor.

2.3 SUCCES CRITERIA

The test series was considered successful if the camera was operational at 3 mbar pressure and the boundaries of the operating temperature range at this pressure are determined. Operation at lower temperatures than the operational temperatures given by the manufacturer in [RD1] was of secondary importance, since heating and cooling of the camera will be possible during flight.

For success criteria on FFT and RFT, see the respective sections above.

3 DETAILED TEST PROCEDURE

3.1 GENERAL CONDITIONS

Conditions given by ECSS [RD3] are as follows:

- Temperature rate of change shall be lower than 20 °C per minute
- Temperature tolerances according to table 4-1 of ECSS-E-ST-10-03C are +0/-4 K for the lower temperature limit and -0/+4 K for the higher temperature limit
- Temperature changes shall be followed by a ~2 h dwell time ("hot/cold soak"). This is not necessary if the temperature change is followed by a pressure increase to ambient atmospheric pressure without FFT or RFT and if the camera is not significantly colder than ambient temperature (i.e. if there is no risk for condensation)
- Pressure tolerances shall be +5/-10 % of the intended pressure for the particular step
- A functional test shall be conducted after every pressure change
- A functional test shall be conducted after every hot or cold soak
- Full Functional Tests shall include a power on test (see also 2.2.1 Full Functional Test)

If testing had to be interrupted overnight, the pressure chamber was left evacuated. This lead to extension of the respective cycle overnight with the pressure increase and the following functional test at the next day.

Limitations imposed by technical equipment caused deviations from the requirement on temperature rate of change. The temperature rate of change was occasionally exceeded. However, this is not considered critical, since a faster change in temperature imposes higher stresses on the equipment and the camera still worked afterwards.

3.2 CYCLE 1

Conducted 03. May 2019.
The purpose of this cycle was to determine if the camera can be operated at low pressures.
The main steps are:

- Functional check at ambient conditions
- Stepwise decrease of pressure to 3 mbar to confirm operability of the camera at the particular pressure levels
- Full Functional Test at every pressure level
- At 3 mbar: Test of equilibrium temperature **with** activated water cooling. This shall be done by conducting a Full Functional Test until the camera has reached thermal equilibrium
- At 3 mbar: Test of equilibrium temperature **without** activated water cooling. This shall be done by conducting a Full Functional Test until the camera has reached thermal equilibrium
- Increase of pressure to ambient atmospheric pressure

The feedthrough for the camera link cables was discovered to be not tight, which allowed for air to leak into the chamber. After reaching the pressure level of 500 mbar, the pressure was increased to ambient pressure in an attempt to fix the leak. Unfortunately, it was still not possible to reach pressures below 10 mbar.

During the FFTs in this pressure cycle, pictures of a test target were taken.

Towards the end of the test a leak was discovered in the cooling liquid circuit at the camera. After increasing the pressure to ambient temperatures, the leak was located at the camera side of the cooling hose on one of the connectors. Apparently the vacuum lead to a leak of cooling liquid between connector and hose. To prevent further leaks, the liquid cooling system was removed from the vacuum chamber and further cycles were conducted without liquid cooling.

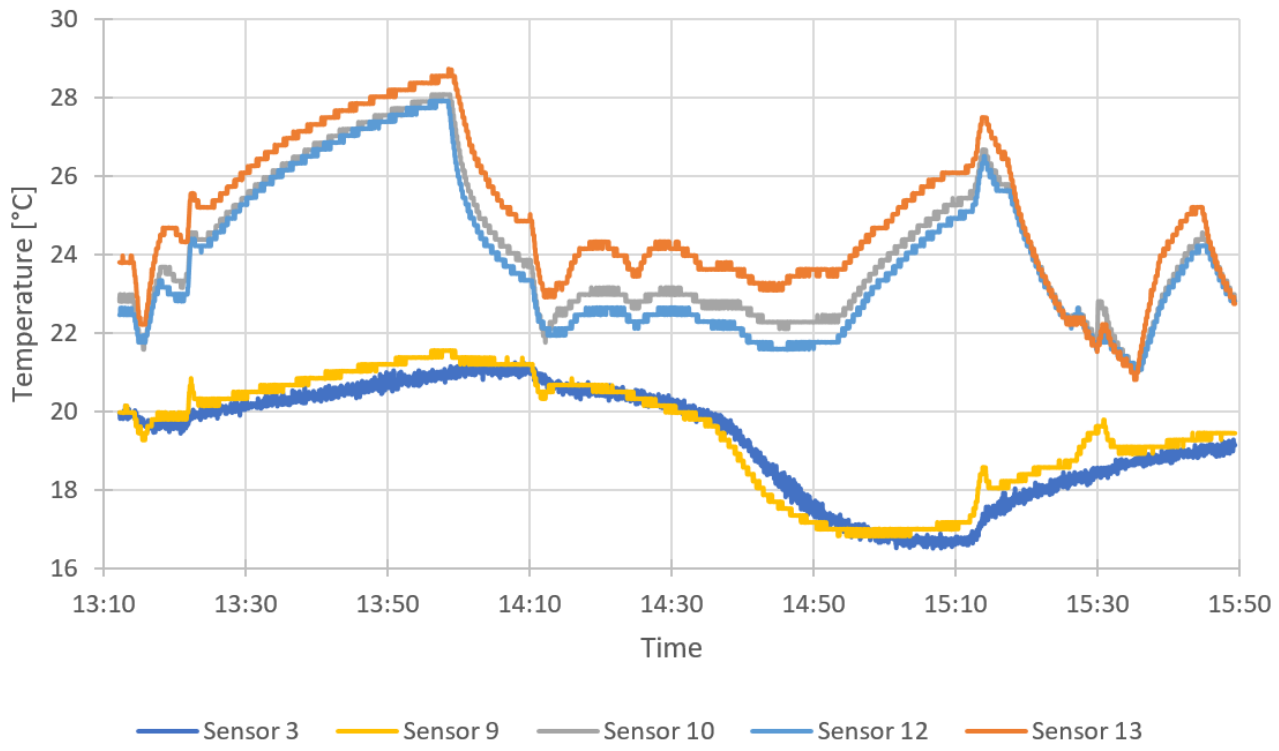

Figure 5: Temperature profiles of external temperature sensors during cycle 1

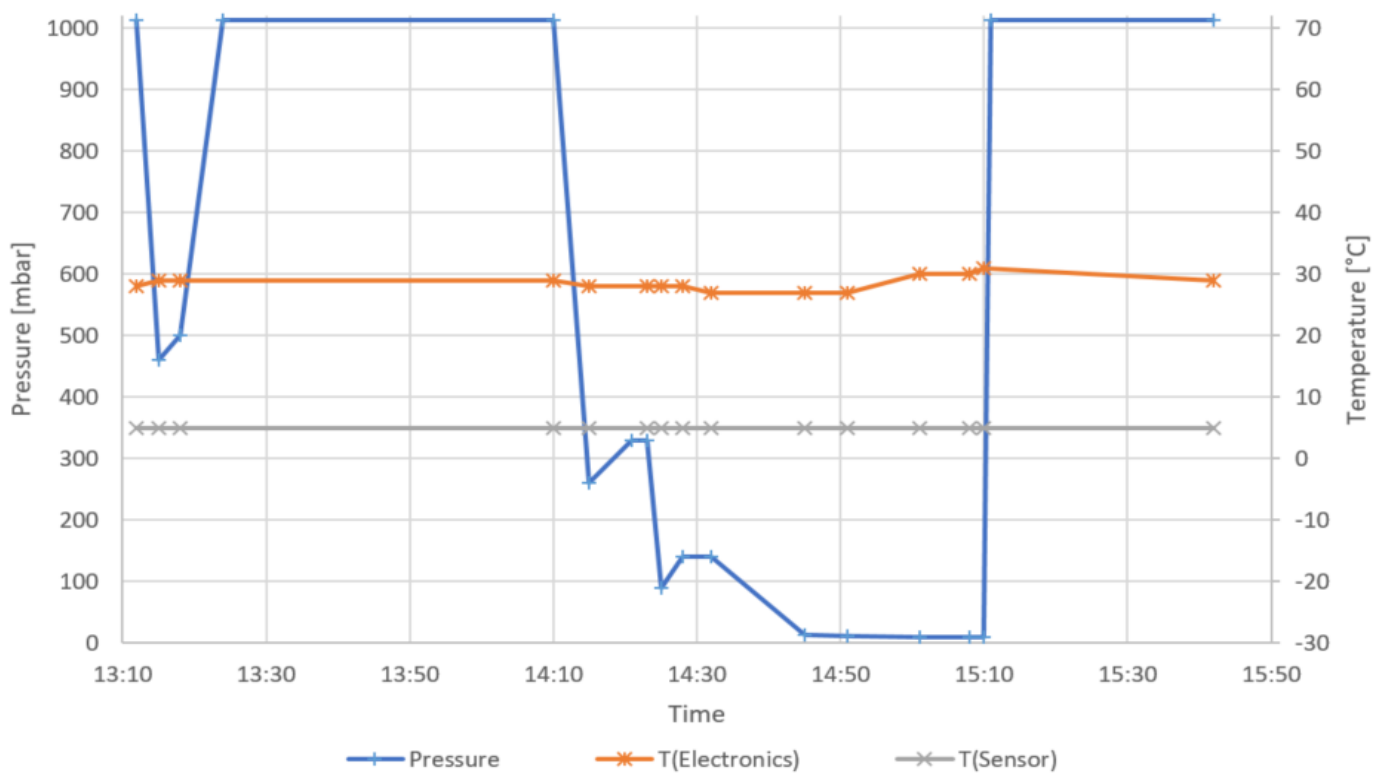

Figure 6: Pressure profile and internal temperatures during cycle 1

3.3 LEAK TEST

Conducted 06. May 2019. Pressure was decreased to 3 mbar while the camera was installed inside of the vacuum chamber. However, the camera was not powered on. Main purpose of this test was to test the leakage rate through the improved camera link feedthrough. At the same time this was a passive pressure cycle for the camera.

The steps during this test were:

- 9:40 vacuum pump on, pressure decrease
- 10:00 3.0 mbar, vacuum pump off
- 10:05 5.2 mbar
- 11:03 48 mbar
- 11:05 pressure increase, end of test

3.4 CYCLE 2

Conducted 06. May 2019.
This cycle shall confirm the operational temperatures of the camera and possibly extend the lower operational temperature limit.
Unfortunately, the LabView measurement equipment did not take any temperature values during this cycle.

The main steps were:

- Decrease of pressure to 3 mbar
- Decrease of temperature to -15 °C interface temperature
- Increase of temperature to ambient temperature
- Slow pressure increase during the night (not shown in the table and the graph below)

This cycle was conducted without liquid cooling of the camera. The camera was only cooled through conductive cooling to the copper plate.

During the FFTs in this pressure cycle, pictures of a test target were taken.

The air leak through the camera link feedthrough was improved, allowing for a pressure reduction to below 3 mbar as long as the vacuum pump was running. At the end of the test the camera was left in the evacuated vacuum chamber. The leak in the camera link feedthrough lead to a slow pressure increase over the following night.

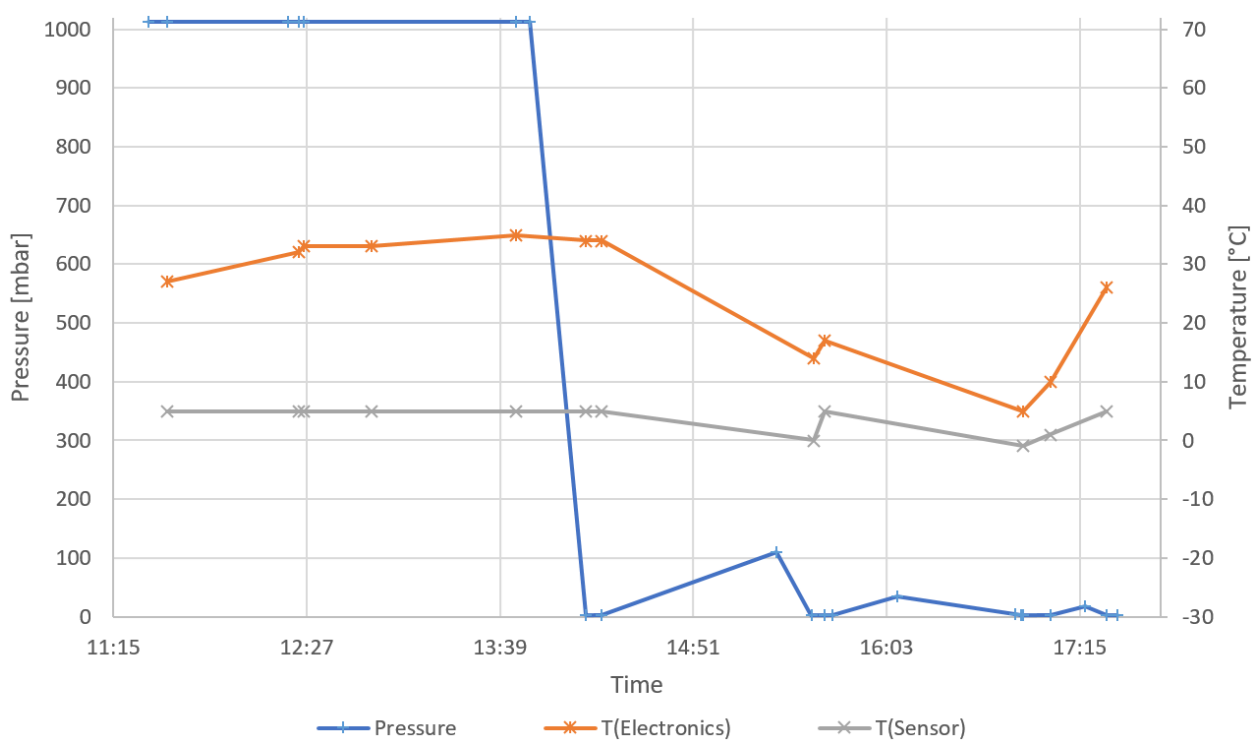

Figure 7: Pressure profile and internal temperatures during cycle 2

3.5 CYCLE 3

Conducted 08. May 2019.
This cycle shall confirm the operational temperature determined during cycle 2 and possibly further extend the operating temperature range.
Temperature testing during this cycle shall be started at the lowest temperature at which the camera was still operational in cycle 2.

The main steps are:

- Decrease of pressure to 3 mbar
- Stepwise decrease to -17.8 °C interface temperature
- Temperature increase to avoid condensation
- Increase of pressure to ambient conditions

The lens was removed from the camera prior to this cycle. The lens thread of the camera was covered by a lid. During the FFTs in this pressure cycle, dark frames were taken.

The figures on the following page show the temperature and pressure profiles during the test. The pressure increase between approximately 14:15 and 15:30 was caused by the vacuum pump being turned off during this time.

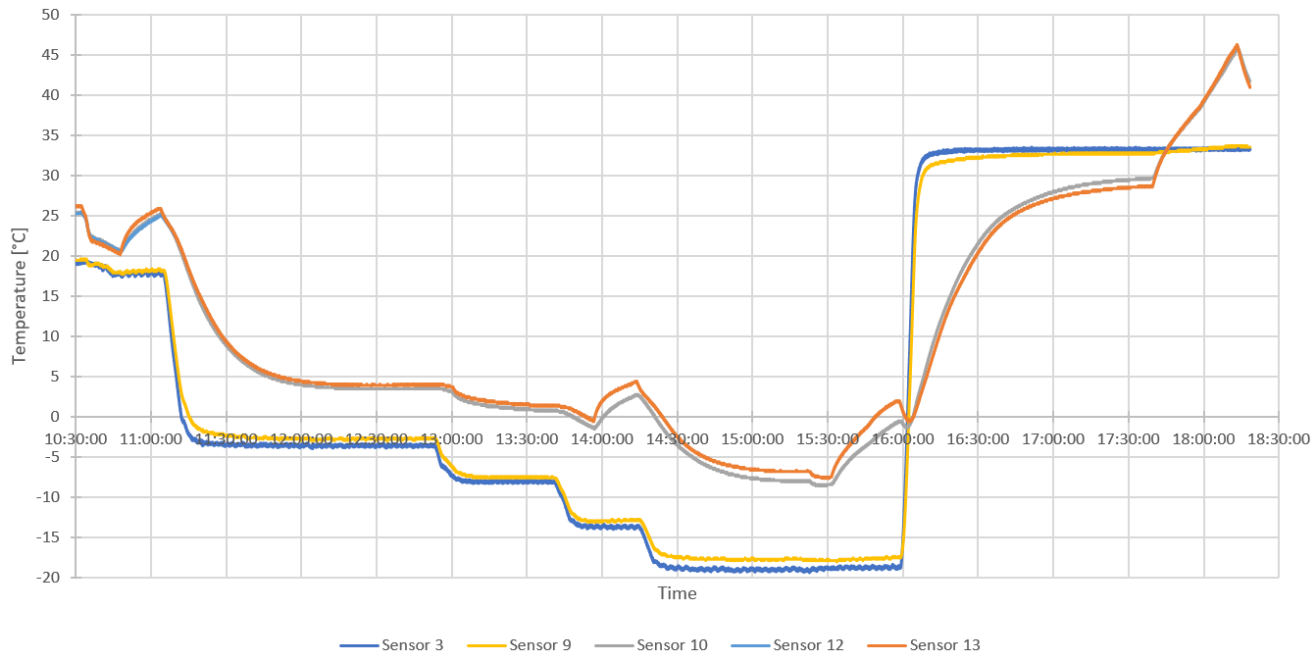

Figure 8: Temperature profiles of external temperature sensors during cycle 3

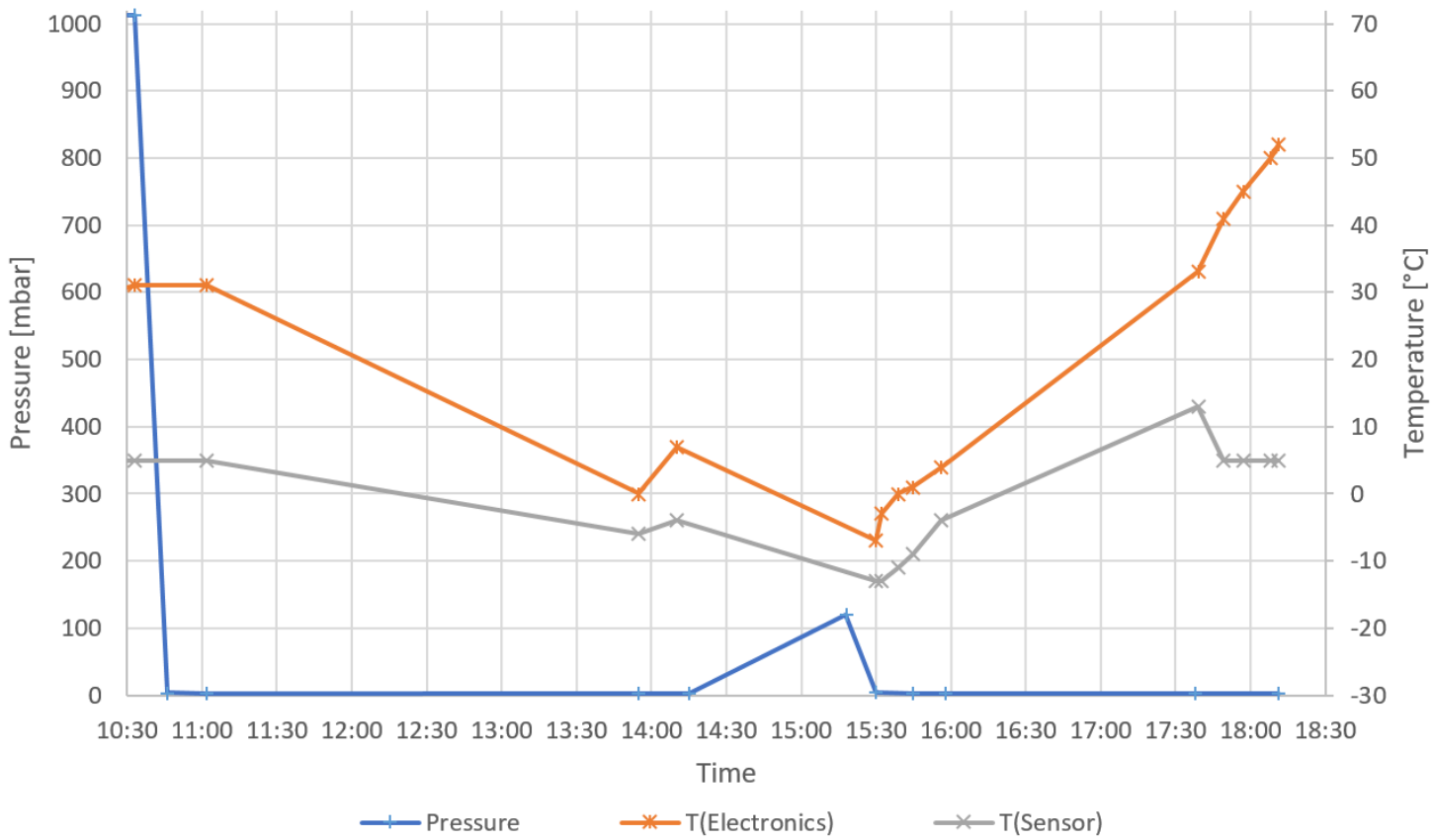

Figure 9: Pressure profile and internal temperatures during cycle 3

3.6 CYCLE 4

Conducted 09. May 2019.
During this cycle, the pressure was reduced to 3 mbar. Unfortunately, the thermostat which heats or cools the copper plate failed. The tests had to be aborted and the pressure was increased to ambient level again. However, a pressure of 3 mbar was maintained for more than five hours. Thus, this is a complete pressure cycle for the camera without any thermal testing.

During the FFT in this pressure cycle, dark frames were taken in vacuum.

3.7 CYCLE 5

Conducted from 17. June 2019 until 19. June 2019. Times during this cycle refer to beginning of the tests, which was 17. June 2019 12:00.
Another temperature sensor was added on top of the camera (sensor 14), the other sensors were placed in the same positions as before.
During this cycle, pressure and temperature cycling was conducted with the camera. The camera was exposed to near-vacuum conditions of under 3 mbar for more than 48 h.

The main steps were:

- Decrease of pressure to under 3 mbar
- Dwell time to eliminate temperature differences throughout the test setup. The vacuum pump was turned off during this time, leading to a slow pressure increase.
- Decrease of pressure to 3 mbar
- Thermostat set to +15 °C
- Long duration test, camera running in vacuum conditions during the night
- Increase of temperature to evaluate behaviour of camera at various higher temperature levels
- Decrease of temperature to cool down camera housing
- Long duration test, camera running through a second night
- Stepwise decrease of temperature down to the limit of the thermal vacuum chamber
- Increase of temperature to avoid condensation
- Increase of pressure to ambient atmospheric pressure

During the FFTs in this pressure cycle, dark frames were taken.

In order to shield the camera from thermal radiation originating from the vacuum chamber walls, a housing made of multilayer insulation (MLI) was installed around the camera prior to this test cycle. For the lowest temperature step, the thermostat was set to -33 °C which resulted in a camera temperature of approximately -30 °C.

The thermostat was not able to reach lower temperatures. Note the ripple in copper plate temperature in Figure 11 after approximately 47 h. The periodic increase and decrease in temperature with a notable amplitude indicated that the thermostat is at the edge of its capabilities. It should be noted that not the whole camera housing reached -30 °C during the 2 h dwell time. This might be because of some parts of the camera were hotter than others at the beginning of the dwell time, due to tests conducted during the previous temperature step. However, the reference temperature commonly used for testing is the temperature of the interface between test object and the surroundings. In this case, this is the aluminium plate, which was at -30 °C.

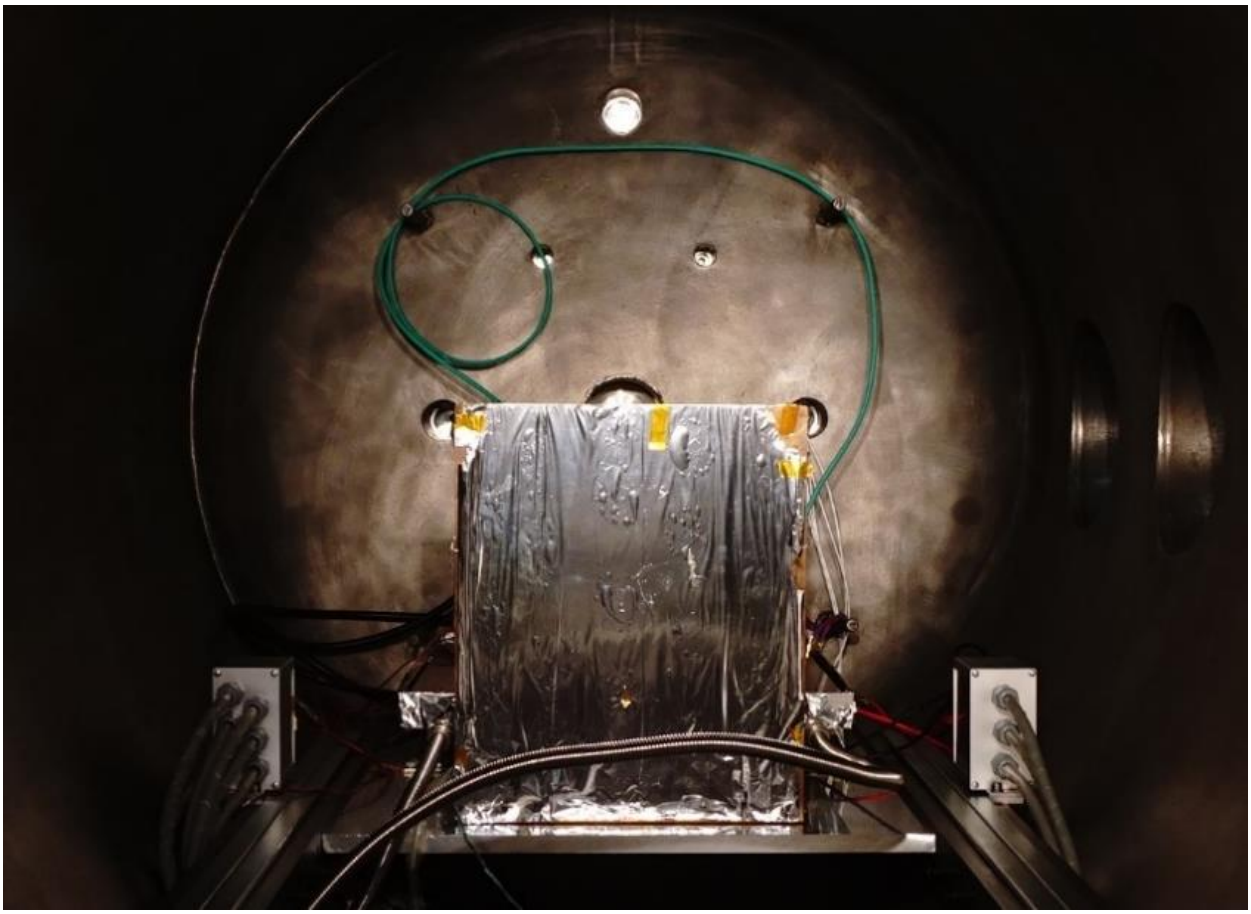

Figure 10: The MLI housing that covered the camera during cycle 5 photographed through the rear window of the thermal vacuum chamber

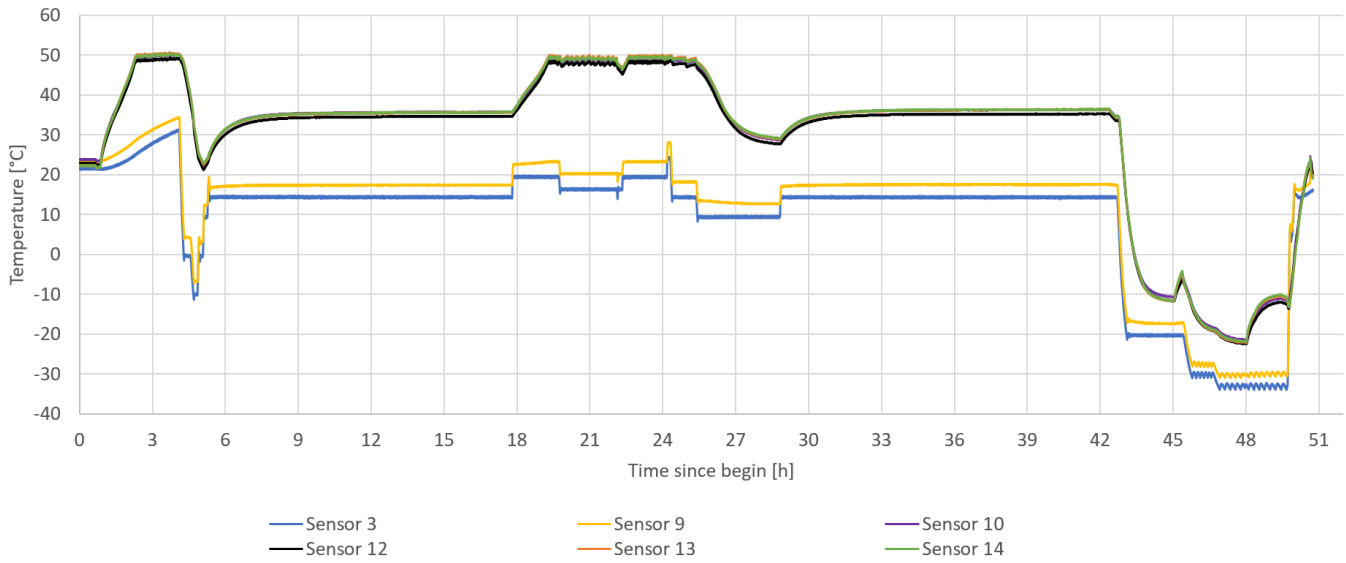

Figure 11: Temperature profiles of external temperature sensors during cycle 5

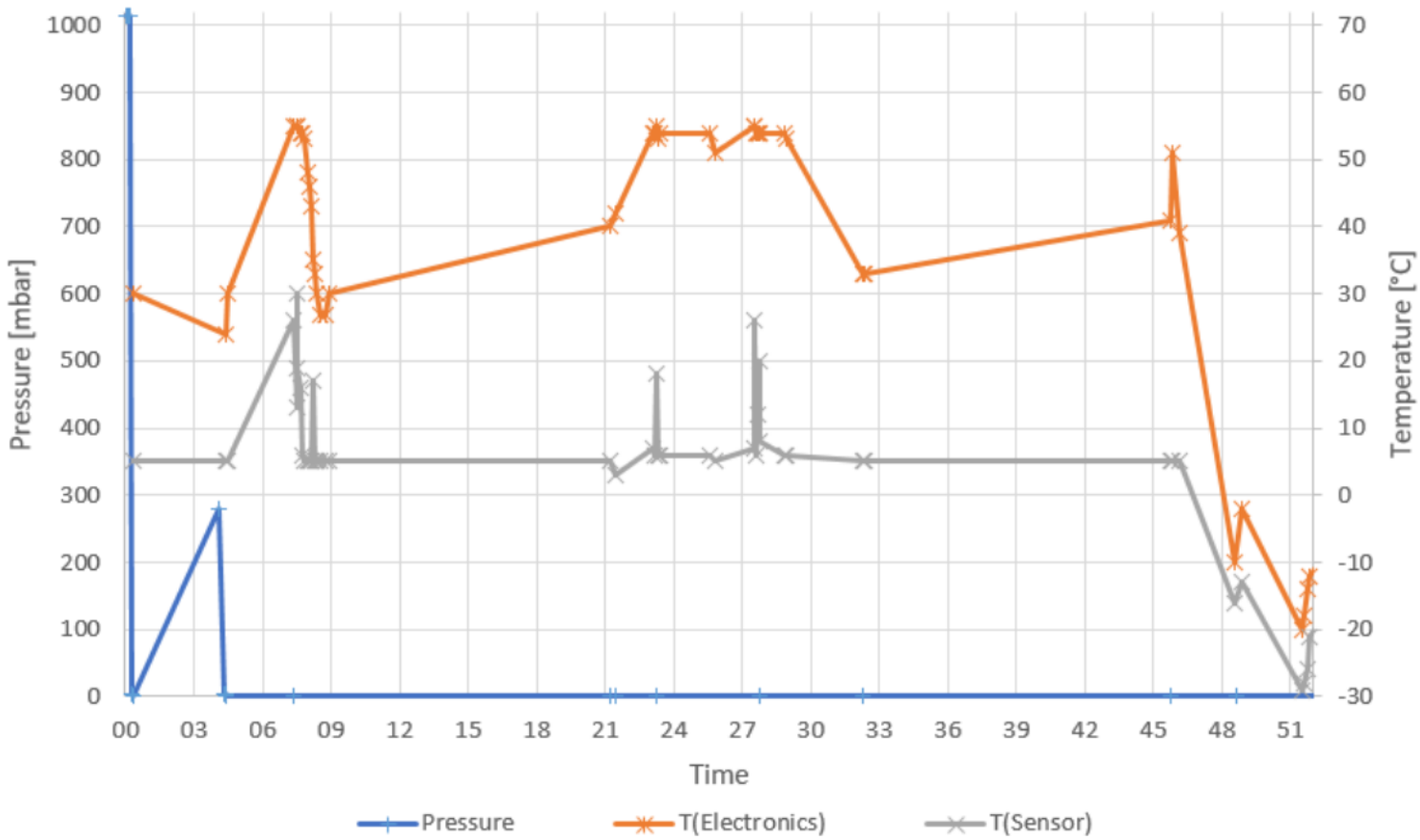

Figure 12: Pressure profile and internal temperatures during cycle 5

4 TABULARY SUMMARY OF TESTS

Date	Test cycle	Tests conducted
03. May 2019	Cycle 1	Stepwise pressure decrease to 10 mbar to confirm operability of the camera in vacuum, pictures of the test target were taken at different pressures
06. May 2019	Leak test	Pressure cycle (camera not operational) down to 3 mbar in order to fix a leak on a cable feedthrough, pictures of the test target were taken at +10 °C and 0 °C
06. May 2019	Cycle 2	Pressure cycle to 3 mbar and thermal test down to -15 °C, pictures of the test target were taken at different temperatures
08. May 2019	Cycle 3	Pressure cycle to 3 mbar and thermal test down to -17 °C and up to +33 °C, dark frames were taken at different temperatures
09. May 2019	Cycle 4	Pressure cycle to 3 mbar, thermal tests failed due to thermostat malfunction, dark frames were taken at near-vacuum conditions
17. – 19. June 2019	Cycle 5	Pressure cycle to 3 mbar, camera at 3 mbar for 48 h, thermal test down to -30 °C, determination of upper temperature limit without water cooling, dark frames were taken at different temperatures

5 RESULTS

The tests conducted in the thermal vacuum chamber at the Institute of Space Systems yielded that the PCO.edge 4.2 is able to opwerate under near-vacuum conditions at 3 mbar. The camera was exposed to five pressure cycles to 3 mbar and one pressure cycle to 10 mbar. The ECSS standard for testing [RD3] asks for only four cycles for the protoflight approach.

The camera was able to turn on from a power off state at a temperature of -30 °C. It was also able to take pictures at this temperature. Self-heating of the camera increased the internal temperatures significantly at low temperatures. At interface temperatures above 17 °C, the conductive cooling to the copper plate was not enough to keep the temperature of the camera electronics below 50 °C.

At 50 °C, the camera electronics shuts of the peltier cooling element. This decreases power dissipation in the camera and prevents the camera from heating up further. Once the camera temperature drops below 50 °C, the peltier element is turned on again. This behavior was observed during the test and prevented the camera from taking any damage at high interface temperatures, however the temperature of the sCMOS sensor rose over 5 °C and thus was unstable over time.

Note that this occurred while the camera was not cooled by the liquid cooling circuit. Liquid cooling is able to keep the internal camera temperatures well below 50 °C. In case the interface temperature during flight is expected to be higher than 17 °C, liquid cooling of the camera will be necessary. Thermal simulations will show if this is the case.

The connectors of the liquid cooling circuit were found to leak in vacuum. Therefore, in case a liquid cooling circuit is installed in the gondola during flight, special attention shall be paid to the tightness of all connectors.

5.1 IMAGE QUALITY

Dark frames were taken at different pressures and temperatures. For the different temperatures and pressures, dark frames were taken at exposure times from 1 s to 10 s in steps of 1 s. According to the EMVA Standard 1288 [RD5], pixel values were averaged over 10 images. Then, the mean pixel value over the whole resulting image was calculated and converted to electrons per pixel using the A/D conversion factor of 0.46 e^-/count from the PCO.edge 4.2 data sheet [RD1].

Figure 13 shows the graph of mean dark signal over exposure time. The dark signal was plotted for six exposure times, as proposed in [RD5]. The orange measurements were taken prior to the vacuum tests at ambient pressure and temperature, while the sCMOS sensor was cooled to 5 °C by the peltier cooler. The dashed orange line is the line of best fit through the six exposure times. The slope of this line is the dark current, while the y intercept equals bias current plus readout noise. The slope of 0.4518 e^-/pixel/s is in accordance with the value of < 0.5 e^-/pixel/s given in [RD1].

The dashed yellow line is the line of best fit through different exposure times at ambient temperature with the sCMOS sensor cooled to 5 °C, but at a pressure of 3 mbar. Note that slope and y intercept are almost exactly identical with the values at ambient pressure. Small differences can be explained by measurement inaccuracies and random noise, as well as the temperature of the camera electronics not being controlled precisely. Therefore, it can be concluded that low pressure has no effect on the dark current.

The green and blue line show the dark signal of frames taken at -10 °C and -28 °C, respectively. Taking dark frames at -30 °C was not possible, because the internal power dissipation of the camera increased the sensor temperature very quickly to approximately 28 °C. Note that already at -10 °C, the dark current is basically zero, but bias current plus readout noise increase at lower temperatures. However, the effect is on the order of 10 e^-/pixel/s and therefore still acceptable. The negative slopes would indicate a small negative dark current, which is unphysical. This can be explained as follows: The camera was turned on from a cold state, with the whole camera being very cold. During the process of taking dark frames, the camera started to heat itself due to dissipation of electrical power. Therefore, the internal camera temperature started to rise, which lead to a decrease in bias current and/or readout noise. Since pictures were always taken with ascending exposure times, this leads to a slope that resembles a negative dark current, but is actually caused by increasing temperature of the camera electronics.

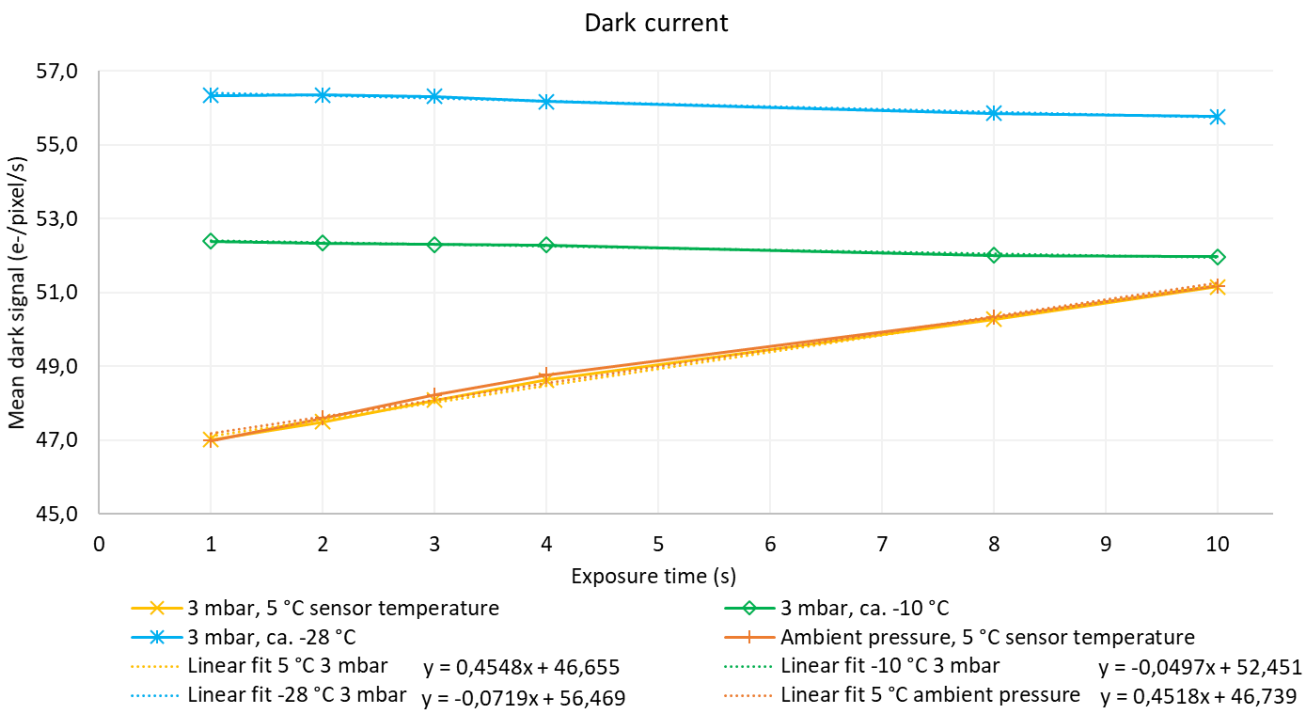

Figure 13: Dark current for different sensor temperatures and pressure

STU-IRS-M-PRO-1220-01-v1.0_TIP-Vibration-Test-Report_2021-07-15

TIP VIBRATION TEST REPORT

Version 1.0

15.07.2021

Status: Released

H2020 INFRADEV-01-2017 project "European Stratospheric Balloon Observatory *Design Study*"

Topic: INFRADEV-01-2017 Design Studies

Project Title: European Stratospheric Balloon Observatory *Design Study* – ESBO *DS*

Proposal No: 777516 – ESBO DS

Duration: Mar 1, 2018 - Feb 28, 2021

WP (EU)	WP 12
WBS Item (internal)	823
PBS Item(s)	1220
Title	TIP Vibration Test Report
Description	Report on vibration tests of Telescope Instruments Platform
Lead Beneficiary	"USTUTT"
Nature	"Report"
Dissemination Level	"Public"
Est. Del. Date	-
Version	1.0
Date	15.07.2021
Status	As run
Lead Author	Deniz Bulut, dbulut@irs.uni-stuttgart.de, Philipp Maier, pmaier@irs.uni-stuttgart.de
Approved by	

VERSION HISTORY

Version #	Implemented By	Revision Date	Approved By	Approval Date	Explanation
1.00	Philipp Maier	15/07/2021			Converted content to test report

TABLE OF CONTENTS

LIST OF ABBREVIATIONS AND DEFINITIONS

Abbreviation	Definition
ESBO *DS*	European Stratospheric Balloon Observatory *Design Study*
FEM	Finite Element Method
MP	Measurement Point
STUDIO	Stratospheric Ultraviolet Demonstrator of an Imaging Observatory
TIP	Telecope Instrument Platform
UV	Ultraviolet

REFERENCE DOCUMENTS

[RD1]	IABG, TN-TR50-5648 89 kN Vibration Test Facility – Facility Description
[RD2]	IABG, TP-TR50-12333 TEST PROTOCOL Vibration Test on TIP Optical Bench for STUDIO
[RD3]	Bulut, D., Development and execution of a shock test of the STUDIO balloon optics, July 2021.
[RD4]	ECSS-E-ST-10-03C, Space Engineering – Testing, 1 June 2012

1 SCOPE

This document provides a report on the vibration test of the STUDIO Telescope Instruments Platform (TIP) conducted at IABG mbH, Ottobrunn, Germany, in June 2021. It describes the test setup, the test results, and summarizes the conclusions.

1.1 TEST OBJECTIVE

The objective of the TIP Vibration Test was twofold:

1. Verify the structural integrity of the TIP at mechanical loads expected during the flight (launch and flight);
2. Verify that optical alignment is maintained within the required limits during launch.

The ECSS-E-ST-10-03C was used as a guideline for the preparation of the vibration test.

2 OVERVIEW

2.1 TEST MOTIVATION

It was decided that only vibration tests will be performed. Shock tests are not foreseen, as the gondola is not expected to undergo major shocks before landing.

The vibration tests aim to

- Test whether any settling or loosening of the screws on the bench occurs;
- Verify that no damage to any of the components or their mechanical mounts occurs under vibration;
- And verify the maintained alignment of the optics after vibrations.

Functional tests shall be performed of the visible camera, the tip tilt platform, and the filter wheel already installed on the TIP.

For these tests, considering the criticality of the flight hardware, the UV detector will be replaced by a mass dummy.

Possible vibrations are suspected to be caused during:

- **Transportation:** the payload will have to be transported from Stuttgart, Germany to Kiruna, Sweden where it will be launched on a transport truck, still to be defined.
- **Launch:** due to the gondola release from the crane at take-off
- **Ascent and during the mission**: acceleration up to 5 g can be expected during the ascent in addition to potential oscillations of the gondola.
- **Termination of flight and landing:** this would be caused by the parachute opening, descent and landing. This could reach 10 g in any direction.

However, the latter is considered not to be critical, since the alignment of the optics is not required anymore and is therefore not defining for the test loads.

2.2 TEST ITEM OVERVIEW

The test item is the TIP, with the following components installed:

- Mirror M4
- Mirror M5
- Mirror M6
- Mirror M7
- Visible camera (with a C-mount lens mounted for optical tests)
- Visible light filter wheel
- M3-tower
- Tip-Tilt platform with M3 (mass- and inertia-equivalent engineering mirror)
- Mass dummies for UV detector, UV filter wheel, and UV electronics
- Optical target installed on the TIP baseplate for optical tests.

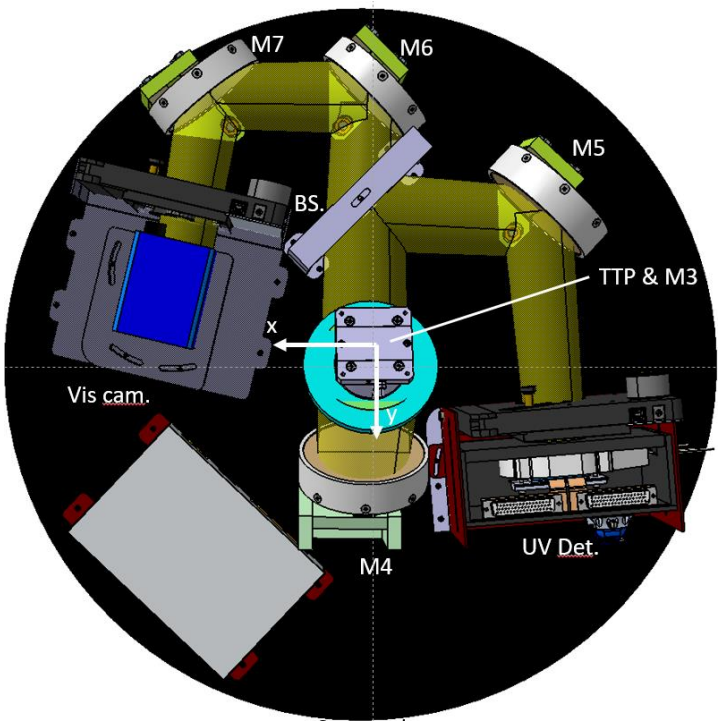

Figure 1: TIP and components

The TIP characteristics are given in the table below.

Table 1: Characteristics of the TIP

Material	CFRP sandwich with an Aluminium honeycomb core		
Diameter	650 mm		
Max. height	~ 280 mm		
Total mass	~ 36 kg		
Inertia Matrix /G [kg*m^2]	IoxG 0,367	IoyG 0,298	IozG 0,519
	IxyG -0,034	IxzG -0,004	IyzG -0,025
Principal Moment /G [kg*m^2]	M1 0,282	M2 0,381	M3 0,522

2.3 GENERAL TEST APPROACH

The general approach for the test is as follows:

1. Search for resonance frequencies at an amplitude of 0.2 g and a frequency sine sweep [5 Hz – 2000 Hz] in each axis before main test.
2. Main vibration test: sine sweep vibrations in 3 orthogonal axis X, Y, Z with an amplitude of 5 g and frequency sweep in the range 5 - 100 Hz.
3. Search for resonance frequencies at an amplitude of 0.2 g and a frequency sine sweep [5 Hz-2000 Hz] in each axis after main vibration test.
4. Functional tests of camera, tip/tilt platform and filter wheel before test campaign and after the test run for each axis.

Test Success Criteria:

- No visible damages
- No significant change in resonance frequencies before / after main vibration test
- No lateral image movement of target larger than 5 mm; no defocus to more than 200 µm.

3 TEST PERFORMANCE

3.1 TEST STAND

The test was performed at the IABG mbH space test center in Ottobrunn, Germany, on a shaker as specified in Table 2.

Table 2: Vibration test stand

Device	**Type**
Shaker	Tira TV 59389
Power Amplifier	Tira A540 3225
Control System Sydney	M&P VibRunner24
Measurement Amplifier	IAB MV100

3.2 INSTALLATION OF TEST ITEM

The assembled TIP is fixed to the shaker using a massive aluminum adapter plate and M8 cylinder head screws in all outer fixation inserts of the TIP (inner fixation ring not used) as shown in Figure 3. Axes for the shaker test are defined as indicated in Figure 2:

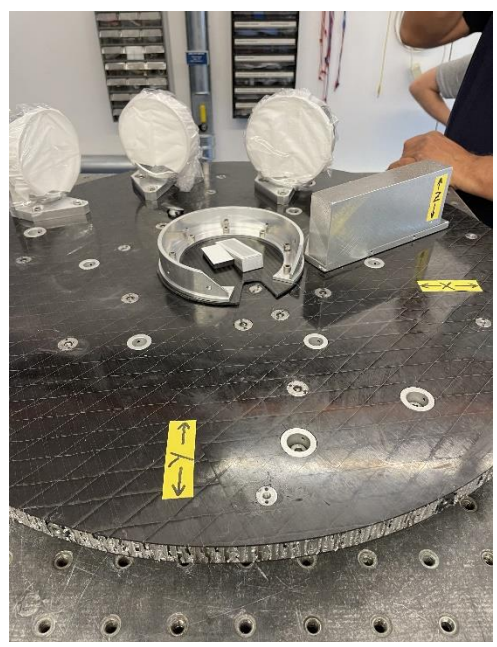

Figure 2: Axes definitions for the shaker tests

Figure 3: TIP mounted on shaker

For acceleration measurements, five acceleration sensors are installed on the TIP itself. Two more are installed on the shaker table for piloting of the shaker. The sensors are summarized in XXX.

Sensor no.	Component	Task	Location
P1	Shaker table	Control	-
P2	Shaker table	Control	-
MP1	M3 tower	Measurement	See Figure 4
MP2	UV dummy	Measurement	See Figure 3
MP3	PCO camera	Measurement	See Figure 4
MP4	Optical bench	Measurement	See Figure 3
MP5	Optical bench	Measurement	See Figure 6

For the y-axis runs, the test items was installed on the shaker in vertical position. For the x- and y-axis runs, the shaker was flipped into horizontal position and the test item installed on a sliding table.

Figure 4: Location of MP1

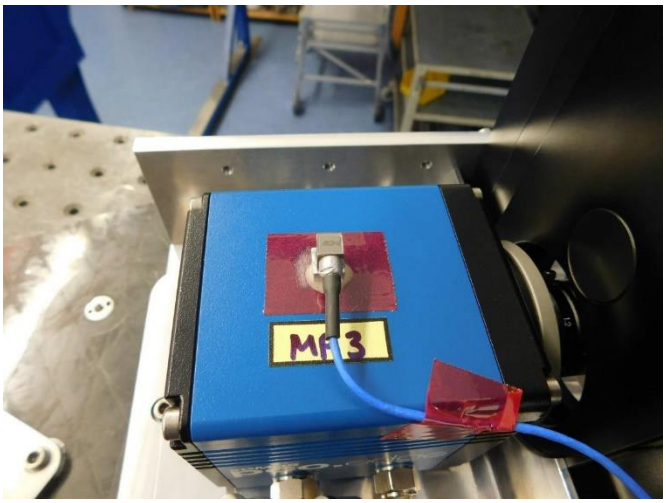

Figure 5: Location of MP3

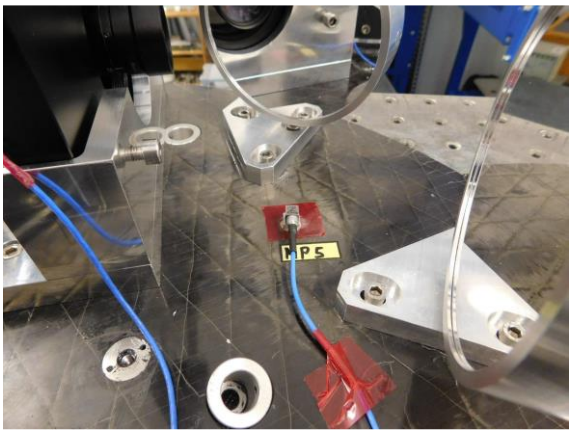

Figure 6: Location of MP5

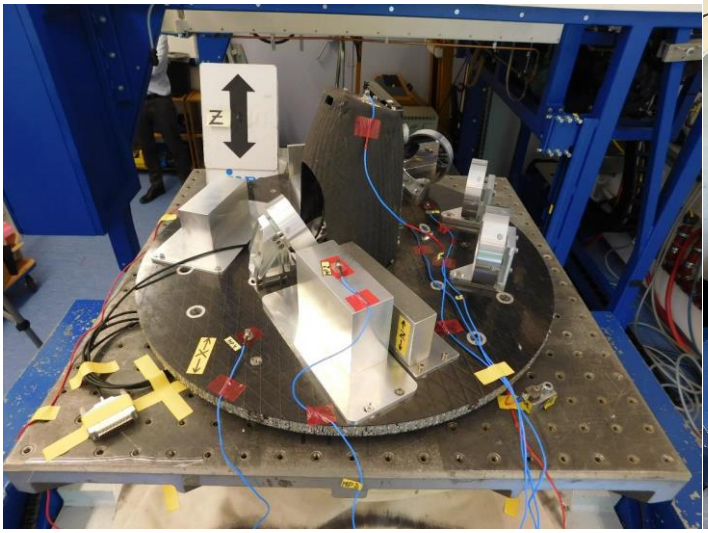

Figure 7: TIP on shaker head for z-axis test

Figure 8: TIP on sliding table

3.3 TEST SEQUENCE

Tests were conducted in the order as shown in Table 3. Piloting was based on the maximum of sensors P1 and P2 for all runs.

Table 3: Test sequence

Run no.	Description	Frequency range	Input level
Functional Test			
1z	Resonance search (Low Level Sine)	4 – 2000 Hz	0.2 g
2z	Sine Vibration (High Level Sine)	4 Hz 9.1 Hz 100 Hz	+/- 15 mm 5 g 5 g
3z	Resonance Search (Low Level Sine)	4 – 2000 Hz	0.2 g
Functional Test			
4x	Resonance search (Low Level Sine)	4 – 2000 Hz	0.2 g
5x	Sine Vibration (High Level Sine)	4 Hz 9.1 Hz	+/- 15 mm 5 g

		100 Hz	5 g
6x	Resonance Search (Low Level Sine)	4 – 2000 Hz	0.2 g
Functional Test			
7y	Resonance search (Low Level Sine)	4 – 2000 Hz	0.2 g
8y	Sine Vibration (High Level Sine)	4 Hz 9.1 Hz 100 Hz	+/- 15 mm 5 g 5 g
9y	Resonance Search (Low Level Sine)	4 – 2000 Hz	0.2 g
Functional Test			

Test levels below 9.1 Hz were lower than 5 g due to mechanical limitations of the shaker. For the interval from 4 to 9.1 Hz, the maximum allowable mechanical displacement of the shaker of +/- 15 mm was used.

3.4 FUNCTIONAL TESTS

The functional tests consisted of the following:

- Switch of filter wheel by one position
- Movement of tip/tilt platform to 5 different positions in both axes (0/0; 500/500; 1000/1000; 1500/1500; 2000/2000 µrad)
- Recording of an image series of 10 images @ 10 ms exposure time with visible light camera at the 5 abovementioned tip/tilt platform positions and at the tip/tilt platform powered off.

All images were taken of an optical target installed on the bottom of the M3 tower, as shown in Figure 9. The optical target consisted of

- An inclined “depth of focus” target scale and
- A plate with point targets

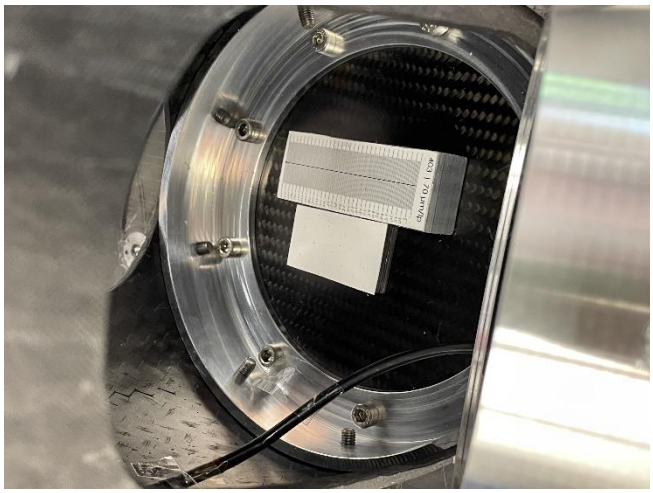

Figure 9: Optical target, with "depth of focus" scale (top) and point targets (bottom)

4 TEST RESULTS

For the complete plotted measurements see [RD2].

4.1 IDENTIFIED RESONANCE FREQUENCIES

Table 4: Resonance frequencies before/after high level tests for vibrations along x

Location	**Resonance Frequencies Before [Hz]**	**Accelerations Before [g]**
MP1	140; 335; 370	1.17; 0.75; 1.00
MP3	220; 255; 375; 1700	0.38; 0.97; 0.61; 0.34
MP4	Peaks below target value	target value: 0.20
MP5	Peaks below target value	target value: 0.20
Location	**Resonance Frequencies After [Hz]**	**Accelerations After [g]**
MP1	136.4; 329.2; 371.7	1.20; 0.82; 0.99
MP3	225; 243; 375; 1700	0.5; 1.26; 0.62
MP4	Peaks below target value	target value: 0.20
MP5	Peaks below target value	target value: 0.20

Table 5: Resonance frequencies before/after high level tests for vibrations along y

Location	**Resonance Frequencies Before [Hz]**	**Accelerations Before [g]**
MP1	230; 345	0.45; 1.53
MP3	Peaks too low, in tolerance	max. value 0,24
MP4	Peaks below target value	target value: 0.20
MP5	Peaks below target value	target value: 0.20
Location	**Resonance Frequencies After [Hz]**	**Accelerations After [g]**

MP1	220.5; 339.4	0.48; 1.42
MP3	Peaks too low, in tolerance	max. value: 0.22
MP4	Peaks below target value	target value: 0.20
MP5	Peaks below target value	target value: 0.20

Table 6: Resonance frequencies before/after high level tests for vibrations along z

Location	**Resonance Frequencies Before [Hz]**	**Accelerations Before [g]**
MP1	331.2; 374.8; 604.3	0.50; 0.43; 0.73
MP3	240.5; 314.9; 381.2; 1797.5; 1859	0.65; 0.57; 0.67; 0.80; 0.82
MP4	1031	0.38
MP5	220.5	0.67
Location	**Resonance Frequencies After [Hz]**	**Accelerations After [g]**
MP1	333.2; 374.8; 608	0.49; 0.41; 0.67
MP3	236.4; 311.4; 381.2; 1793; 1880.1	0.73; 0.57; 0.65; 0.93; 0.76
MP4	1031	0.38
MP5	220.5	0.71

4.2 MAXIMUM ACCELERATIONS DURING HIGH-LEVEL TESTS

Table 7: Maximum accelerations experienced at measurement points and associated excitation frequencies

Location	**Excitation x**		**Excitation y**		**Excitation z**	
MP1	11.66 g	100 Hz	10.56 g	94 Hz	5.42 g	100 Hz
MP2	5.33 g	100 Hz	5.87 g	100 Hz	5.23 g	100 Hz
MP3	5.39 g	100 Hz	9.80 g	94 Hz	6.07 g	100 Hz
MP4	5.20 g	100 Hz	5.04 g	100 Hz	5.14 g	100 Hz
MP5	5.19 g	100 Hz	6 g	93 Hz	6.20 g	100 Hz

4.3 CONCLUSIONS

No visible damage was observed. No major shifts in resonance frequencies were observed before/after the high level tests, indicating that components did not move significantly.

Shims on the mirror holders were observed to move and will need to be fastened with additional screws.

The first resonance frequencies of the M3 tower were observed to be rather low. Given that excitations are expected at 80 Hz from the tip/tilt platform during operation, the behavior of the tower should be observed closely, preferably with acceleration measurements during future

functional tests of the tip/tilt platform. Given the low amplitude of the expected excitation, this may not pose a problem, though.

Observed resonances at sensors MP4 and MP5 are surprising. Further FEM simulations of the test setup itself may provide explanations.

The results of the optical tests were not available yet at the time of writing of this report.

[SubTitle]

ESBO Solar Panel Thermal Vacuum Test

Document ID	Project
SCIPROJ-195065613-131	**ESBO**

Version:	Document Type:	Issue Date:	Valid From:
1.0	**Not defined**	**2021-05-31**	**2021-05-31**

	Name	Date
Prepared by:	Christian Lockowandt	2021-05-31
Reviewed by:		
Approved by:	Christian Lockowandt	2021-05-31

Distribution:

Swedish Space Corporation

Torggatan 15, SE-171 04 Solna, Sweden
Invoicing address: P.O. Box 4207, SE-171 04 Solna, Sweden
Phone: +46 8 627 62 00, Fax: +46 8 98 70 69
www.sscspace.com
Reg.no: 556166-5836
Registered Office: Kiruna

Change Record

Version	Date	Changed paragraphs	Remarks	Author
1.0	2021-05-31	All	First version	CLO

Table of Contents

1 INTRODUCTION

The main purpose with the tests reported in this test report is to test and identify solar panels that can withstand the environment on altitudes of 25-45 km concerning high temperatures and low pressure.

On stratospheric balloon flights solar panels with photovoltaic cells are used as a source of energy, specially for flight durations longer than 1-2 days. The generated electrical power can be used directly or for charging batteries. The environment on altitudes between 25-45 km that are the regular flight altitudes with stratospheric balloons is different from the ground level environment. There are mainly three differences that are important to consider in the design of solar panels for stratospheric balloons.

- Higher total irradiation from the sun.
- Lower thermal conductivity to the environment.
- Higher level of UV radiation.

The two first differences will result in a higher temperature on the solar panels than expected in a ground level environment. Many photo voltaic cells can be operated at this increased temperature. The main problem with commercial solar panels is the encapsulation material used in solar panels for encapsulate and protect the solar cells. These material in many cases change the properties at these increased temperatures and low pressure. The increase in UV radiation is normally not a big issue as the commercial solar panels can withstand high levels of UV radiation. Therefore the tests have only been performed to simulate the thermal and low pressure environment. The solar panels can also be exposed to very low temperatures, down to -70 °C, especially during accent for shorter periods. This have not been included in this test.

The tests have been focusing on flexible panels with encapsulated photovoltaic cells of monocrystalline silicon mainly. These types of panels exist in many types and are manufactured by many different companies. The panels are designed for mounting on a rigid surface or in a frame. The mass is reasonable low (approx. 2 kg for 100 W) and also the price (approx. 300 € for 100 W). The panels are in most cases also very robust and can withstand mechanical stress and high levels of moisture/rain. This could in most cases result in multiple re-use of panels for multiple missions.

In the tests commercial-off-the-shelf, COTS panels and customized panels have been tested.

2 TEST SETUP

The tests have been performed in a vacuum chamber, with a pressure between 2.5 – 3 mbar. This is equivalent to a flight altitude of approximately 40 km. An aluminum heating plate of 700 x 600 x 8 mm painted black for higher thermal radiation. Was heated by resistive heaters and controlled by a temperature control unit was placed in the vacuum

chamber. The solar panels or the test samples were placed on the heater plate. The temperature was measured at different point on the solar panels and on the heater plate. The panels were heated to increasing temperatures and visually observed both during and after the tests. The main purpose of the tests has ben to verify that the panels can withstand the combination of high temperature and low pressure. No electrical measurements have been performed on the panels before, during or after the tests. The purpose of the tests have been to test the encapsulation material and techniques. The expected temperature on the solar panels during flight is approximately 90 °C. The maximum testing temperature have been 120 °C for margin in different configurations and environment conditions. The test period has been from hours up to a 8 days depending on the initial result in the tests. In the case of major failure of the panels the test has been terminated.

3 PERFORMED TESTS

A set of tests with different panels have been performed described below. The panels were observed during the test in the vacuum chamber through a small window in the chamber. It is important to be able to observe the panels during the tests as the expansion of the bubbles is at its maximum when the panel is at high temperature and in low pressure. After the test the bubbles shrinks or almost disappears, and the full impact of the expanding bubbles are difficult to observe.

3.1 Sunpower

The tested panel:

“SunPower SPR-E-Flex 50 Monocrystal Solar panel 50 W 12 V”.

https://sunpower.maxeon.com/int/sites/default/files/2019-10/sp_E_Flex_50W_UK.pdf

The panel was placed on the heating plate with the active side of the photo voltaic cells facing up. The temperature was measured at two different locations on both sides of the panel. The measured temperature on the upper side was a few degrees cooler compared to the lower side. The measured temperature on the panel was between 101°C – 97°C. Large bubble was observed after a short time, also “separation” of the different layers with resulting cracking of the photo voltaic cell at some positions. The test was terminated after 2 hours.

The panel was not qualified for operation in high temperature and low pressure.

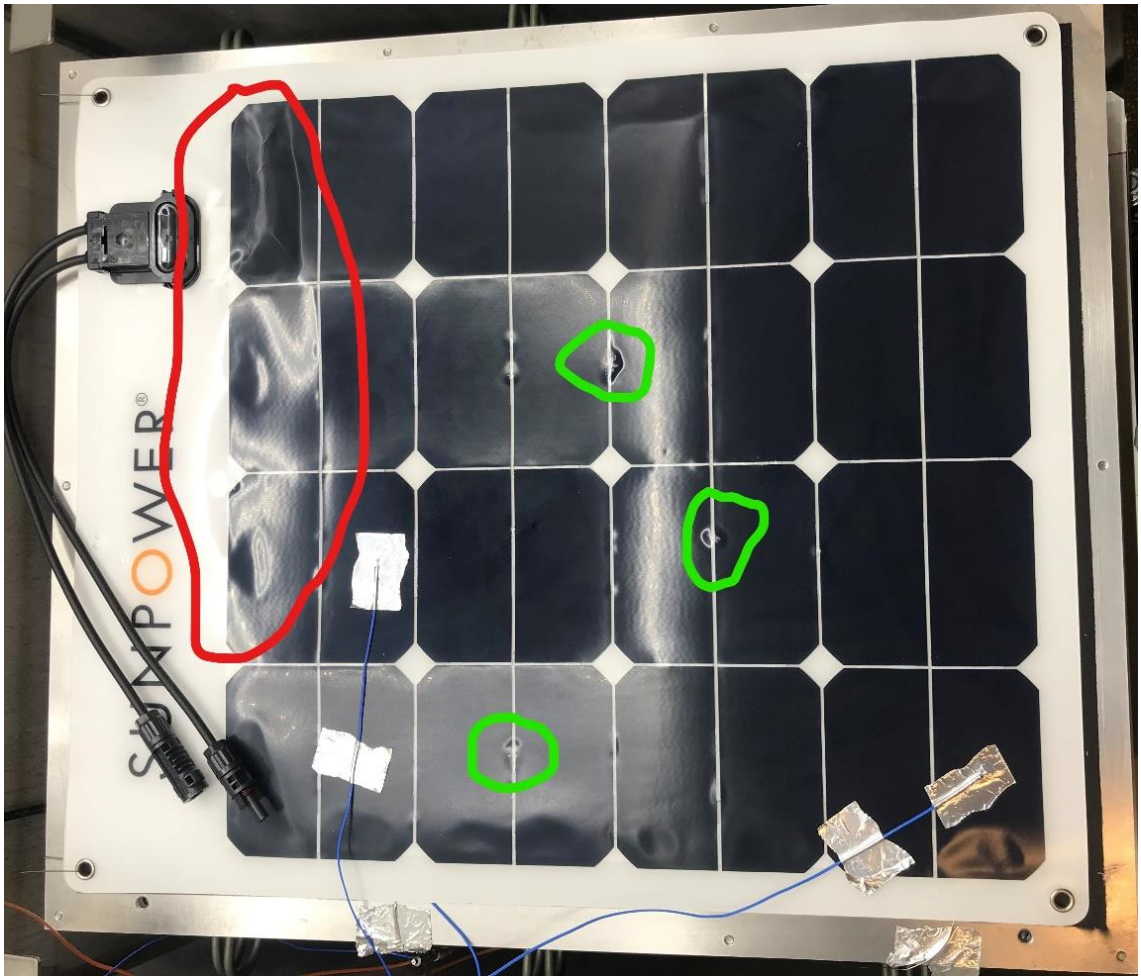

Figure 1 SunPower panel after test. Red area marks were major separation occurred with resulting cracks in cells. Green area marks some remaining bubbles.

3.2 Sunbeam

The tested panel:

"Sunbeam Though Flush, 54 W".

https://www.sunbeamsystem.com/tough-series/

The panel was placed on the heating plate with the active side of the photo voltaic cells facing up. The temperature was measured at two different locations on both sides of the panel. The measured temperature on the upper side was a few degrees cooler compared to the lower side. The measured temperature on the panel was between 102°C – 94°C. Large bubble was observed after a short time, also "separation" of the different layers especially top layer at some positions. The test was terminated after 4 hours.

The panel was not qualified for operation in high temperature and low pressure.

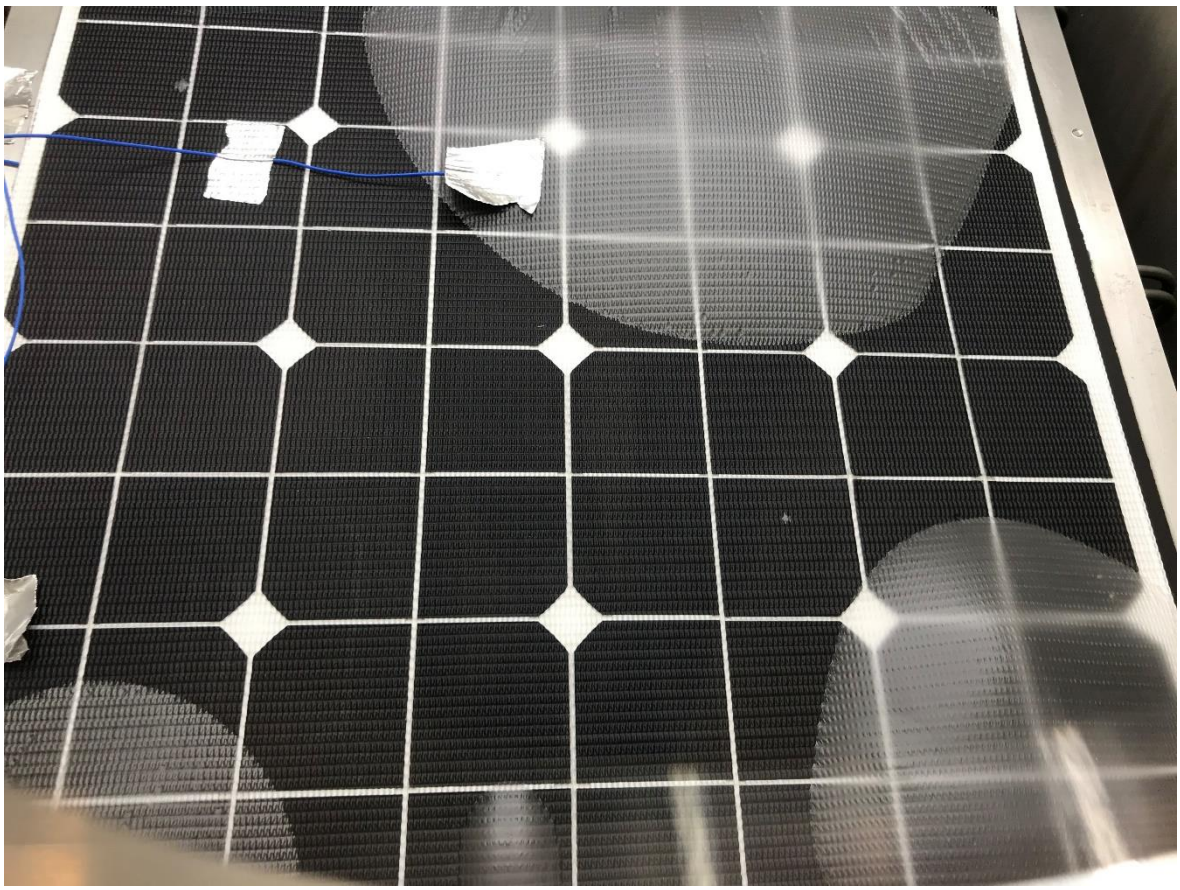

Figure 2 Sunbeam pane,l picture taken during test in vacuum chamber. Large bubbles separation of top layer.

3.3 Midsummer

The tested panel was a test sample received from the manufacturer Midsummer, https://midsummer.se/en/ . The cells are of thin film type.

The panel was placed on the heating plate with the active side of the photo voltaic cells facing up. The temperature was measured at one location on both sides of the panel. The measured temperature on the upper side was a few degrees cooler compared to the lower side. The measured temperature on the panel was between 103°C – 97°C. Large bubble was observed after a short time, also “separation” of the different layers at some positions. The test was terminated after 6 hours.

The panel was not qualified for operation in high temperature and low pressure.

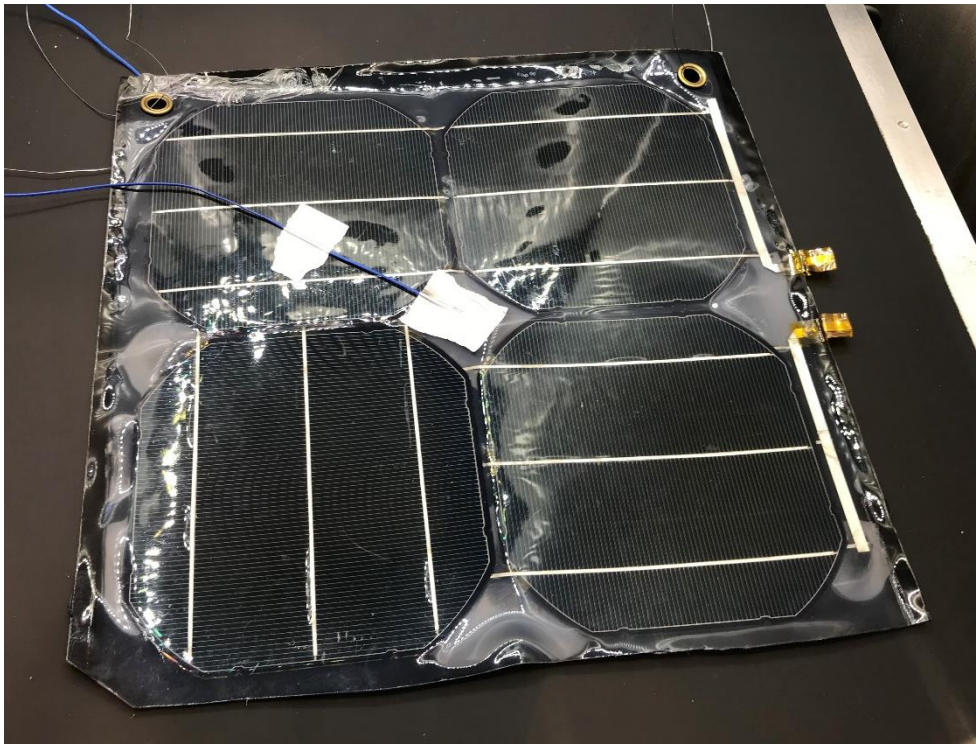

Figure 3 Midsummer test sample on heater during test inside vacuum chamber

3.4 MitoSolar

MitoSolar delivered different test samples for the tests. The test samples were manufactured after discussions between SSC and MitoSolar. The samples were of two types, the "standard" lamination with polyolefin similar to the COTS panels and another epoxy-based lamination for high temperature applications.

3.4.1 Standard lamination

Two different test samples were tested that was received from the company MitoSolar, https://www.mitosolar.com of the standard lamination type . The two samples were similar in material and design ("Non cross linked BPO" and "Crossed linked high-temp TPO").

The panels were placed on the heating plate with the active side of the photo voltaic cells facing up. The temperature was measured at three locations on the side facing up. The measured temperature on the panels was between 102°C – 95°C. Large bubble was observed after a short time, also "separation" of the different layers at some positions. The photo voltaic cells also cracked in some places due to the large deformation of the lamination material. The test was terminated after 1 hour for the "BPO" and after 2 hours for the "TPO".

The panel was not qualified for operation in high temperature and low pressure.

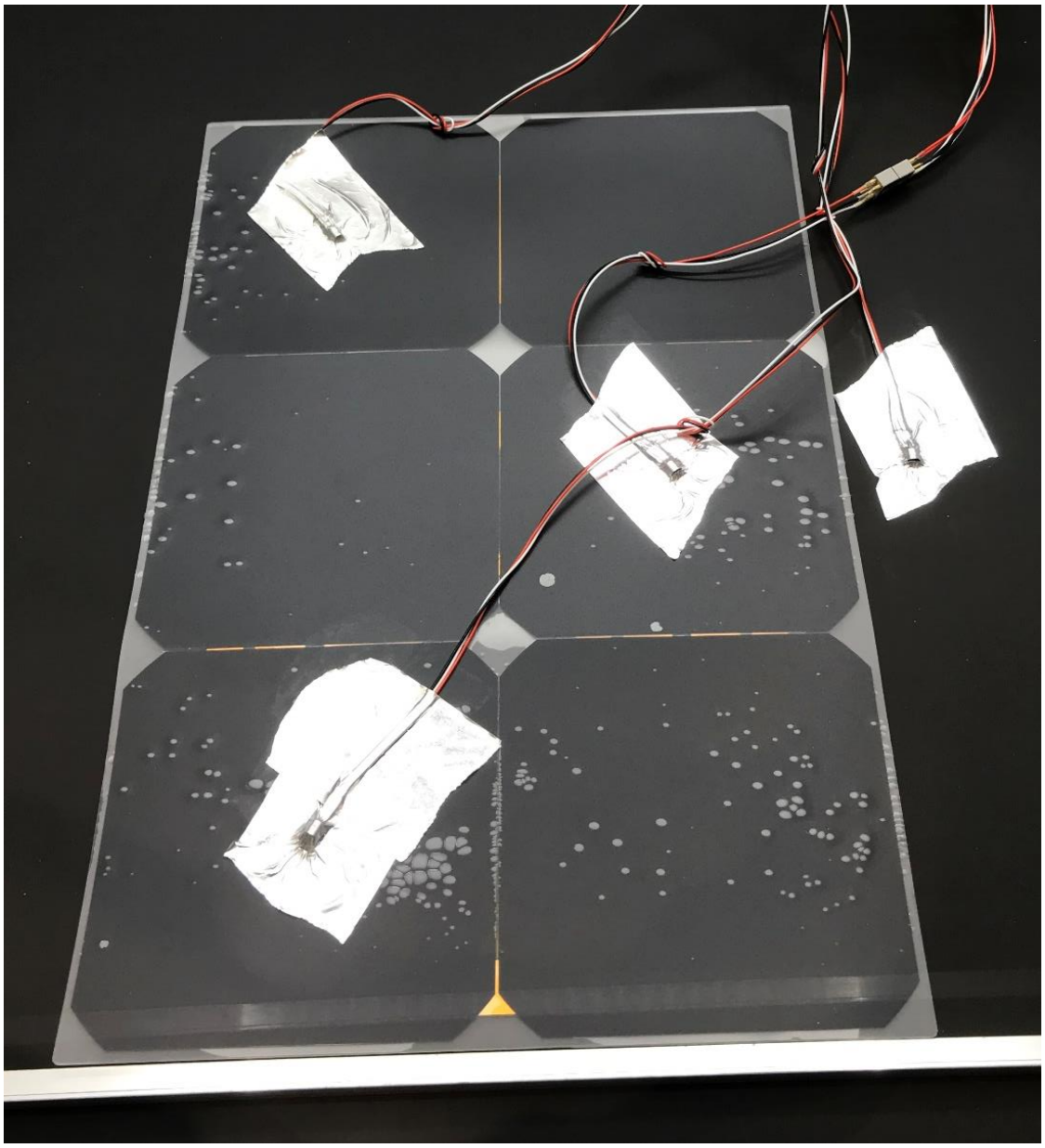

Figure 4 BPO test sample in vacuum chamber during test

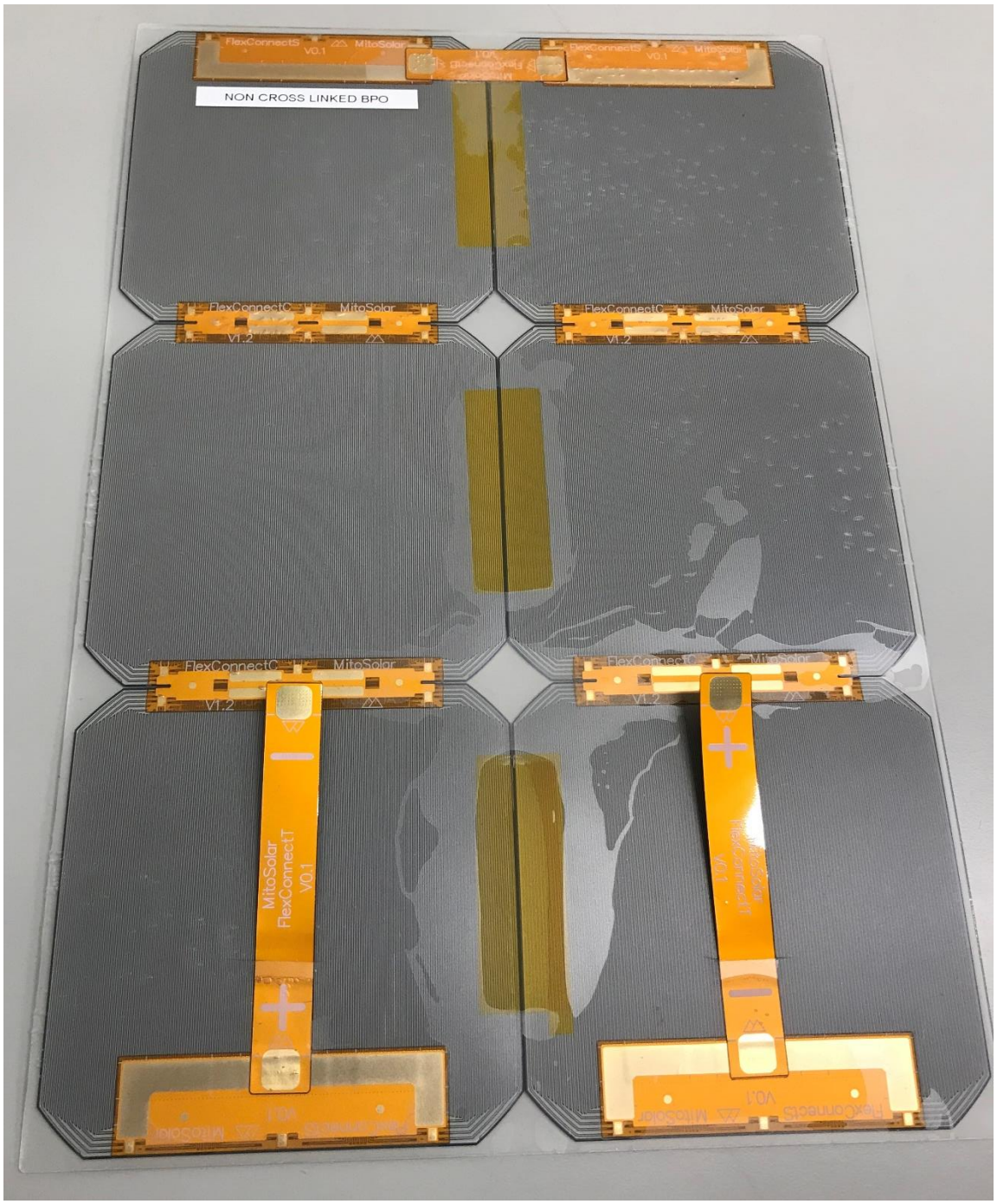

Figure 5 BPO test sample backside after test

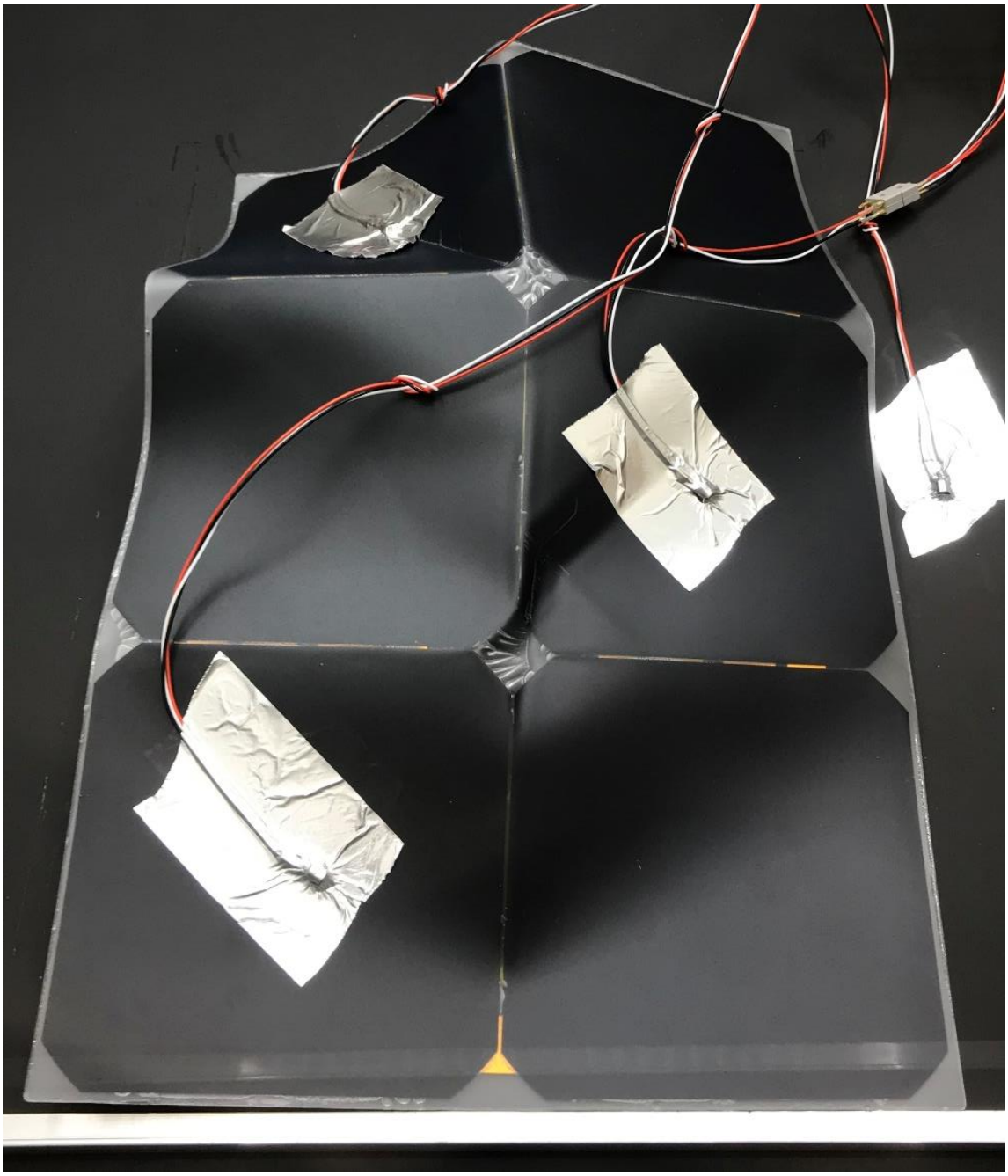

Figure 6 TPO test sample in vacuum chamber. Large deformation of sample due to separation and large gas bubbles.

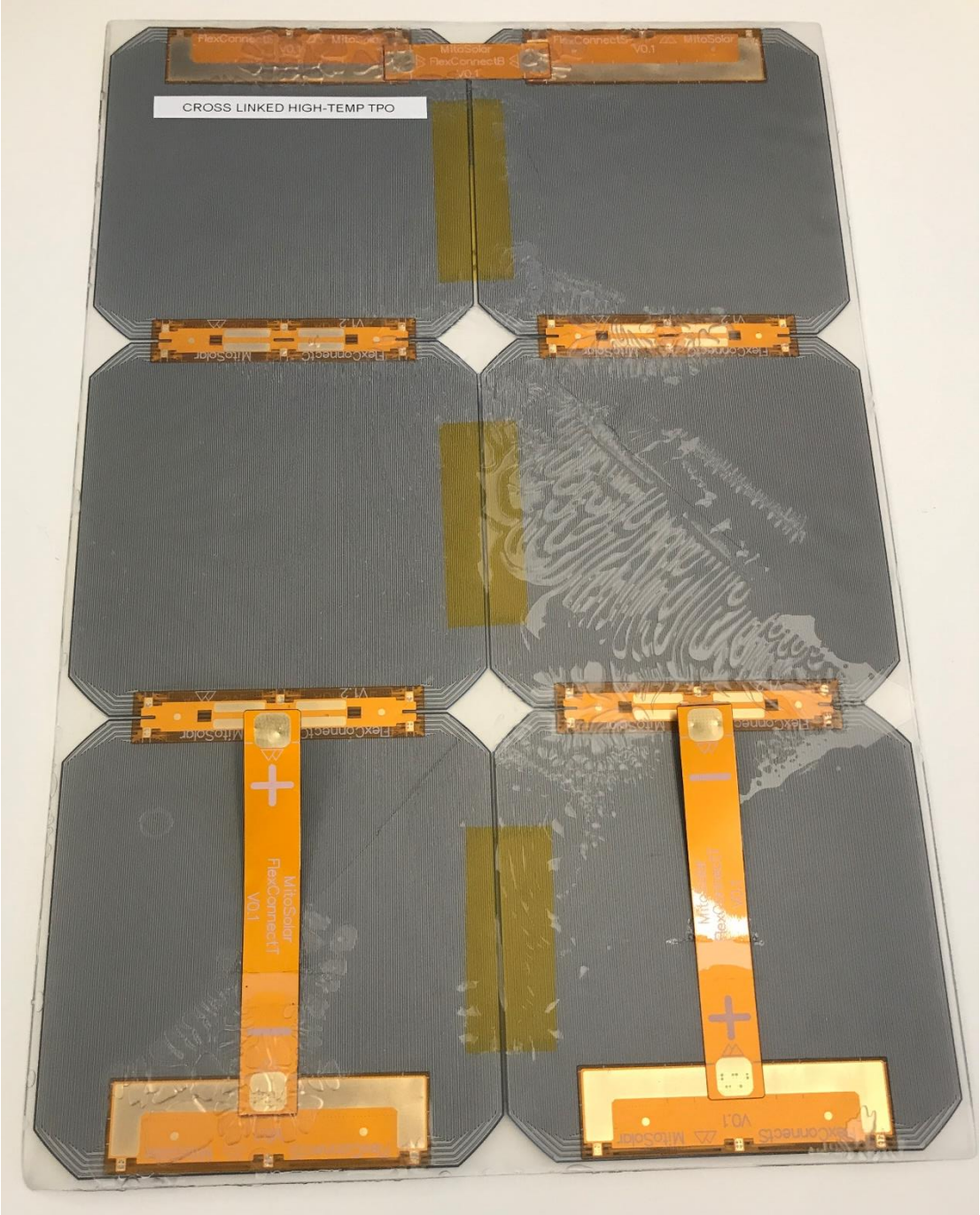

Figure 7 TPO test sample backside after test

3.4.2 High temperature lamination

Two different types of test samples were tested that was received from the company MitoSolar, https://www.mitosolar.com . The two type of samples had the same basic design with an epoxy lamination of the cells. The first type that was delivered in two copies comprised the lamination with the cells. The second type comprised the lamination of the cells and added aluminium honeycomb structure on the backside for higher stiffness of the sample.

Test of only lamination samples:

The two samples were placed on the heating plate one sample with the active side of the photo voltaic cells facing up and the other sample with the cells facing down. The temperature was measured at two locations on the side facing up. A test with increasing set temperature from 80°C to 110°C was performed for 2 days. A second test was performed with set temperature of 120 °C for 5 days continuously. The measured temperature on the panels during the test was between 120 – 118 °C. No bubbles or any other mechanical changes could be observed during or after the test. A slight increased “milkiness” could be observed in the lamination after the test.

Figure 8 Epoxy laminated test sample after test

Test of lamination and honeycomb sample:

The sample was placed on the heating plate with the active side of the photo voltaic cells facing up. A test with set temperatures of 90 and 100 °C was performed for 28 hours. The measured temperature on the test sample on the top surface was between 77 and 89 °C. No changes could be detected on the sample.

In general, the temperature difference on test sample between the side facing the heater plate and the opposite side was approximately 7 – 10 °C. For a more realistic test the samples were placed with the photovoltaic cells down towards the heater plate in the remaining test.

The sample was placed on the heating plate with the active side of the photo voltaic cells facing down for better simulating the real case situation. A test with set temperatures of 120 °C was performed for 8 days continuously. The measured temperature on the test sample on the top surface (backside of sample) was between 113 and 114 °C. The chamber was opened once briefly during the test for a visual inspection of the sample. No changes could be detected at this stage or after test was terminated.

Both the panel was qualified for operation in high temperature and low pressure.

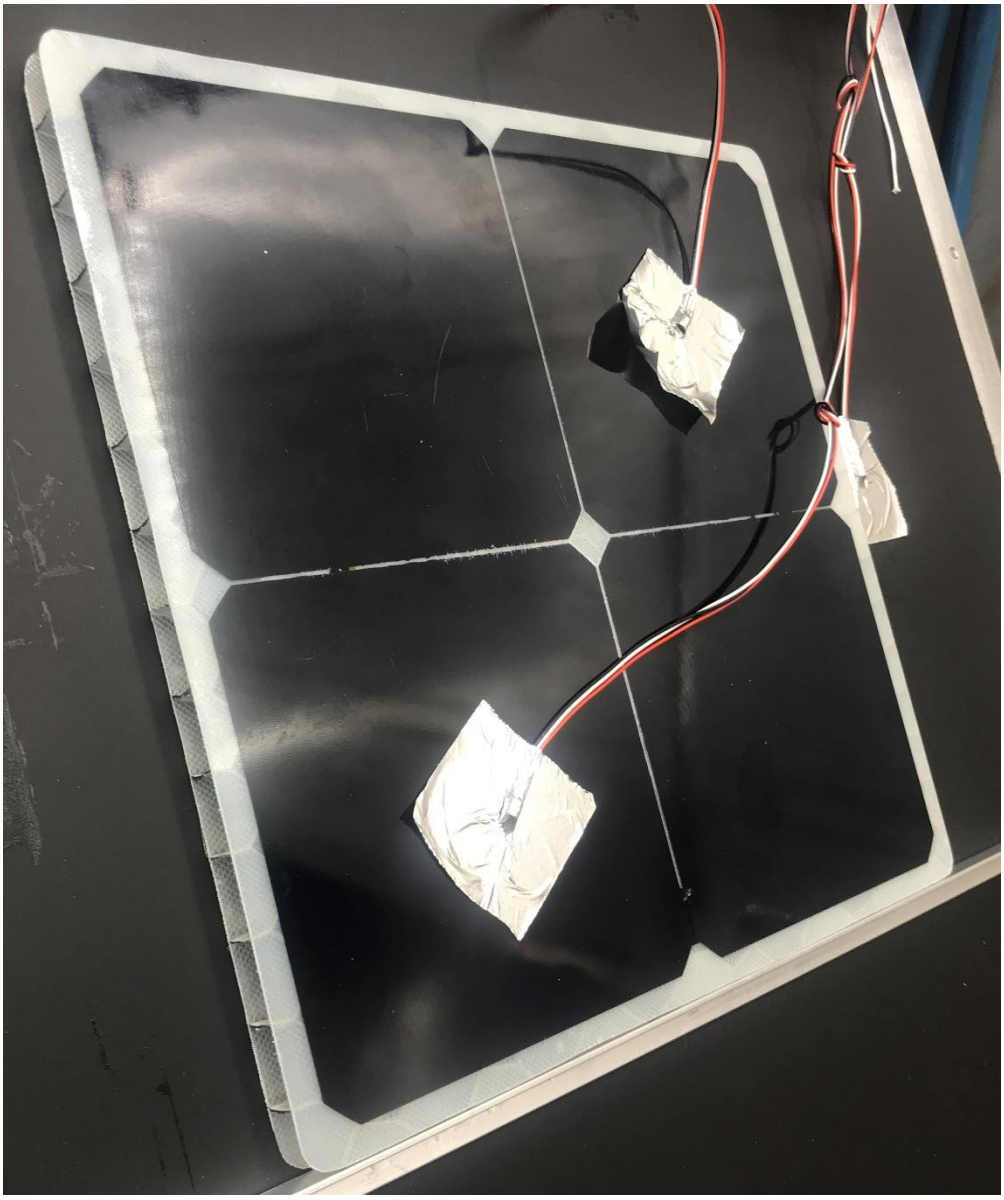

Figure 9 Epoxy laminated test sample with honeycomb structure on heater plate in vacuum chamber.

4 RESULTS AND CONCLUSION

The COTS and some of the test samples have an encapsulation material of EVA (ethylene vinyl acetate), polyolefin or similar. These or similar materials are common encapsulation material in thin and flexible solar panels. There is a major problem with this type of design in applications with high temperature and low pressure. The encapsulation material gets soft at higher temperature and there is also a process of outgassing inside the encapsulation or expansion of enclosed gas bubbles. This results in a major mechanical failure of the

panels as the gas bubbles expands inside the soft encapsulation material at the low pressure. The result is similar in all tested panels with this type of materials. The conclusion is that this type of solar panels are not suitable for use in stratospheric ballooning.

The second type of panel that was tested had a similar design, but the encapsulation material was an epoxy-based material. This gives a similar product that is thin and flexible (maybe a little more rigid due to the epoxy) and reasonable low mass. No changes could be observed on the panels during or after the tests. There was no softening and no gas bubbles could be detected. This design was concluded that it could be used at high temperatures and low pressure as experienced during stratospheric ballooning.

Manufacturer	**Type**	**Result**
Sunpower	SPR-E-Flex 50	Negative
Sunbeam	Though Flush, 54 W	Negative
Midsummer	Test sample, thin film	Negative
Mitosolar	Standard lamination	Negative
Mitosolar	Epoxy-based lamination	Positive

Table 1 Summary of test results. The result "Negative" is meaning that the outcome of the test shows that the tested item could not be used at high temperature and low pressure. The result "Positive" means that the tested item could be used at high temperatures and low pressures.

STU-IRS-S-PRO-1112-01-v1.0_Image-Stabilization-System-Simulations_2021-07-16

STUDIO IMAGE STABILIZATION SYSTEM SIMULATIONS

Version 1.0

16.07.2021

Status: Released

H2020 INFRADEV-01-2017 project "European Stratospheric Balloon Observatory *Design Study*"

Topic: INFRADEV-01-2017 Design Studies

Project Title: European Stratospheric Balloon Observatory *Design Study* – ESBO *DS*

Proposal No: 777516 – ESBO DS

Duration: Mar 1, 2018 - Feb 28, 2021

WP (EU)	WP 12
WBS Item (internal)	823
PBS Item(s)	1112
Title	Image Stabilization System Simulations
Description	Report on Control Theoretical Simulations of the STUDIO Image Stabilization System
Lead Beneficiary	"USTUTT"
Nature	"Report"
Dissemination Level	"Public"
Est. Del. Date	-
Version	1.0
Date	16.07.2021
Status	Released
Lead Author	Thomas Roth, USTUTT, troth@irs.uni-stuttgart.de
Approved by	

TABLE OF CONTENTS

LIST OF ABBREVIATIONS AND DEFINITIONS

Abbreviation	Definition
ESBO *DS*	European Stratospheric Balloon Observatory *Design Study*
ISS	Image Stabilization System
STUDIO	Stratospheric Ultraviolet Demonstrator of an Imaging Observatory

REFERENCE DOCUMENTS

[RD1]	Roth, T., Simulation and Controller Design of a Closed-Loop Image Stabilization System for an Astronomical Balloon Platform, January 2021.
[RD2]	ESBO *DS* D2.1-1 Requirements Baseline UV.

1 SCOPE

This document describes Matlab/Simulink simulations that were carried out in order to identify and examine potential control laws for the STUDIO Image Stabilization System (ISS).

The simulations were carried out at USTUTT in support of the ISS development at CSIC/IAA.

2 FULL SYSTEM ARCHITECTURE AND REQUIREMENTS

The Image Stabilization System (ISS) ensures the stability of scientific images in the UV instrument, even when the telescope pointing is slightly disturbed during their exposure. Such pointing disturbances can be the result of internal influences (e.g. limited Attitude Control System (ACS) stabilization quality, structural vibrations from equipment), or external influences (gondola pendulation caused by atmosphere). If not corrected, these instabilities can cause blurred frames of less scientific value.

The ISS is a closed-loop control system (see Figure 1). By slightly rotating the mirror M3 in the optical path, it can shift the image in both the UV instrument and VIS camera. The ISS measures the current image stability with the VIS camera frequently (100 Hz). A bright guide star's location is identified and tracked in its images by a centroiding algorithm. It is executed on the camera frame grabber (FPGA). From this centroid measurement, a control algorithm running on the OBC computes an angular position command to a piezo-actuated Tip-Tilt Platform (TTP) attached to M3. The control algorithm must rotate the mirror such that the guide star in the VIS images always stays at the same location.

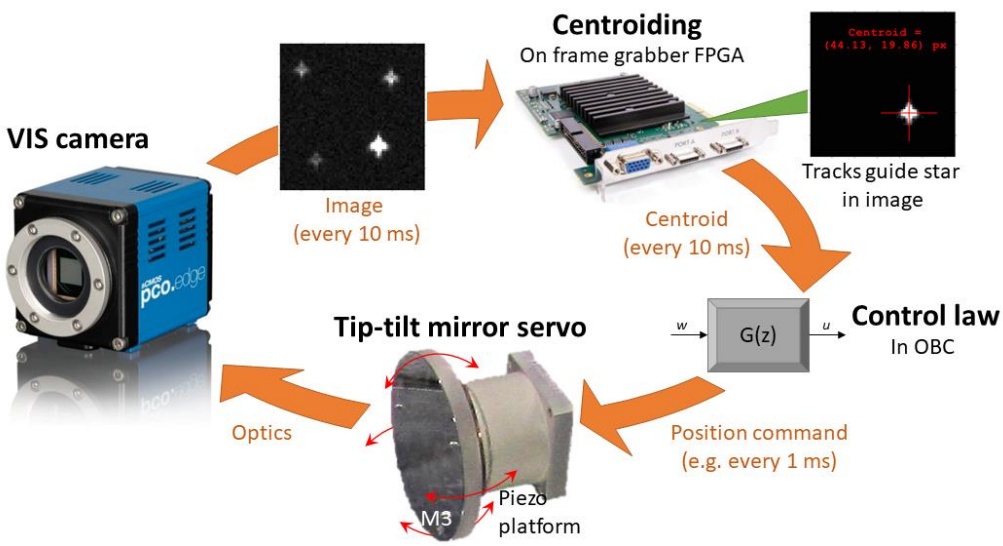

Figure 1: ISS control loop concept

This task is described in more detail by the pointing system requirements (see [RD2], p. 14). The most important consequences for the system and controller design are:

- GF-UV-TEL-02a: The guide star shall stay within 0.5 arcsec ≙ 2.5 pixels (assumed to be 3σ) of its target position in the VIS camera image.
- GF-UV-TEL-03: Pointing disturbances up to ± 40 arcsec should be expected.
- RF-UV-TEL-04: The centroid accuracy shall be < 2.5 pixels.

Other design factors from initial calculations influencing the control loop are:

- Intended VIS camera integration time of 0.01 s.
- Guide star apparent magnitude range 7 mag to 9 mag.
- To fulfil the control task, the centroid accuracy should be < 0.2 pixels.

To support the design of viable control laws, the ISS was modelled in Matlab/Simulink as part of a Master Thesis at USTUTT [RD1]. For further information on any chapter of this document, or to obtain the model files referenced, please contact:

- Philipp Maier (pmaier@irs.uni-stuttgart.de)
- Thomas Roth (tsroth@live.de)

3 EXPECTED DISTURBANCES

In the absence of measurements or accurate predictions of the pointing disturbance environment expected for STUDIO, data for similar astronomical stratospheric balloon missions was employed. The spectral characteristics of the disturbances were of special interest for the controller design.

Literature on several missions reports gondola pendulations excited by residual atmosphere between 0 – 1 Hz. It may cause large gondola rotations, but these are reduced to an image instability of at least < 40 arcsec by the ACS pointing control (Requirement GF-UV-TEL-03). Further, vibrations from mechanical equipment (e.g. motors) were found to cause narrow-band spikes approximately between 10 Hz – 50 Hz. Finally, low-amplitude wide-band disturbances were reported.

A dataset of measured pointing disturbances (arcsec on-sky over time) from the BRRISON mission was kindly provided by the BRRISON team (see Figure 2). It employed a telescope- and fine-pointing system similar to STUDIO. Hence, the data was considered representative for the expected disturbance environment on STUDIO. It conforms with the above descriptions from literature. Artifacts rendered parts of the data less useful, so 4 representative segments of 1 min length were selected for control law verification. To remain conservative, the data amplitude was scaled by factor 4, resulting in a peak-to-peak amplitude of approximately ± 40 arcsec (RF-UV-TEL-04).

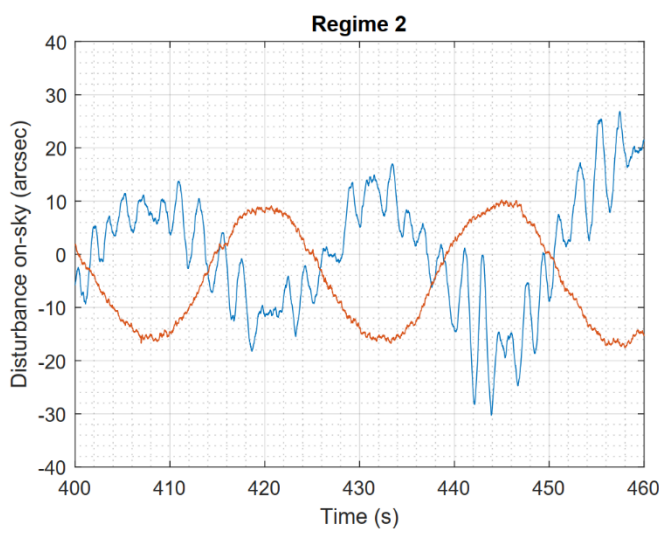

Figure 2: BRRISON pointing disturbance dataset excerpt (amplitude scaled x4)

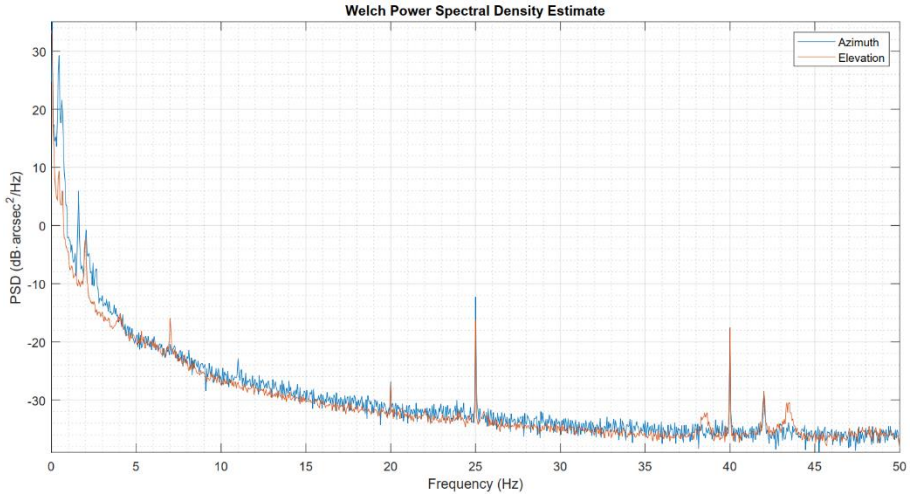

Figure 3: BRRISON pointing disturbance dataset spectral analysis

4 IMAGE STABILIZATION SYSTEM MODEL

This section gives an overview of the mathematical models employed to simulate the ISS closed-loop behavior. Each component or effect that plays a role in the stabilizing of the telescope image was modelled separately, either as a Matlab function or a Simulink model chart. All of these submodels were combined into a Simulink model of the entire closed-loop ISS.

4.1 FULL MODEL

The closed loop ISS Simulink model is shown in Figure 4. Each submodel is represented by a Simulink block. The controller on the left (not shown, squiggly line) provides an angular position

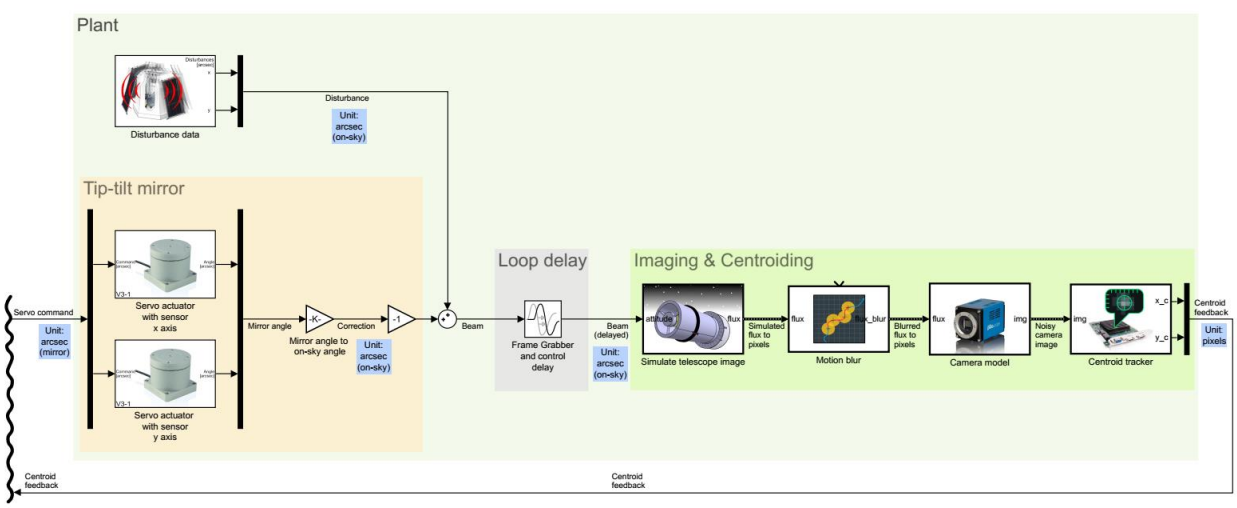

Figure 4: Complete ISS Simulink model

command to the 2 independent TTP axis models (yellow area). Multiplication with a constant vector (yellow area) representing the optical path geometry and reflection at M3 yields the current displacement of the guide star image on the focal plane on account of the mirror's rotation alone. The current telescope pointing disturbance from the dataset is then added (pale-green area).

Consequently, the current location of the guide star's image on the focal plane is described by the signal named 'Beam'. This signal represents the image stability in the VIS camera and UV instrument alike, and was used to gauge the fulfillment of requirement GF-UV-TEL-02a. The blocks in the bright-green area simulate a noisy, blurred camera image with the guide star at the calculated location. Finally, a prototype of the centroiding algorithm (bright-green area) estimates the location of the guide star in the simulated image, and feeds back that information to the controller. A delay block in the model (gray area) simulates the estimated transmission and processing times (the delays occur after the camera, centroiding, and controller in reality; the block is located before the image generation for technical reasons).

4.2 SUBMODELS

4.2.1 Telescope optics

A simplified, geometric model of the telescope's optical path provided important information on the relationship of the other submodels. With some reasonable assumptions, a linear relationship between distances on the focal plane (pixels), telescope attitude (arcsec), and TTM rotation angle (µrad) could be derived. For each 1 pixel the guide star moves in the VIS camera image, the telescope has rotated 0.206 arcsec away from its intended pointing. To bring the guide star back to its desired position in the image, the TTM needs to rotate 4.889 µrad per 1 pixel displacement in the cross-elevation axis (x-axis), and 4.637 µrad per 1 pixel displacement in the elevation axis (y-axis). In the real system, these values are subject to calibration.

4.2.2 Camera image simulator

To determine the accuracy of centroid measurement under realistic conditions, a library of Matlab functions was programmed to generate artificial camera images. They use the VIS camera Point Spread Function (PSF) from optical simulations and estimated optical losses to give stars a diffracted, realistic appearance. Several camera noise sources are simulated using statistical models, including shot noise, dark current, readout noise, and sensor non-uniformities. Additional features include the simulation of faulty pixels, motion blur (FOV moves during exposure), and multiple stars of different brightnesses inside the FOV.

4.2.3 Centroiding algorithm

The centroiding algorithm for the STUDIO ISS is based on a proven algorithm from the SOFIA telescope. SOFIA's algorithm was recreated in Matlab to test its accuracy under STUDIO's conditions. It receives a camera image (arbitrary units), applies some pre-filters (thresholding, rejection of isolated bright pixels), and calculates the guide star's centroid location (in pixels) using the (modified) moment method.

4.2.4 Tip-tilt mirror system (TTM)

The dynamic behavior of the TTM is modeled in Simulink. A single rotation axis (x or y) is modeled, since both are independent and constructed identically. The model receives an angular position command as input, and outputs the actual angle of the mirror M3. The piezo-actuated Tip-Tilt Platform (TTP) hardware is modeled as a limited 2nd order transfer function (spring-mass-damper-system). It omits non-linearities, hysteresis, and changes over time that often occur in piezo actuators, since these effects are mitigated by a servo-controller. This servo controller within

the platform's driver electronics measures the true angular position and ensures it accurately matches the commanded position. It was modeled with information kindly provided by the manufacturer. The model includes a PID controller, an anti-resonance notch filter, a rate limiter and a simplified angular position sensor model.

4.2.5 Disturbances

To represent the pointing disturbance environment, segments of the BRRISON dataset described in 4.2.5 are fed directly into the model.

5 CONTROLLER DESIGN AND SIMULATION

First, the dynamic properties (e.g. Bode diagrams) of the ISS model were calculated by Simulink. On this basis, the controller design goals in the following sections were formulated. Controller candidates were constructed, optimized, and tested directly inside the ISS model. Their performance was validated by simulating the model and assessing the image stability via the standard deviation of the model's 'Beam' signal.

5.1 METHOD

5.1.1 Bandwidth

In control theory, the closed-loop bandwidth is the maximum frequency that a controller is capable of correcting. Based on the model's dynamic properties, it was concluded any sufficiently stable controller's bandwidth would need to be < 30 Hz. Even then, the closed-loop system would amplify disturbance frequencies beyond the control bandwidth, making it impossible to meet the control accuracy requirement. Only for bandwidths roughly < 15 Hz could this effect be mitigated. To raise the bandwidth beyond this limit, faster camera integration times would be necessary. This in turn would require brighter guide stars, thus limiting observation options, and was therefore not considered further.

5.1.2 Order

Due to the discussed bandwidth limit, the high frequency vibrations in the disturbance (e.g. 25 Hz or ~ 40 Hz peaks in Figure 3) cannot realistically be addressed by the ISS. A detailed analysis of the spectral distribution of disturbance amplitudes showed that disturbances > 12 Hz alone did not exceed the image stabilization requirement GF-UV-TEL-02a. On the other hand, they revealed the largest disturbance amplitudes to be at (very) low frequencies of 0.04 – 3 Hz. Hence, it was decided to ignore high frequencies and focus on correcting low frequencies as much as possible. A rough pointing budget confirmed the feasibility of this approach. To provide sufficiently strong low-frequency damping for this to work, the ISS controller needed to be of at least 2nd order. Furthermore, it must contain at least 1 integrator to ensure steady-state accuracy.

5.1.3 Open-loop shaping workflow

To simulate the controller, a continuous transfer function Simulink block was added to the model. Based on the previous paragraphs, the goal was an open-loop transfer with a 0 dB Bandwidth of 12 Hz and comfortable stability margins. Simulink's 'Control System Designer' was used to set

the controller transfer function's poles and zeros. This tool draws the open-loop Bode diagram based on the controller's and ISS model's poles and zeros. In a heuristic, iterative process, good locations for the controller's poles/zeros were identified. Success was evaluated not only by how well the Bode diagrams met the design goals, but also by running simulations to evaluate closed-loop image stability directly.

5.2 CONTROLLER CANDIDATES

5.2.1 PI+I controller

The result of the open-loop shaping is the following controller:

Order 2 ; 2 poles $s_{p1,p2} = 0$; 1 zero $s_{z1} = -10$

Transfer function:

$$G(s) = \frac{k_1 \cdot s + k_2}{s^2} = k_1 \cdot \frac{(s + \frac{k_2}{k_1})}{s^2} = \frac{1}{s} \cdot \left(k_1 + \frac{1}{s} \cdot k_2\right)$$

$$\text{with} \quad k_1 = 80 \quad ; \quad k_2 = 800$$

This is in effect a proportional-integral-controller (PI) with an additional integrator (I) in series. Hence the name PI+I controller.

Each axis (x and y) in the ISS model was given an independent, identical copy of this controller. Replacing the continuous (theoretical) transfer function with its discrete counterpart (update rate 1 kHz) did not cause any deterioration of control performance. Initial problems with instability after step commands (e.g. on switch-on) caused by integrator windup could be solved by deploying anti-windup measures and/or temporarily switching to a less aggressive controller.

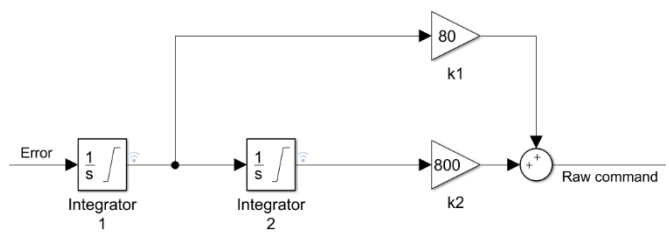

Figure 5: Block diagram of the PI+I controller

5.2.2 Estimator: up-sampling and delay compensation

The goal of focusing on high-amplitude, low-frequency disturbances means that accurately tracking long, predictable slopes (i.e. flanks of a sine-wave) in the disturbance is especially important. These high-rate disturbance slopes can produce some image instability even during the exposure time in between centroids. Furthermore, some control inaccuracy during testing could be attributed to delay in the system.

To address these issues, an Estimator (EST) was created in addition to the PI+I controller. It can reconstruct the current pointing disturbance by combining the centroid and the currently commanded TTM position (≅ current actual TTM position). By extrapolating linearly from a number of previous measurements (linear least squares fitting), the gaps in between camera images can be filled with artificial, predicted centroids. This enables the controller to track long-term trends (over 100s to 1000s of ms) more accurately. Extrapolating slightly into the future can mitigate negative delay impact. As drawback, this extrapolation does not perform well when disturbances with high frequency oscillations or peaks occur.

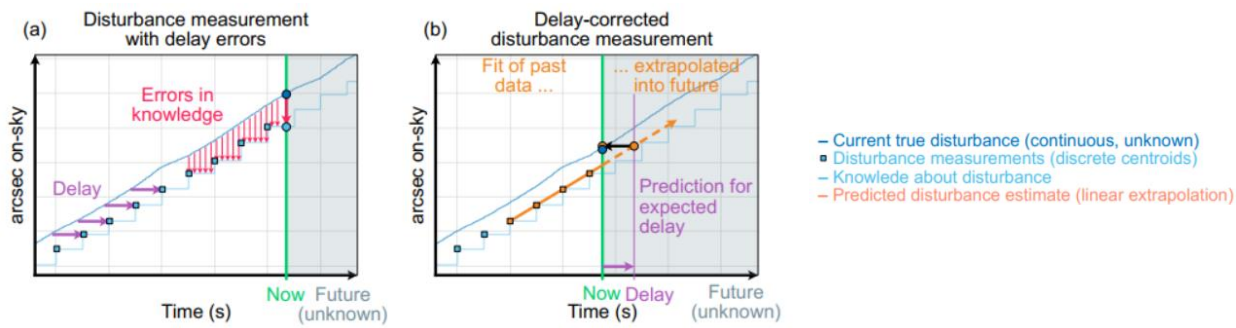

Figure 6: Illustration of the Estimator's concept

A Kalman update equation was added to always provide the best compromise between extrapolated prediction (slopes) and real measurements (peaks). After implementing this Estimator as Matlab code and adding it into the Simulink ISS model, its parameters (e.g. number of datapoints used to extrapolate from) were systematically optimized for the best image stabilization performance.

While intended for use in combination with the PI+I controller, the estimator could also be used as a controller on its own. This approach was later abandoned.

5.3 CONTROLLER PERFORMANCE VALIDATION

Table 1: Comparison of controller candidates
(✓: requirement met, *: with anti-windup measures)

Controller	Image stability 3σ in arcsec on-sky				Tradeoff			
	Nominal [2]		Extreme [1]		Accuracy	Complexity	Stability	Robustness
PI+I	0.49	✓	0.61		o	+	+*	o
EST + PI+I	0.46	✓	0.58		+	o	+*	o
EST direct	0.42	✓	0.50	✓	+ +	− −	+	−

All of the mentioned controller designs were simulated extensively in the ISS Simulink model to verify their performance in different circumstances. The PI+I controller on its own could narrowly fulfill the image stability requirement GF-UV-TEL-02a (see Table 1). Adding the Estimator before the PI+I controller (EST+PI+I, see Figure 9) offered an improvement in performance. The best performance was achieved using the Estimator directly as controller. However, this approach

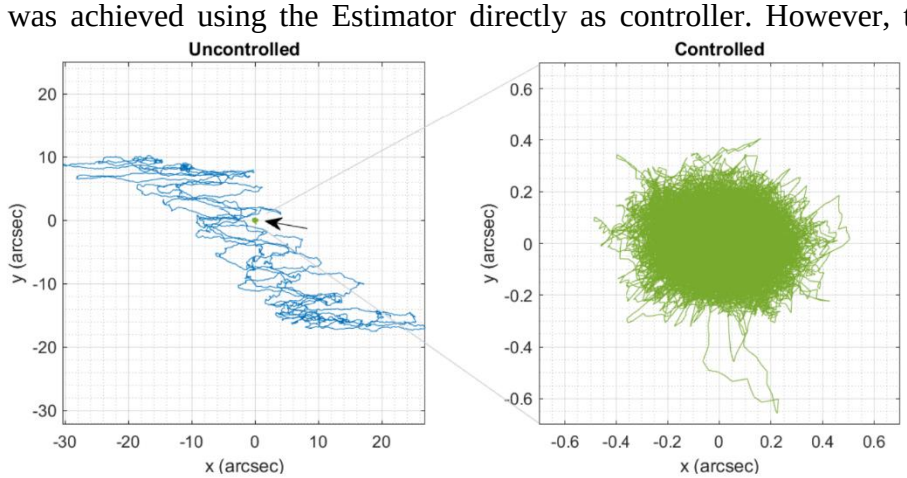

Figure 7: Example of a simulation result. Left: without controller (disturbance), right: with controller.

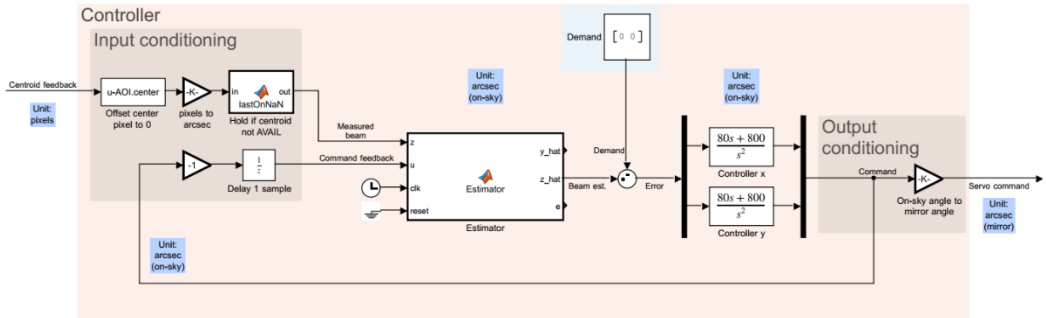

Figure 8: Simulink implementation of the EST + PI+I controllers for both axes. In the ISS model (Figure 4), placed on the left (squigly line).

would require more inputs (in hardware), and was more sensitive to changes in the ISS model parameters than the other options. Therefore, it was not considered for further development.

On account of these encouraging results, the PI+I controller with optional Estimator were implemented in C++ for the flight software (alongside a classic PID controller as backup). However, care should be taken to properly mechanically damp and isolate the telescope nonetheless. If much stronger than expected high-frequency disturbances occur in STUDIO (i.e. undamped vibrating equipment), the proposed controllers will not be able to compensate due to their limited bandwidth.

6 EXPERIMENTAL MODEL VALIDATION

Across several experiments, many of the models supporting the controller design process could be validated.

6.1.1 Camera image simulator

By comparing artificially generated images to images taken with the actual camera hardware, the statistical camera noise models could be validated for the purposes of this simulation. Regarding the appearance and brightness (VIS PSF, losses) of a star seen through the telescope, no experiment has been conducted yet.

6.1.2 Centroiding algorithm

A test rig was constructed using the VIS camera hardware (see Figure 10). A wide-angle objective was mounted on the camera and pointed at a TV monitor displaying an artificial star (appropriately

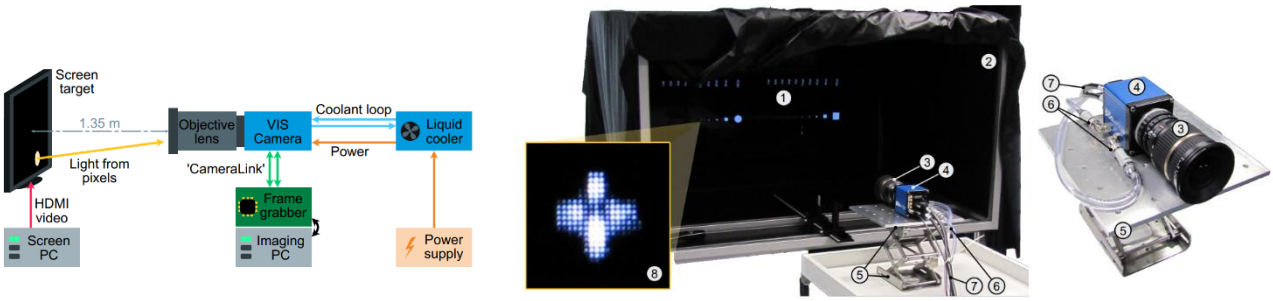

Test rig. (1) Screen target (showing calibration image), (2) Aluminium box structure with fabric covering, (3) Objective lens, (4) Camera, (5) Baseplate on scissor jack for height adjustment, (6) Coolant tubes, (7) Power and data cables, (8) Close-up of artificial star on screen shaped like PSF V2E.

Figure 9: Test rig for camera and centroiding model validation

scaled image of the VIS PSF). The objective aperture was adjusted so the brightness of the star seen through the camera matched the simulated brightness for a star of magnitude 7 mag or 9 mag. The images taken this way strongly resembled the artificial simulated images. The original SOFIA algorithm's Matlab implementation was then applied to the real camera images. The resulting centroid stability (3σ norm) was nearly identical to the centroid accuracy predicted by simulations (see Table 2).

On the same rig, centroids calculated by STUDIO's Frame Grabber hardware were stored. Owing to limitations of the FPGA, the centroiding algorithm in the STUDIO Frame Grabber has some differences to that of SOFIA. With appropriate image filter settings (threshold, bias) the STUDIO algorithm's centroid stability (3σ norm) was only slightly worse than that of the SOFIA algorithm (see Table 2).

Table 2: Centroiding accuracy validation: worst-case (9 mag star, 10 ms integration time)

Method	Centroid stability (3σ) Unit: pixels
Goal	< 0.2
Simulation (SOFIA algorithm)	0.12
Experiment – SOFIA algorithm	0.122
Experiment – STUDIO frame grabber algorithm	0.16

The SOFIA centroiding model in Matlab is thus validated as an optimistic estimate of the real STUDIO centroiding performance. Both algorithms achieve the 0.2 pixel 3σ norm accuracy goal, which should be sufficient for accurate ISS control.

6.1.3 Tip-tilt mirror system (TTM)

The step response of the flight hardware TTP with M3 mounted was compared to a simulated response. The real system exhibited a faster rise time and less overshoot than the model. Hence, the TTM model can be considered validated as a conservative estimate of the TTM dynamics. On top of that, the TTP never exhibited any undesirable behavior (e.g. resonance) during testing, even when given extreme commands (sawtooth of amplitude ± 1000 µrad (max. movement range) and frequency 100 Hz).

6.1.4 Disturbances

No measurements of telescope vibration on the gondola or gondola pendulations have been possible to date.

6.1.5 ISS closed-loop end-to-end test

Preparations have been made to test all ISS hardware and software components in conjunction on a test rig mimicking STUDIO's optical bench geometry (see Figure 11). A dim, collimated laser beam simulates the guide star. In the optical path, the beam is first disturbed using a Tip-Tilt Mirror identical to the one in the ISS. This Disturbance-TTM could retrace the BRRISON disturbance dataset, for example. Then the disturbed laser beam is reflected from the flight-hardware TTM

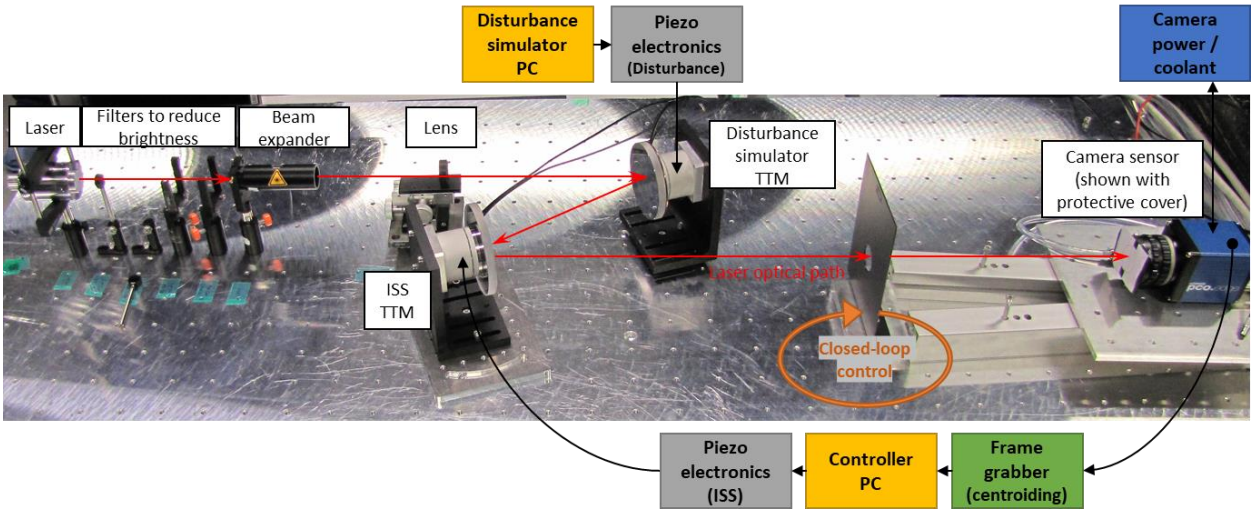

Figure 10: Test rig for ISS closed-loop, end-to-end test

before directly striking the camera sensor. The images from the camera are read and centroided by the Frame Grabber hardware in real-time. A lab PC then executes a recent lab version of the ISS controller flight software. Its output is commanded to the TTM hardware.

Initial trials confirm the validity of the test setup. The controller software can receive centroids from the camera and frame grabber correctly. However, at the time of writing, closed-loop tests could not yet be performed due to a hardware issue. Therefore, neither the full ISS Simulink model nor the control laws designed on its basis can be considered fully validated.

IMAGE STABILIZATION SYSTEM TESTS

Version 1.0

21.07.2021

Status: Interim Release

STU-IAA-M-PRO-1112-01-v1.0_Image-Stabilization-System-Tests_2021-07-21

Image Stabilization System (ISS) "European Stratospheric Balloon Observatory *Design Study*"

Topic: INFRADEV-01-2017 Design Studies

Project Title: European Stratospheric Balloon Observatory *Design Study* – ESBO *DS*

Proposal No: 777516 – ESBO DS

Duration: Mar 1, 2018 - Feb 28, 2021

WP (EU)	WP 11
WBS Item (internal)	620
PBS Item(s)	1112 / 2131
Title	Image Stabilization System Tests
Description	Description and Report on Image Stabilization System Tests
Lead Beneficiary	"IAA"
Nature	"Report"
Dissemination Level	"Public"
Est. Del. Date	-
Version	1.0
Date	
Status	Interim Release
Written by:	Daniel Benitez (Sub-contracted by IAA-CSIC)
Lead Author	Rene Duffard; Angel Colín; José Luis Ortiz
Approved by	

TABLE OF CONTENTS

FIGURE LIST

TABLE LIST

LIST OF ABBREVIATIONS AND DEFINITIONS

Abbreviation	Definition
ESBO	European Stratospheric Balloon Observatory
ISS	Image Stabilization System
FSFW	Flight Software FrameWork
TIP	Telescope Instrumentation Platform
ACS	Attitude Control System
TTM	Tip Tilt Mirror
GCS	General Command Set
IRS	Institute of Space Systems
GCS	General Command Set

REFERENCE DOCUMENTS

1	--
2	

1 INTRODUCTION

This document presents test and part of the integration activities that were performed of the Image Stabilization System developed for the STUDIO balloon telescope prototype at Ingenyo facilities in Spain and facilities of the University of Stuttgart in Germany.

2 OVERVIEW

The main goal of the ISS Subsystem is to compensate maximum disturbances with amplitude of about ±40 arcsec and a frequency of 20 Hz, leaving a residual disturbance below 0.5 arcsec and maintain the image stability for at least 300 seconds. To get this behavior, the STUDIO prototype includes a Tip/Tilt mirror that controls the direction of the guiding star light beam received by the PCO camera image. The Figure 1 shows the light beam path from Tip/Tilt mirror to the PCO visible camera.

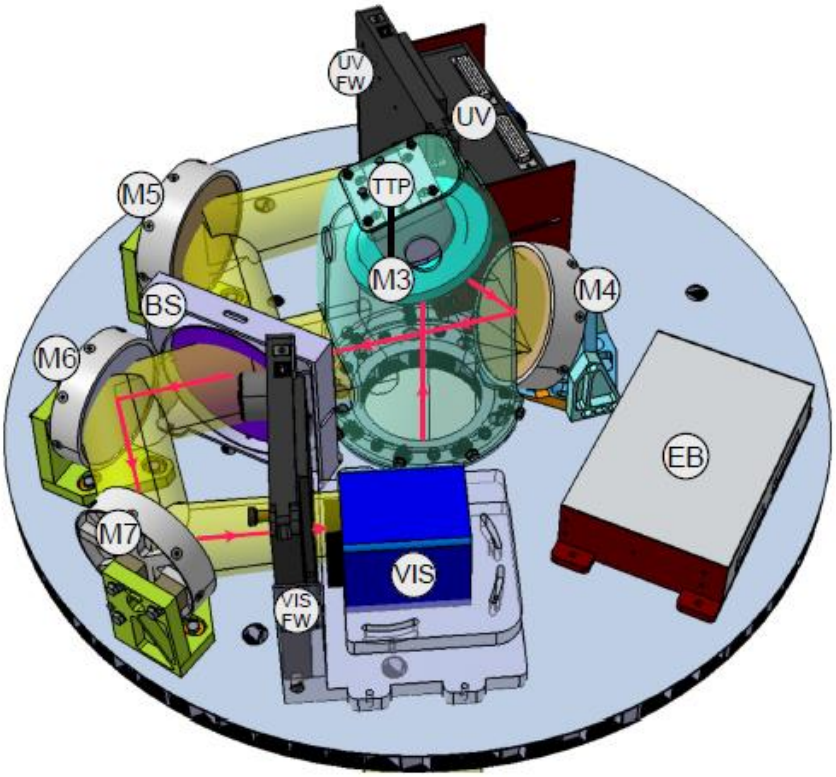

Figure 1: STUDIO Telescope Instrument Platform with the optical beam to visible camera.(M3)–(M7) mirrors, (BS) dichroic beam-splitter, (TTP) tip-tilt platform, (FW) filterwheels, (VIS) camera, (UV) MCP instrument, (EB) instrument electronics box, red arrows: optical path to camera (Image taken from [ROT00])

This document contains the description of tests carried out with the ISS subsystem as part of the STUDIO prototype.

First a general description of the ISS subsystem is introduced, followed by a detailed view of the design and the different approaches to a solution are commented with the related tests and practical results. After that, integrated tests with the on-board framework and a test setup at USTUTT are presented, followed by conclusions of all performed tests and integration activities.

2.1 GENERAL DESCRIPTION OF ISS SUBSYSTEM

The ISS subsystem, highlighted in green in the simplified Telescope Instrument Platform shown in Figure 2, is in charge of stabilizing the image and compensate the high-frequency disturbances that the Attitude Control System (ACS) is not able to handle. Based on that design, the ISS consist in: a Tip Tilt Mirror (TTM) formed by a special 110 mm diameter mirror attached to an S-340 piezo actuator, an E-727 piezo controller, both manufactured by Physik Instrumente, and a visible sCMOS camera. This visible camera (330 nm – 1100 nm) takes images at a rate of 100 fps, transmits them to a frame grabber which identifies the actual location of a guide star in the image using a centroiding algorithm. Based on this location, the ISS control software running on the On Board Computer (OBC) commands the TTM movements in order to compensate any displacement of the guide star on the image due to disturbances.

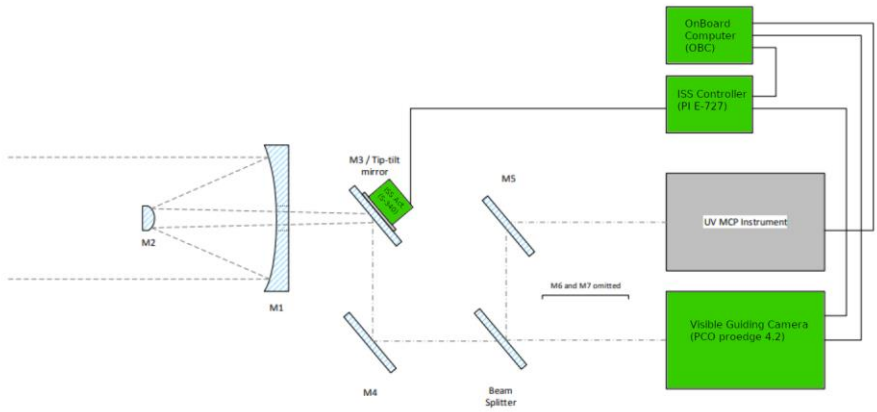

Figure 2: Simple scheme of light optic beam with ISS components highlighted

3 IMAGE STABILIZATION SYSTEM FUNCTIONAL TESTS

The different parts of the Telescope Instrument Platform (TIP) were planned to be developed at the same time. This implies that neither telescope optics nor visible camera were available during the development of the ISS. For that reason a customized test bench with different camera and optics were built for the development and functional validation of the Image Stabilization System functionalities.

With the test bench prepared, it is time for the ISS implementation based on the following steps:

- Tune and incorporation of Physik Instrumente Piezo Controller (E-727) and Piezo Tip/Tilt Platform (S-340).
- Verification of the test bench stability to get the needed resolution for the centroid coordinates in order to be able to compensate the possible displacement due to disturbances and vibrations.
- Development and enforcement of stabilization algorithms based on closed loop control strategies to correct low and slightly high frequencies movements of the centroid.
- Test battery applying different correction factors to the stabilization algorithm.

3.1 IMAGE STABILIZATION SYSTEM TEST BENCH

The test bench used during the developing process of the ISS is based on the following elements:

- Camera ZWO ASI120MM-S with USB 3.0 interface.
- 18/105mm Nikon lens.
- E-727 Physik Instrumente Piezo Controller.
- S-340 Physik Instrumente Tip/Tilt Piezo Platform with a 100 mm diameter mirror fixed on it (Tip/Tilt mirror). The mirror presents its highest sensitivity in the visible wavelength.
- A white LED light set on a holder to simulate the reference object whose centroid must be stabilized.
- Wooden table with vibration dampers on which the camera and the Tip/Tilt piezo platform are installed.
- A motor to generate different kind of simulated disturbances to be compensated by the ISS.
- An Arduino Nano microcontroller to control the switching on and off of the LED light and the movements of the motor in charge of generating the disturbances.

Figure 3 shows the basic configuration used for the test bench.

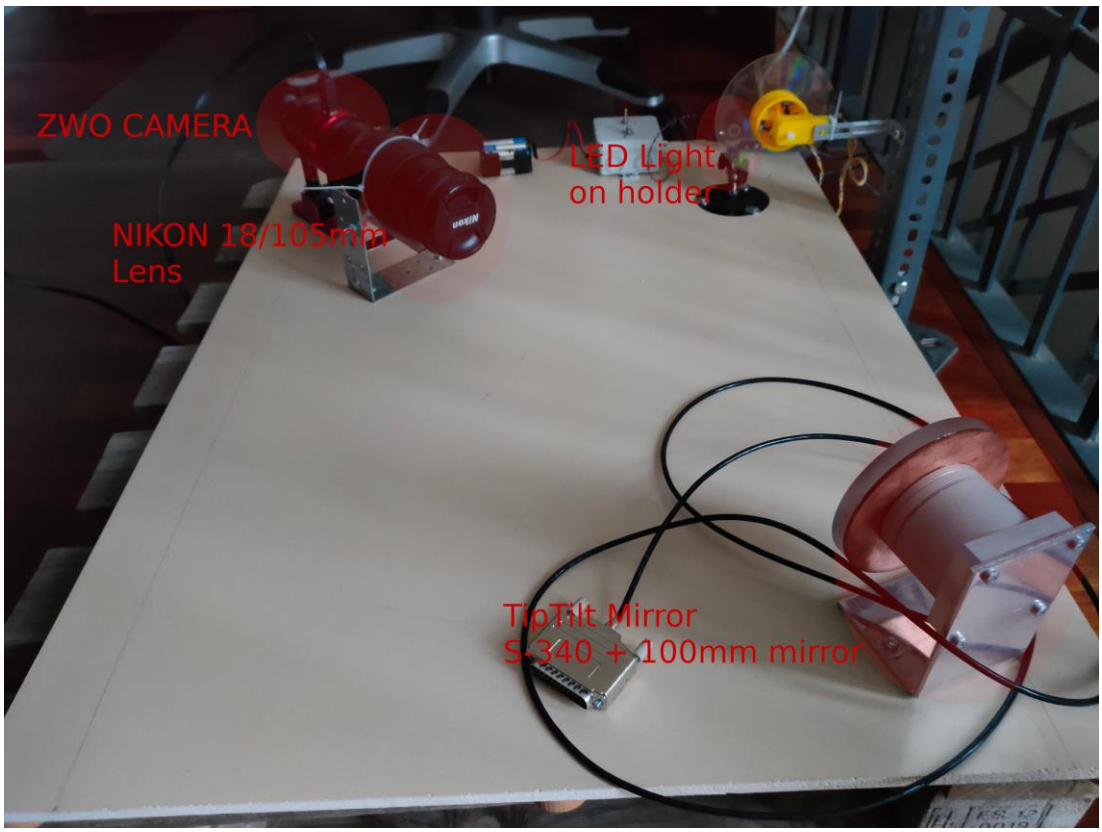

Figure 3: ISS Test bench with ZWO camera + Nikon lens + Tip/Tilt mirror + LED light

Due to the unavailability of a proper optics table and the need to transport the test bench from time to time, the assembly of all the elements was done on a light wooden board with dimmers installed in the bottom side to reduce the possible vibrations generated by external sources.

The LED light and the disturbance simulator motor are controlled using an Arduino Nano microcontroller that receives the proper commands from the computer via a serial port. This way the LED can be switched on and off and the motor moved directly from the computer which expedites the tests and allows doing them remotely.

3.2 TIP/TILT CONTROL HARDWARE PREPARATION: PI PIEZO CONTROLLER E-727 AND PI PIEZO PLATFORM S-340

The ISS is based on a mirror attached to an S-340 Piezo Tip/Tilt Platform [PI02] whose movements are controlled by the Digital Multi-Channel Piezo Controller, E-727 [PI04]. The combination of these two components allows to control the mirror angular displacement with high precision and response time.

3.2.1 S-340 Piezo Tip/Tilt Platform

The S-340, shown in Figure 4, is a high precision 2-axes platform for Tip/Tilt movements based on 4 longitudinal piezo actuators in a differential tetrapod drive architecture, allowing the kinematic independence of both axes of rotation. In other words, the rotation angle in one axis depends exclusively on the differential elongation of the corresponding piezos, minimizing the effects from simultaneous rotation in the other axis. As shown in Figures 5 and 6, the Performance Test Protocol curves, this design allows to get a highly linear response of the S-340 piezo platform, which is essential to get a relation factor between the displacement of the centroid in the image and its corresponding Tip/Tilt platform angular position for the ISS.

Figure 4: PI S-340 piezo Tip/Tilt platform

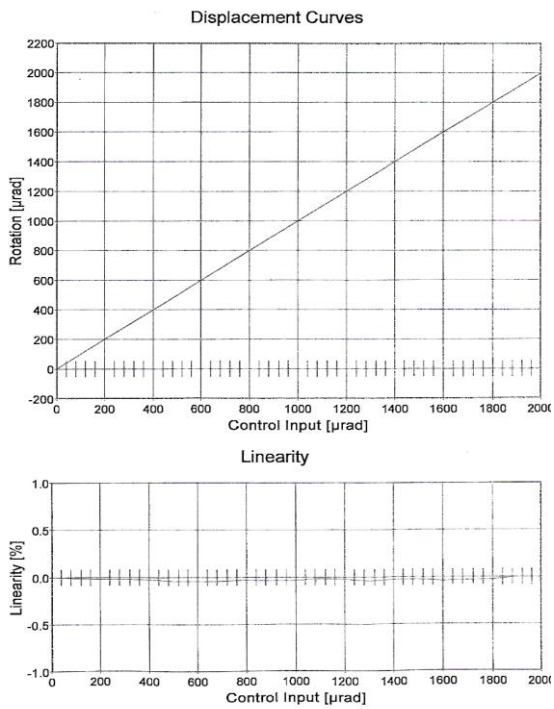

Figure 5: Measurement of Linearity of S-340.ASD piezo platfom RotX Axis

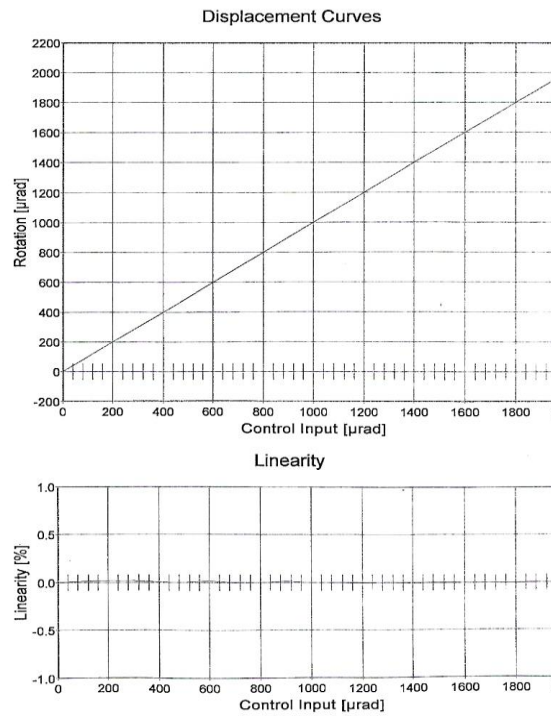

Figure 6: Measurement of Linearity of S-340.ASD piezo platfom RotY Axis

For the ISS subsystem the S-340.XSD version is used, which provides strain gauges for angular position feedback (i.e. an internal closed-loop control of the tip-tilt platform) and Sub-D type connector.

Piezo actuators require high and very precise regulated voltages to operate. Their extension is not a linear function of the applied voltage. To eliminate this and other non-linearities (as hysteresis or temperature dependency) when the Tip/Tilt platform is commanded to a concrete angular position, and facilitate the interaction with it, the E-727 servo piezo controller is used.

3.2.2 E-727 Piezo Controller

The E-727 is a digital controller for piezo-based nanopositioning systems used to handle the angular displacements of the S-340 piezo platform corresponding to the centroid position error. Basically, it receives the axes angular position to be corrected as input (difference between the current and the commanded platform position), and outputs voltages commands to the amplifiers driving the two axes piezo actuator pairs.

This controller implements a complex Proportional-Integral (PI) control algorithm to ensure tracking of angular position commands and two notch filters to avoid the excitation of the piezo platform at resonance frequency. Fortunately, this complexity is abstracted from user through the use of Physik Instrumente manufacturer commands and tools, as described in the tuning process section of this document.

For the ISS subsystem, it was only needed to use a part of all the functionalities and tools available for the E-727 controller, which includes Servo-Controller Dynamic Tuning, installation of PI 3rd party Linux libraries and use of General Command Set (GCS).

3.3 TUNING PROCEDURE FOR TIP/TILT MIRROR BASED ON E-727 CONTROLLER AND S-340 PLATFORM

As any other control motion system, the S-340 Tip/Tilt platform requires a tuning procedure to optimize the response to motion commands for a concrete combination of mirror and environmental conditions. A change in the weight or diameter of the mirror mounted on the S-340 platform requires a new tuning to find the best motion performance.

To facilitate tuning process, Physik Instrumente incorporates a Servo-Controller Dynamic Tuning option in its PiMikroMove software tool offering the possibility to adjust both the notch filters in Open-Loop to compensate undesired resonances in the mechanical system and the servo-control parameters (P-term, I-term) to optimize the dynamic properties (overshoot and settling time). As indicated in the "Servo-Controller Dynamic Tuning" section of the E-727 User Manual, the calculation of the notch filters is based on the Open-Loop frequency response of the Tip/Tilt mirror while the servo-control parameters are adjusted based on step response measurements.

The graphics shown in Figures 7 and 8 correspond to the case of the 100 mm visible dummy mirror used in the test bench during the ISS development phase. As can be deduced from the graphics, the values for the horizontal axis (known as X axis) are around 650 Hz for the notch filter 1 and the step response is quite fast and stable with a P-term of 0.009.

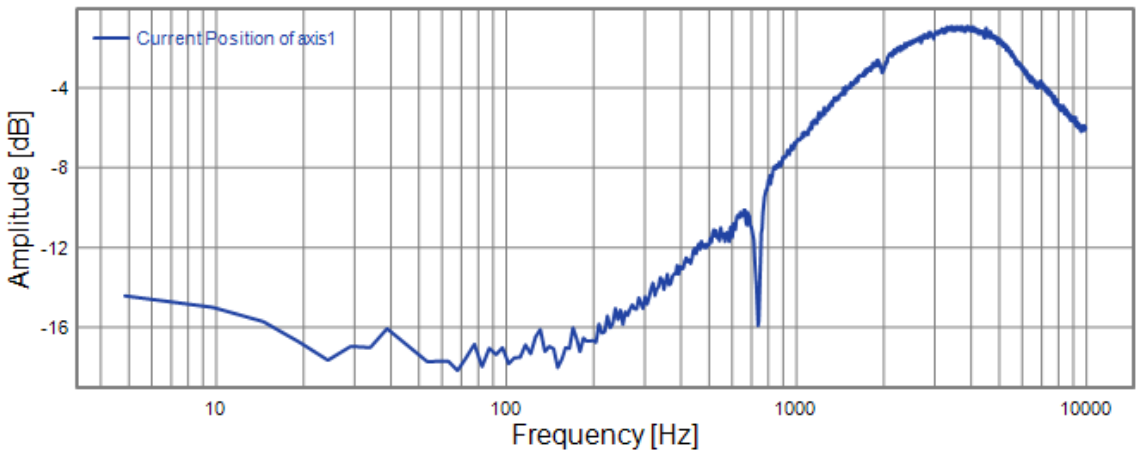

Figure 7: Open-Loop frequency response for 100 mm dummy visible mirror

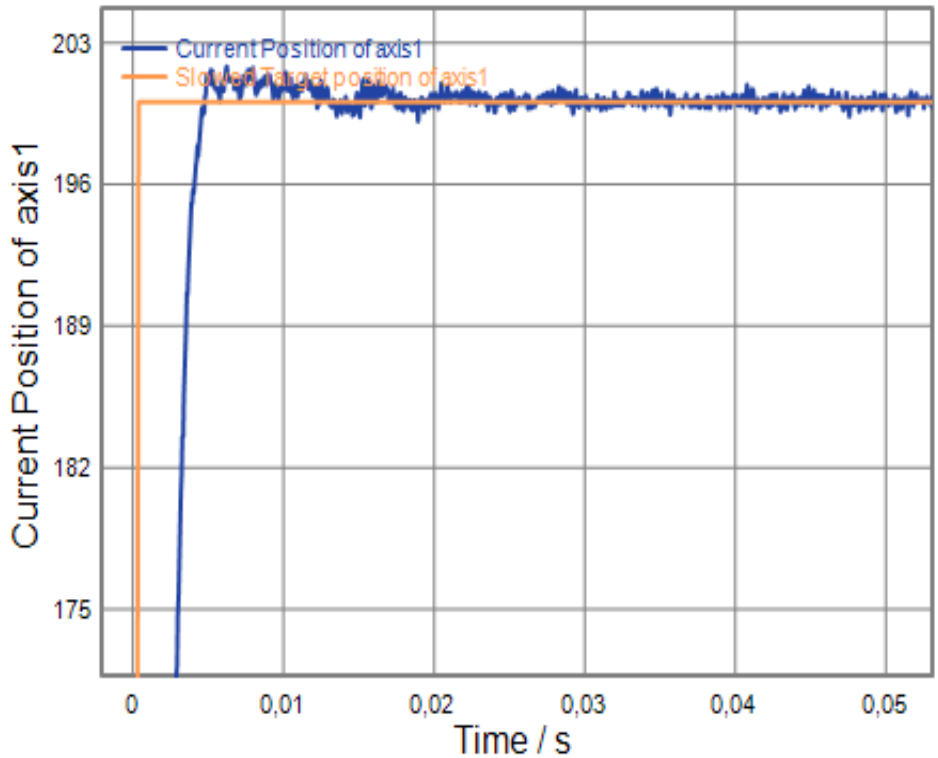

Figure 8: Closed-Loop step response for the X-Axis dummy mirror with a P-Term value of 0.009

3.4 IMAGE STABILIZATION SYSTEM CONTROLLER IMPLEMENTATION

Based on the requirements, the Image Stabilization System must compensate the remaining image jitter up to ±40 arcseconds with disturbance frequencies up to 20 Hz, stabilizing the image on the focal plane to a maximum residual jitter amplitude of 0.5 arcseconds, and maintaining the stability over at least 300 seconds. With this conditions, Thomas Roth have designed and simulated a couple of possible solutions based on closed loop controllers: PI+I and PI+I+Estimator. The implementation of the ISS Controller is based on those solutions detailed on the section 6 of the Master Thesis Work *"Simulation and controller design of a closed-loop image stabilization system for an astronomical ballon platform"* [ROT00].

Although a first order loop controller PID is discarded in the Master Thesis due to the limited response to high frequency disturbances, it have been added to the possible solutions to have a first approximation and provide a reference to compare with.

3.4.1 PID Closed Loop Controller

Proportional-Integral-Derivative (PID) is a control strategy employing feedback to apply an accurate and responsive correction to a control function. The equation 3.1 shows the mathematical form of its overall control function.

$$u(t) = K_p e(t) + K_i \int_0^t e\,(r)dr + T_d \frac{de(t)}{dt} \qquad (3.1)$$

Figure 9 shows a diagram of a basic PID control algorithm including a Proportional (Kc), an Integral (1/Ti) and Derivative (Td) responses. For ISS implementation the PID block parameters would correspond to the following:

- Set Point would be the desired centroid position.
- Process Variable would be the current centroid position.
- Error term would be the difference between the desired and the current centroid position.
- Kc would be the proportional component that provides the ratio of output response to the current Error term.
- 1/Ti would provides the sum of the Error term over the time, increasing over time unless the error is zero, so the effect is to drive the Steady-State centroid position error to zero.
- Td would cause the output to decrease if the current centroid position is increasing rapidly. The derivative response would be proportional to the rate of change of the current centroid position. Although it is implemented in the software Tip/Tilt controller FSFW component, For the ISS the derivative gain will be usually set to zero because it is more sensitive to noise in the process variable signal (current centroid position), amplifies high frequency components and adds complexity to the control system needing an extra filtering of the differentiated signal (PIDF).

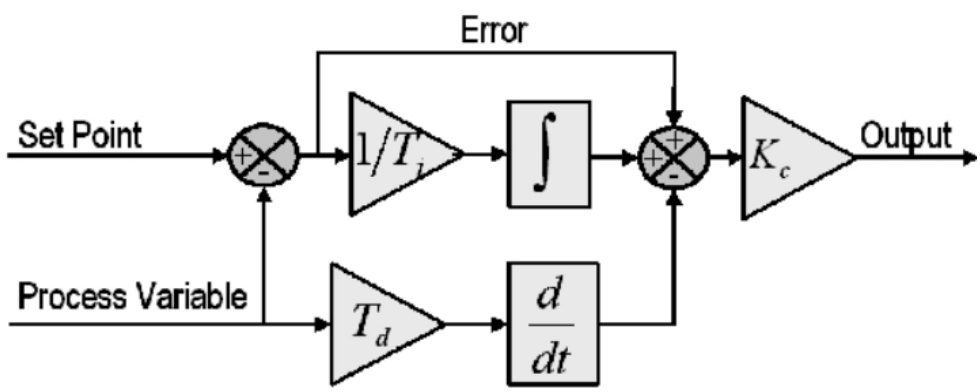

Figure 9: Block diagram of a basic PID control algorithm

In ISS case one PID block is applied to each axis of the Tip/Tilt Piezo Platform giving the opportunity to control them independently in a more flexible and simple way. More details of PID controller systems can be easily found online [NI01][PDH01] or in books like "Modern Control Engineering" written by Katsuhiko Ogata [OGA01].

3.4.2 PI+I Closed Loop Controller

PI+I is a second order controller proposed in the section 6.4 of the Master Thesis Work *"Simulation and controller design of a closed-loop image stabilization system for an*

astronomical balloon platform" [ROT00]. Basically is a PI-controller in series with a second integration stage characterized by the transfer function shown by equation 3.2.

$$G(s) = \frac{1}{s} \cdot \left(k_1 + \frac{1}{s} \cdot k_2\right) \qquad (3.2)$$

with $k_1 = 80$; $k_2 = 800$;

That transfer function is translated into the discrete equation 3.3 that offers the opportunity to implement the PI+I controller as a software function into the FSFW Tip/Tilt controller component.

$$u_k = k_1 \cdot e_k + k_2 \cdot e_{k-1} + k_3 \cdot e_{k-2} + k_4 \cdot u_{k-1} + k_5 \cdot u_{k-2} \qquad (3.3)$$

where,

u_k → Command with number of pixels to correct the centroid position.

e_k → Actual centroid position error (current_centroid – target_centroid).

e_{k-1} → Last centroid position error.

e_{k-2} → Previous centroid position error to last centroid position error.

u_{k-1} → Last command to correct the centroid position.

u_{k-2} → Previous command to last command.

3.4.3 Estimator

Based on the simulations exposed in the section 6.5 of the Master Thesis Work *"Simulation and controller design of a closed-loop image stabilization system for an astronomical balloon platform"* [ROT01], it seems that applying an interpolation of a fixed number *n* of past centroids the future centroids positions can be extrapolated in order to reduce the impact of steep slopes disturbances. The resulting algorithm is a combination of an estimator with a Kalman update equation added to automatically choose the best blend between real measurements and extrapolated estimation.

This algorithm have been implemented as a software function of the FSFW Tip/Tilt controller component to allow the flexible addition of the estimator in order to check if it improves the performance of the PI or PI+I loop controllers.

4 IMAGE STABILIZATION SYSTEM CALIBRATION

The ISS is based on precise angular movements of the piezo Tip/Tilt platform to compensate the possible displacement of the centroid due to environmental disturbances. So a relation between the piezo platform angular position in microradians and the centroid displacement in pixels must be established. Fortunately, as indicated in the Figures 5 and 6, the S-340 piezo Tip/Tilt platform offers high linearity allowing to get a direct relationship between the piezo angular position and the centroid coordinate in the image, as defined in equations 4.1 and 4.2.

$$ttAngularPos_{coordx} = Correlation_{coordx} \cdot centroidDisplacement_{coordx} \quad (4.1)$$

$$ttAngularPos_{coordy} = Correlation_{coordy} \cdot centroidDisplacement_{coordy} \quad (4.2)$$

where,

ttAngularPos → Angular position in microradians to move the piezo Tip/Tilt platform for x and y axes.

Correlation → Correlation factor between the angular position of the piezo platform and its corresponding centroid displacement for x and y axes.

centroidDisplacement → Number of pixels that the centroid has been displaced.

The relation between the centroid coordinate and the Tip/Tilt mirror angular position depends directly on the optics and camera, so the correlation factor should be calculated each time any of these elements changes. For that reason, the following procedure based on a least square method has been implemented, taking advantage of the high linearity of the S-340 piezo platform:

1. A fixed LED light simulating a reference star is mounted on the test bench and the TipTilt platform is moved in all the range of the two axes (in the S-340 platform case the range is 2000 µrad for each axis).
2. Then, the TipTilt platform with the mirror attached is moved over all the range in the two axes and the corresponding centroid coordinate values are stored with the current piezo platform angular position.
3. When the TipTilt platform has been moved over all the range in the two axes, the stored angular positions and centroid coordinates are processed by an approximation algorithm based on a least square method, that return the correlation factor for each axis.
4. The correlation factor is stored in the file system to be used with the current configuration of the system (optics + camera).

Figure 10 shows an example with a graphic of the approximation for X and Y axes using the test bench with the ASI120MM-S camera and the Nikon lens with 105 mm focal length, obtaining as result a correlation factor of 51.07 and -56.50 with a correlation coefficient of 0.99998 and 0.99996, which indicates a high linearity in the relation between centroid coordinate and Tip/Tilt mirror angular position.

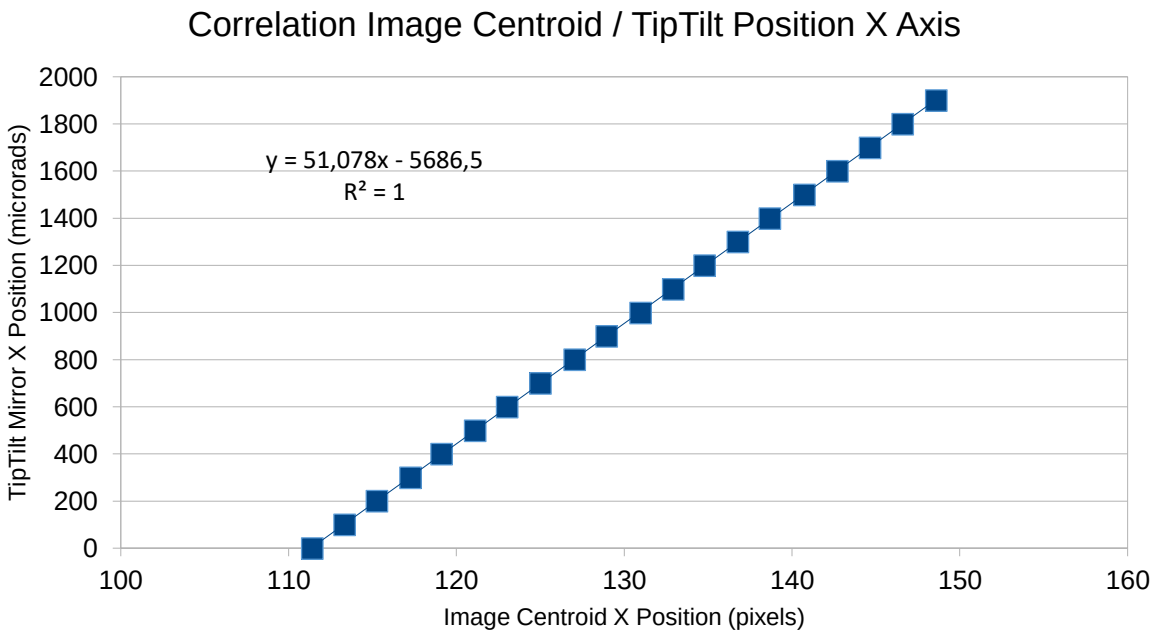

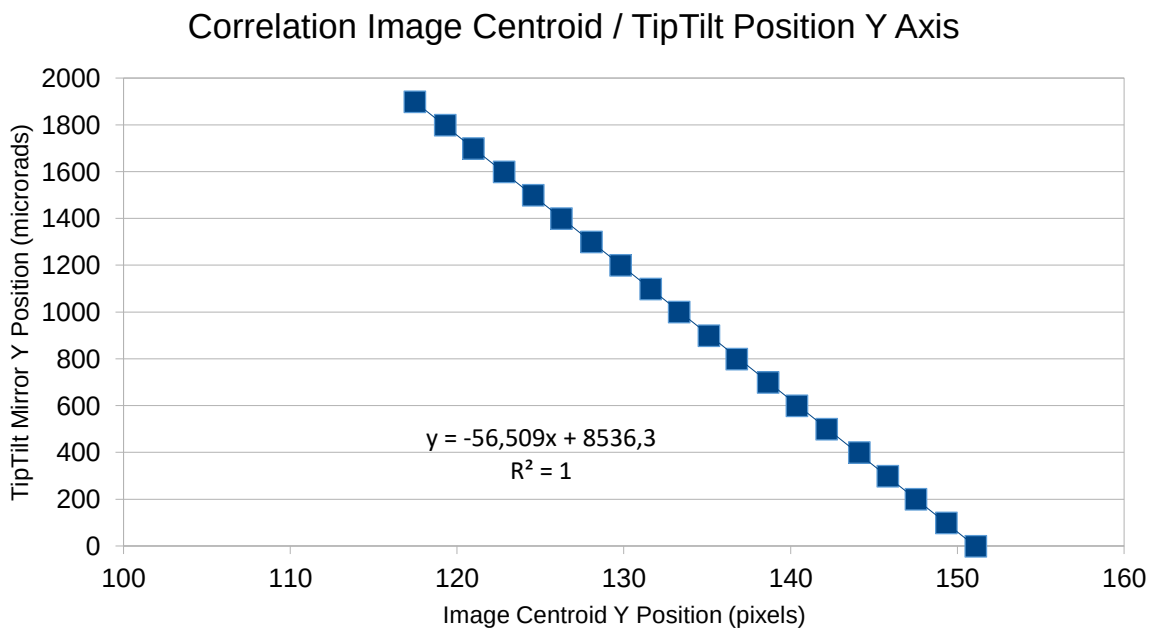

Figure 10: Correlation results between tip/tilt angular position and centroid position on the image plane

5 IMAGE STABILIZATION SYSTEM CONTROLLER TESTS

After the development of the appropriate software algorithms for the Image Stabilization System, a set of tests using the bench described in section 3.1 have been performed to check if the designed ISS meet the expected requirements. These tests include: verification of centroid coordinates calculation algorithm provided by USTUTT, estimation of ISS hardware electronics power consumption and dissipation, Tip/Tilt piezo platform speed response to movement commands and compensation of centroid disturbances using the designed PI and PI+I controller plants.

5.1 VERIFICATION OF CENTROID COORDINATES

To be able to correct the centroid displacement due to environmental disturbances, it is essential to determine the concrete centroid coordinates with high precision. Fortunately, a Matlab algorithm based on the calculation of the intensity weighted center (IWC) was already developed by USTUTT for previous missions, so that algorithm have been translated and adapted to C++ for the ISS case.

To verify the correctness and precision of the centroid coordinates calculation, a bunch of tests have been completed using the assembly described in section 3.1 with a fixed LED light acting as star simulator.

After some problems related to the instability of the surface on which the assembly was placed and the optical lens attachment, a proper configuration to measure the correctness of the centroid coordinates algorithm stability for the tests was achieved. The result of these tests is shown at Figure 11, where the displacement of the centroid using a fixed simulation star was measured during 30 seconds with a difference below 0.1 pixels in both axes.

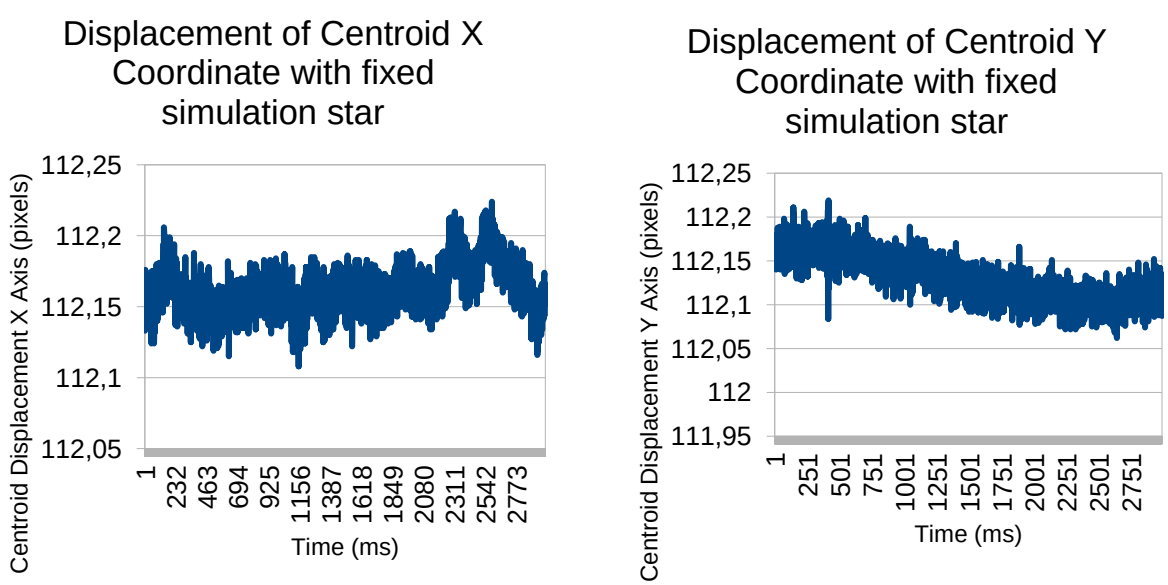

Figure 11: Displacement of Centroid Coordinate with fixed simulation star

Taking into account that the pixel scale for the test bench with the ASI120MM-S camera (pixel size of 3.75µm) and a focal length of 105 mm is around 7.366 arcseconds and that the final system will have much better pixel resolution (see section 4 at Master Thesis Work

"Simulation and controller design of a closed-loop image stabilization system for an astronomical balloon platform" [ROT00]), the obtained accuracy below 0.2 pixels (3σ) confirms that the centroid coordinates calculation algorithm provides enough resolution and correctness for the ISS requirements.

5.2 ESTIMATION OF POWER CONSUMPTION AND DISSIPATION

The PI E-727 piezo controller and the S-340 Piezo Platform must be installed as part of the Telescope Instrumentation Platform (TIP). During the flight of the stratospheric balloon, the TIP must have the most stable environmental conditions and must provide the required power energy to the electronics parts. This energy is provided using batteries, so a high precision calculation of the power consumption is required to size the batteries adequately.

For the ISS case, the PI E-727 piezo controller is the main element that consumes power to control the S-340 piezo platform movements, so the following experimental procedure of measuring its power consumption were carried out:

- A special power cord for the E-727 was built to allow the insertion of a multimeter to measure the amperage flowing through the E-727 controller.
- The E-727 was powered on, measuring and writing down the amperage during the initialization process of the E-727 controller.
- The S-340 piezo platform was commanded to move in all the range of the two axes, from 0 to 2000 microradians, writing down the amperage measured by the multimeter.

Table 1 shows the obtained measurements, taking into account that the E-727 power adapter provides a voltage of 48 Vdc. From the table it can be deduced that the E-727 goes through three stages during initialization, just after power up, and consumes from 23 to 31.8 watts depending on the angular position of each axis of the S-340 piezo platform.

S-340 X Axis Angular Pos. (µrad)	**S-340 Y Axis Angular Pos. (µrad)**	**PI E-727 Power Consumption (W)**	**PI E-727 DC Current (A)**
0	0	31.8	1.146
500	0	30.4	1.082
500	500	29.2	1.016
1000	500	27.8	0.97
1000	1000	26.6	0.923
1500	1000	25.8	0.888
1500	1500	24.6	0.852
2000	1500	23.7	0.827
2000	2000	23	0.8
Average Power Comsumption for PI E-727 with S-340 Piezo (W)		26.9888888888889	

Average DC Current while S-340 TipTilt Platform operating (A)	0.95
Peak DC Current at first stage of PI E-727 Power UP (A)	0.7-0.8
Peak DC Current at second stage of PI E-727 Power UP (A)	0.3-0.4
Peak DC Current at third and final stage of PI E-727 Power UP (A)	0.8-1.14

Table 1: E-727 controller power consumption during initialization and range positions

5.3 TIP/TILT PIEZO PLATFORM SPEED RESPONSE TO MOVEMENT COMMANDS

To interact with the TTM, the FSFW based software running on the OBC must implement a direct USB communication with the E-727 controller, which is in charge of applying the appropriate voltages to the piezo actuators of the S-340 Tip/Tilt platform to get the requested movement. To implement this communication, Physik Instrumente manufacturer provides what is known as General Command Set (GCS) [PI05], a standard command set, independent of specific hardware (controller or attached stages) and well-suited for positioning tasks with one or more axes. This GCS is implemented as a software library to be used directly by computers with Linux operating system [PI01].

The core of design of the ISS is based on the capacity of the TTM to be moved at high velocity to compensate the high frequency disturbances (10-20Hz). After the tuning procedure done with the PIMikroMove software tool, the set composed by the S-340 piezo actuator and the E-727 controller takes between 2 and 3 ms to move and stabilize an angular position of 250 µrad and about 7-8 ms to move from 0 to 2000 µrad (See). This should be enough for the requirements of the ISS, but the software library could add some delay to the execution of the commands. To evaluate this possible delay, some time measurements were done using the Linux GCS library and the C++ time manipulator chrono library, with the results shown in the Figure 12 and 13.

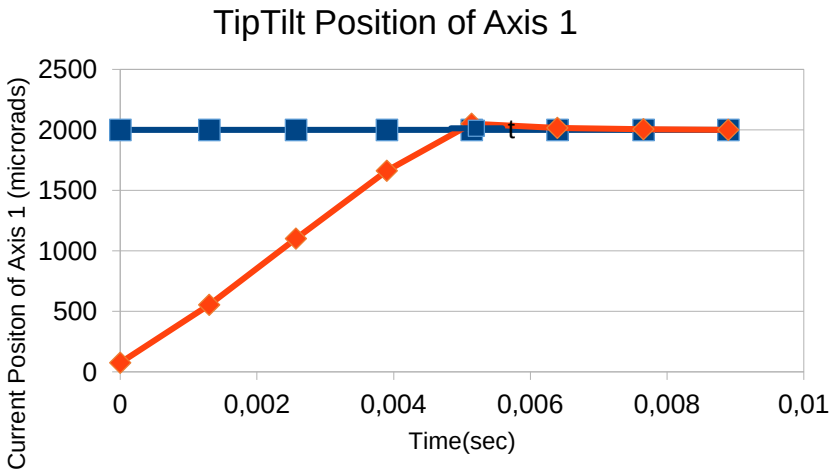

Figure 12: Measured time for Tip/Tilt movement from 0 to 2000 rad using Linux GCS and chrono libraries

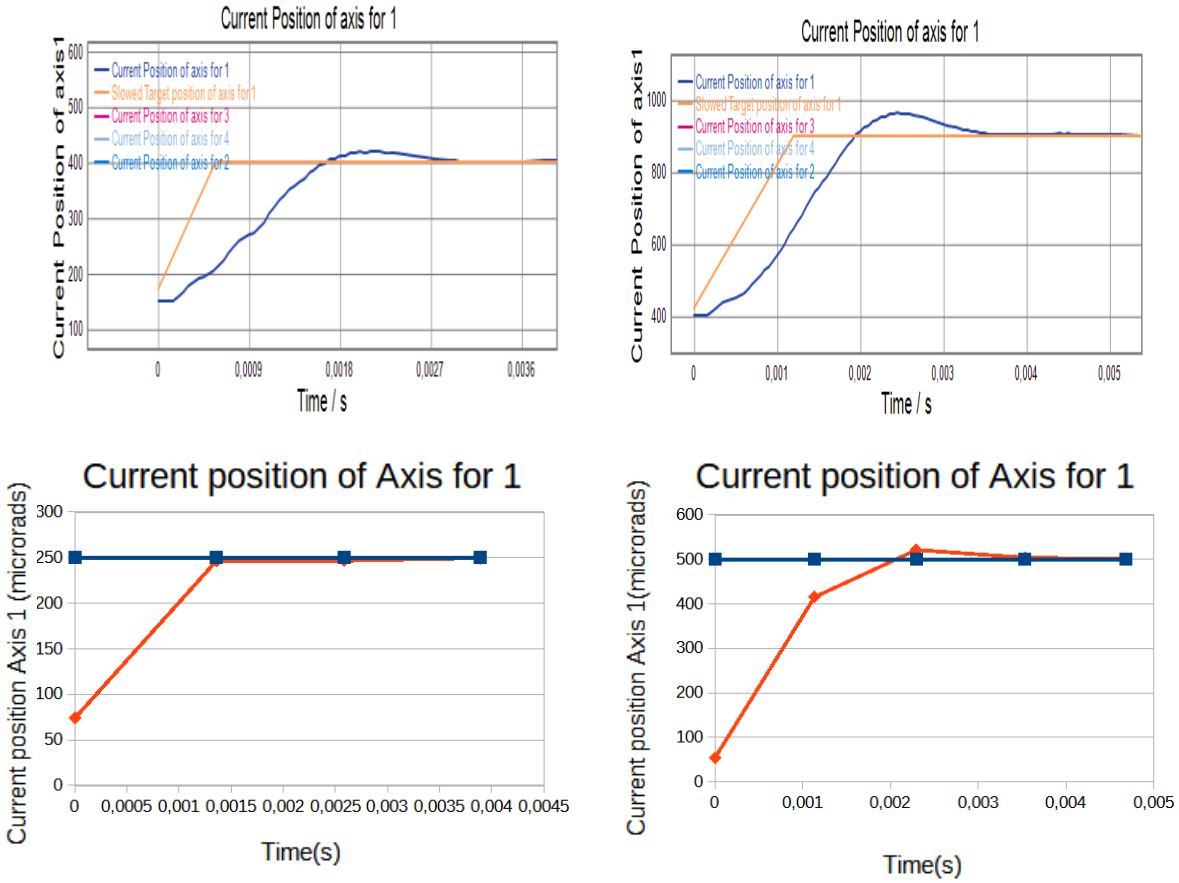

Figure 13: Measured time for Tip/Tilt movement from 0 to 2000 rad using Linux GCS and chrono libraries

After measuring the time required to move the TTM from one position to another using the Linux GCS library and compare them with the same displacement using the PiMikroMove tool, it can be assumed that the Linux GCS library and the PiMkroMove behave in a similar way.

5.4 CENTROID STABILIZATION AND COMPENSATION OF DISTURBANCES TEST

After developing the ISS controller software algorithms introduced in section **Fehler! Verweisquelle konnte nicht gefunden werden.**, the next step consists basically in proving the suitability of these stabilization algorithms using the physical test bench.

To emulate the disturbances, the LED light simulating the reference object is attached to a micro stepper motor and placed on a metal arm besides the test bench, avoiding the possible transmission of vibrations from the motor to the test bench. This motor is controlled by a microcontroller with a customized firmware in charge of moving the LED with different patterns and frequencies.

Based on that combination of test bench and flexible star simulator disturbances generator, a series of tests for the PI and PI+I controllers have been carried out.

5.4.1 PI closed-loop controller test

The PI closed-loop controller algorithm have been tested simulating two types of disturbances: manually generated disturbance and fixed 1 Hz and 20 Hz frequency disturbances generated by the micro stepper motor.

Manual generated disturbance

The manually generated disturbance test is aimed to verify that the PI closed-loop is able to move the TipTilt mirror and counteract punctual short range disturbances. These disturbances are generated by manually knocking the LED light simulation star base.

Figure 14 shows the result of generating two vibrations of the simulation start generated by hitting its base two times in ten seconds. Those vibrations are instantly compensated by the Tip/Tilt mirror angular movements, so the PI closed-loop controller design fits the requirements to compensate punctual short range disturbances.

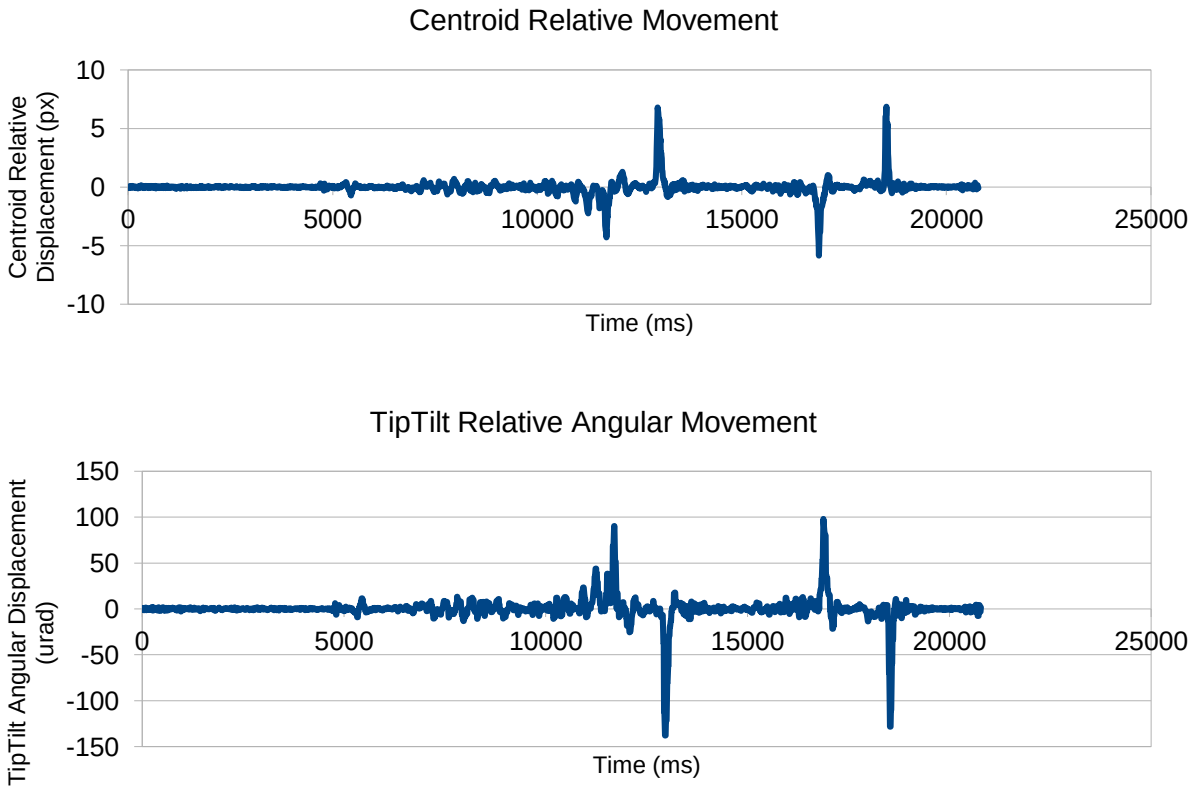

Figure 14: Correction of manual disturbance knocking simulation star base

1 Hz frequency disturbance

In order to know how the PI closed-loop controller responds to low frequency disturbances, a 1 Hz disturbance was generated moving the micro stepper motor with the LED light attached. Figure 15 shows the comparison between the uncorrected and corrected centroid position when applying a 1 Hz square disturbance. It is evident that the PI closed-loop controller amends the centroid displacement due to the simulated disturbance, but it presents some difficulties to correct large changes in the disturbances. This behavior seems to be related to some high frequency components of the square signals, but the disturbances during the balloon flight are not expected to have that kind of behavior. So in principle the PI closed-loop controller should be appropriate to handle low frequencies disturbances.

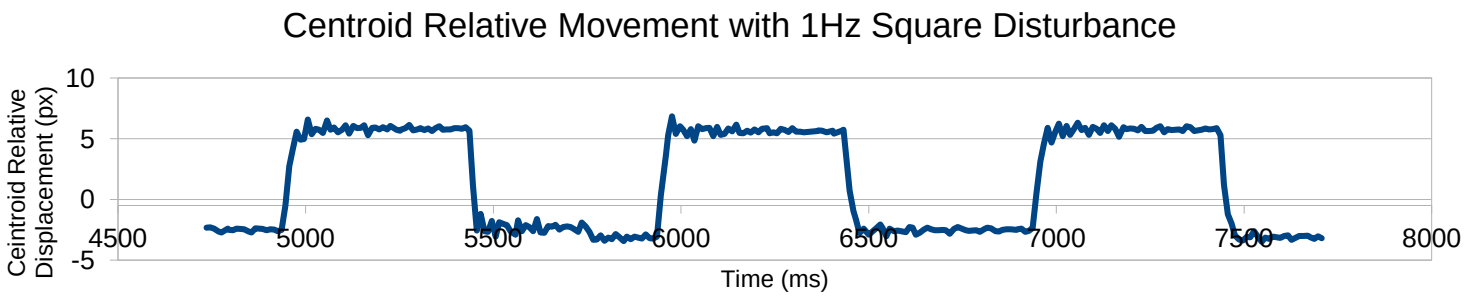

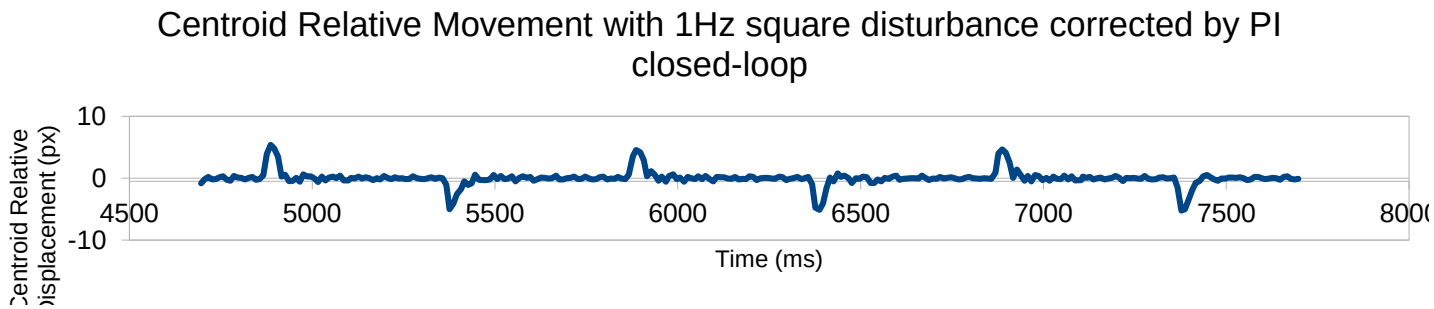

Figure 15: Comparison between uncorrected 1Hz square disturbance and corrected by PI controller

<u>20 Hz frequency disturbance</u>

Although the Master Thesis Work *"Simulation and controller design of a closed-loop image stabilization system for an astronomical balloon platform"* concludes that the majority of the expected disturbances are low-frequency oscillations (below 10 Hz), the initial requirements included compensation of disturbances up to 20 Hz. For that reason that kind of disturbance have been generated using the micro stepper motor with the pattern shown at upper graphic in Figure16.

The lower graphic in Figure 16 shows the result of trying to compensate that disturbance with the PI closed-loop controller. From that graphic it can be concluded that the PI closed-loop controller takes the centroid around the center (zero point) but it is incapable of reducing the centroid deviation. In the concrete case shown in the Figure 16, the calculated standard deviation of the uncorrected 20 Hz disturbance gave a value of 2.39 pixels while in the corrected one this value increased to 3.01.

Based on these results it can be concluded that the PI controller has a good performance for low-frequency disturbances (1 Hz to 5 Hz) but it is insufficient to compensate high-frequency disturbances.

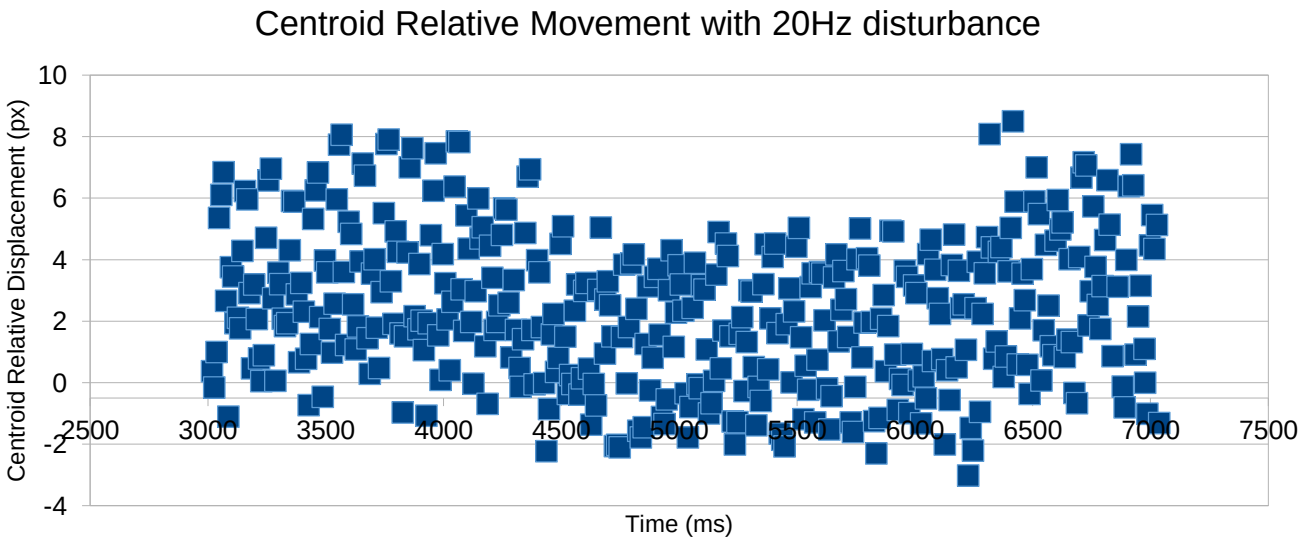

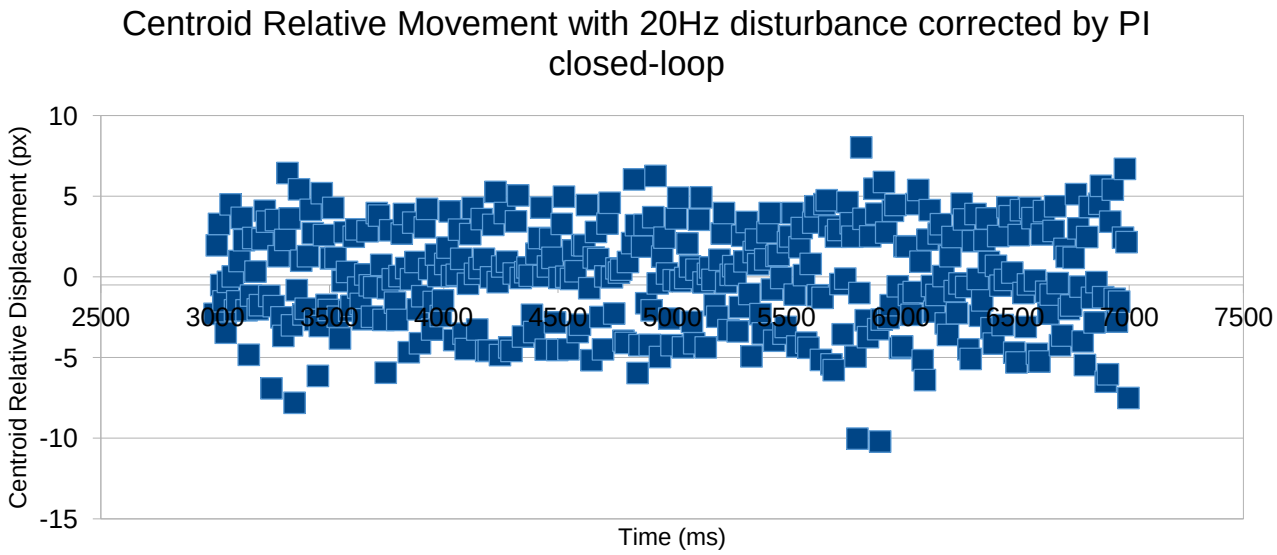

Figure 16: Comparison between uncorrected 20Hz disturbance and corrected by PI controller

5.4.2 PI+I loop controller test

After basic PI correction test, the approach for the PI+I type controller explained in section 3.5.2 have been tested.

<u>Synthetic disturbance generator</u>

In order to have a more precise control of the disturbances applied to the system and reduce the differences between the behavior of the test bench and the final system, a synthetic disturbances generator has been implemented. The simulation of the disturbances has been done adding the simulated disturbance value to the centroid position obtained by the system.

This way it is possible to close the loop and check the performance of the controller with the current configuration.

The synthetic disturbances generator uses known disturbances that are injected to the centroid position from a previously created file. The following disturbances files has been created:

- A set of single-frequency disturbance files, with frequencies between 1 and 20 Hz.
- A disturbance file with disturbance values measured as in-flight data in the BRRISON project, a stratospheric balloon that has a similar gondola to the STUDIO one.

Although disturbances applied by the synthetic disturbances generator are more similar to those of the final system, contributions from test bench disturbances are not negligible.

Once the synthetic disturbances generator has been implemented, BRRISON project disturbances have been injected to the system centroid position and a value sweep in the parameters of the PI+I controller was performed to find their optimal working values. In order to facilitate the sweep, two groups of parameters were defined in the PI+I equation described in (3.3): parameters related to previous error values (k_1, k_2, k_3), and parameters related to previous commands (k_4, k_5). It has been respected the proportional relationship between parameter in the same group disposed in the Master Thesis Work "Simulation and controller design of a closed-loop image stabilization system for an astronomical balloon platform".

The values calculated by Thomas Roth in his Master Thesis are:

k_1=0.0402; k_2=0.0004; k_3=-0.0398; k_4=2; k_5=-1

The final equation applied to the test controller is:

$$u_k = K_{error} \cdot (0{,}0402 \cdot e_k + 0{,}0004 \cdot e_{k-1} - 0.0398 \cdot e_{k-2}) + K_{command} \cdot (2 \cdot u_{k-1} - u_{k-2}) \qquad (5.1)$$

The assessment of the results was done with the standard deviation of the centroid position. After a bunch of tests the optimal values found for the proportional parameters are:

K_{error} = 19; $K_{command}$ = 40;

5.4.3 Estimator test

A first implementation of the estimator was done without success in the test bench. Whenever the estimator was applied, the correction commands diverged in a small number of steps. After some clarifications with Thomas Roth about his implementation in his Master thesis "Simulation and controller design of a closed-loop image stabilization system for an astronomical balloon platform", the estimator was implemented again adjusting the order of the polynomial estimation to one, what means linear estimator, and establishing the behavior of the estimator under unexpected circumstances. The number of extrapolated centroid without a new valid centroid has been limited by a configurable parameter.

The new estimator solution was implemented after the initial test bench described at section 3.1 was dismounted. It cannot be tested until the control loop is closed again. But the estimated centroid positions in simulated series of applied disturbances are coherent with the actual values obtained measuring the centroid.

6 CONCLUSIONS ON IMAGE STABILIZATION SYSTEM DESIGN

After testing PI and PI+I controller algorithms for the ISS, it seems that the PI closed-loop controller has a better performance correcting low-frequency disturbances while PI+I is able to handle high-frequency disturbances up to TBD (Ignacio results).

Otherwise, the estimator proposed in Thomas Roth Master Thesis has obtained inconclusive results in the experiments carried out with the test bench, but it could be due to the limited stability and environmental conditions, so exhaustive tests are recommended in a more controlled environment.

As each controller algorithm seems to work better than the other in concrete conditions and there is no conclusive result of the convenience of using the Estimator, it have been decided to grant the maximum flexibility to the ISS subsystem control by implementing in the FSFW the possibility of selecting one of the two controller algorithms (Pi or PI+I) and if the Estimator is active or not.

7 IMAGE STABILIZATION SYSTEM FSFW INTEGRATION

Once the ISS control software algorithms have been defined, developed and tested, the next step was to implement them into the software suite in charge of communicating with external devices, perform control loops, receive telecommands and send telemetry between the different STUDIO project subsystems. For this task, the Institute of Space Systems, hereinafter IRS (USTUTT), have developed its own Flight Software Framework (FSFW).

For the integration of ISS subsystem into the FSFW two different software components have been developed following the philosophy established by the framework: TipTilt Handler Device and TipTilt Controller.

8 INTEGRATION AND TESTS OF IMAGE STABILIZATION SYSTEM INTO IRS OPTICAL BENCH

After designing and integrate the ISS software components into the FSFW, the next step has consisted of doing stabilization tests with a system formed by the elements shown at Figure 16, including: PCO Visible Camera, Tip/Tilt 110 mm mirror mounted on S-340 Piezo Platform, a second 100 mm mirror attached to another S-340 Piezo Platform to simulate disturbances and a laser providing the reference star.

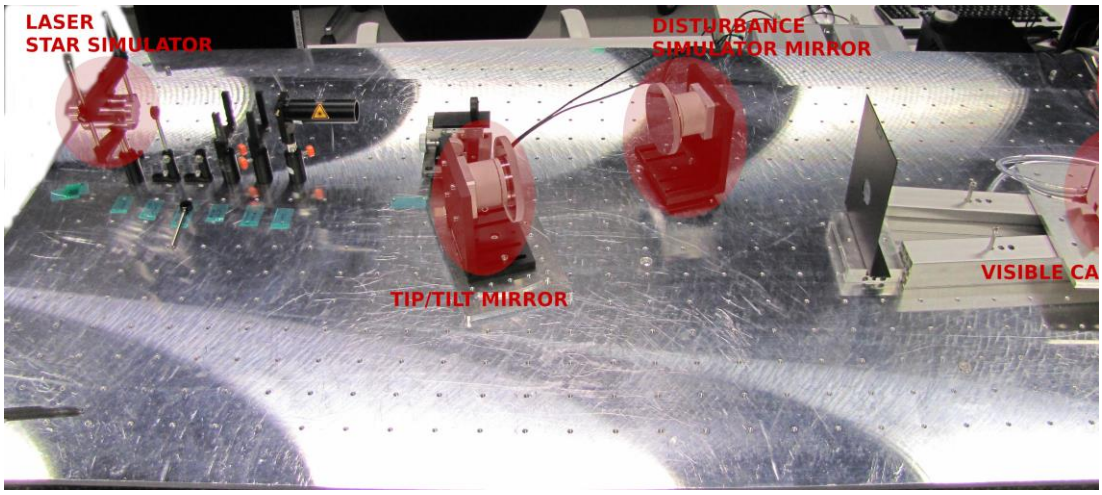

Figure 16: Test bench in optical laboratory at IRS facilities

8.1 INITIAL PLAN AND TEST OBJECTIVES

8.1.1 Test Objectives

Acceptance Test:

- Verify the general functionality of the Image Stabilization System
- Verify the performance requirement for the Image Stabilization System
- Verify the robustness of the Image Stabilization System

System Characterization:

- Characterize the system with regard to several aspects (*details see below*)

8.1.2 Detailed Test Items

<u>Acceptance Test</u>

- Verify the general functionality of the Image Stabilization System
  - Software
    - Housekeeping data provision
      - Incl. saving of tip/tilt platform positions
    - 3 commands (setting modes, changing parameters, action commands)
    - Event generation / raising
  - Hardware setup
    - Connect camera + TTP controller to PCDU
- Verify the performance requirement for the Image Stabilization System

    - 0.5 arcsec peak-to-peak at reference disturbance over at least 300 s
    - Use at least two of the "segments" of the pointing data for the tests (within +/- 40 arcsec)
    - Full test run over at least 2 h
- Verify the robustness of the Image Stabilization System (against the following irregularities)
    - Segments with (short) disturbances > +/- 40 arcsec, but still within range of camera (i.e. e.g. +40" +/- 50" for a 512 px subframe)
    - "Missing" centroids, simulated by short manual obstructions of laser beam (+ "regular" disturbance set on 2nd TTP)

<u>System Characterization Test</u>

- Assessment of performance of different control laws (PI+I, PID, with/without estimator)
    - Using the available "segments"
    - Daniel & Ignacio to figure out how to tune the controllers
- Sensitivity to centroid quality
    - Different brightness targets (9 mag target = baseline)
- Frequency sweeps (different amplitudes)
- Different camera exposures times

8.1.3 Test Setup

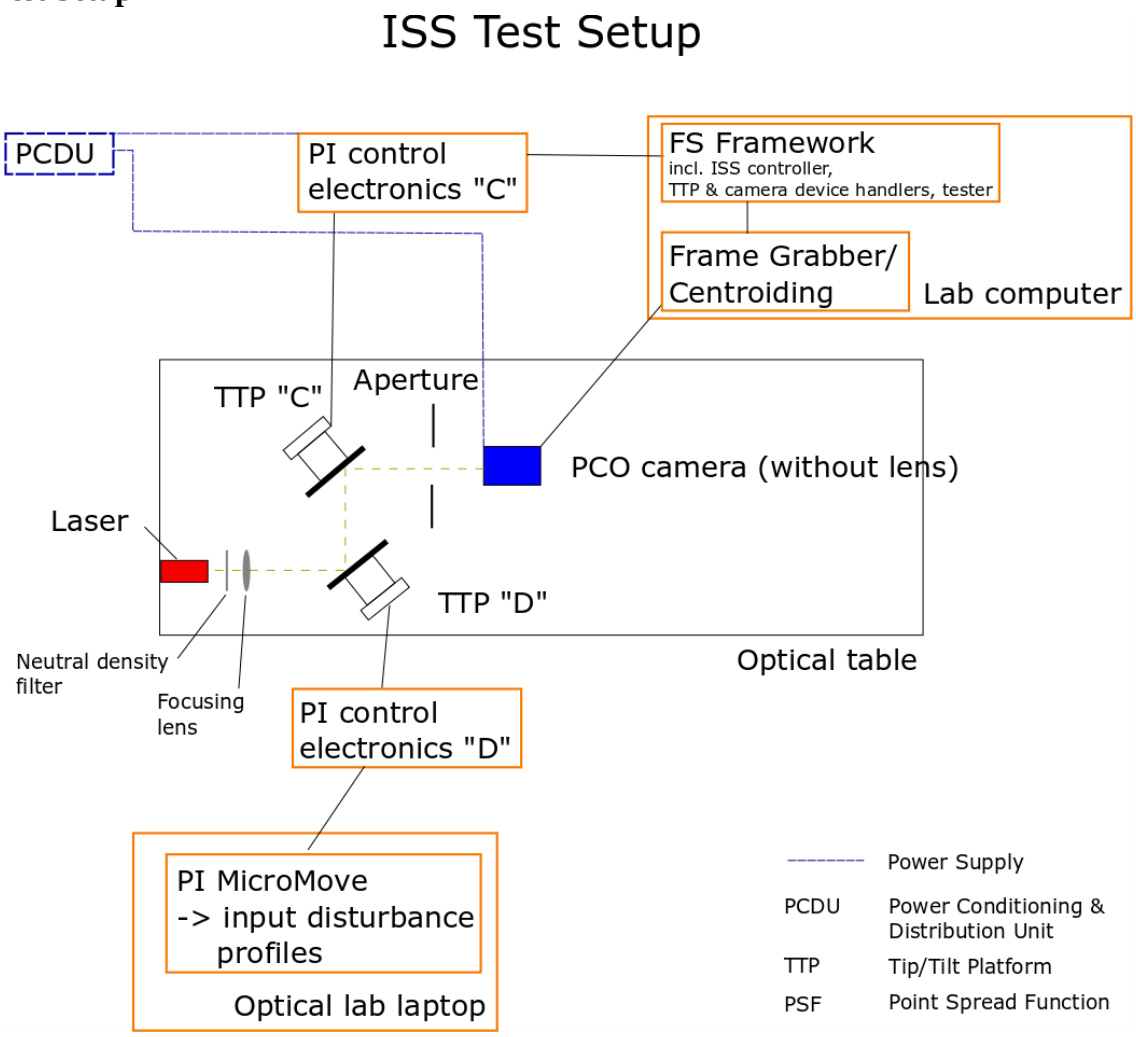

General approach:

- Red laser (635 nm) acts as target. Laser beam is attenuated by (exchangeable) neutral density filters to roughly match expected target star brightness under flight conditions. Attenuated laser beam is furthermore focused by a lens (focal length 1500 mm) onto the camera chip. Laser is still.
- Tip/Tilt platform (TTP) “D” is used to generate disturbances based on expected remaining gondola/telescope jitter
- Image Stabilization System (ISS) is used in closed loop (TTP “C” + PCO camera, controlled via software framework) to correct the disturbances

8.2 WORK LOG DURING INTEGRATION WEEK

This section is dedicated to describe all the tasks carried out during the four days of work at IRS facilities related to the ISS integration:

- Preparation of components related to the ISS software integrated into the FSFW for the reading of centroid information provided by the PCO camera through datapool variables.

- Add events generated by the ISS software controller to inform the Ground Station about any anomaly, such as:
  - Event to inform that the target centroid position requires a TipTilt mirror angular position out of the 0-2000 µrad range of the S-340 piezo platform. After generating the event, the platform remains in the extreme position closest to the target centroid location.
  - Event related to incidents detected in the Tip/Tilt hardware controller, PI E-727, returning as parameter of the event the error code generated by the PI E-727 control libraries. Then this error code can be easily identified by Ground Station searching in the error list provided by the PI E-727 user manual.
  - Event relative to reaching the limit number of iterations of the estimator with an invalid centroid.
- Detection and correction of an incompatibility for the 2018 (used during development) and 2020 (libraries included in the new Physiks Instrumente driver acquired by IRS). That incompatibility is related to the need to specify a parameter with the number of axes in the library function in charge of detecting if the axes are moving or not.
- Correction of incident related to the delay in sending commands from the TipTiltComIF to the E-727 Piezo Controller. The problem was related to an unexpected overload of the Computer Processing Unit (CPU), which slowed down the execution of the software within the Framework. After migrating the ISS software to a Framework clean branch, this incident was solved, reducing the processing time of the commands form about 200ms to 4ms.
- Modification of ISS software components to be able to use simulated centroid coordinates taken from a file instead of being provided by the PCO camera datapool variables. This modification was necessary due to problems with the PCO camera libraries during the compilation process, which could not be solved during the four day stay at IRS facilities.
- Open loop integration test on the optical bench located in the clean room of the IRS facility. As the centroid data could not be provided by the camera, the ISS did not have the enough information to close the control loop. However, in absence of performing these closed-loop tests, a calibration and a stabilization procedures were performed using data provided by files with simulated centroid coordinates, with good results.

8.3 IMAGE STABILIZATION SYSTEM INTEGRATION FINAL RESULTS

After four days of work at IRS facilities, located at the University of Stuttgart, it can be concluded that the following tasks of the planned tests have been successfully performed:

- Physically integrate the ISS subsystem, formed by the mirror mounted on an S-340 Tip/Tilt Piezo Platform and PI E-727 Piezo Controller, into the IRS optical bench.
- Solve the problems of delays related to sending commands and obtaining responses between the FSFW and the E-727 Piezo Controller, reducing the delay from 200 ms to less than 4 ms.
- Carry out tests in calibration and stabilization modes from inside ISS software controller component.

- Inclusion of the following data exchange (datapool variables) to get the centroid information from the Visible Camera Device handler:
  - Centroid_PoolId → Datapool variable with the two centroid coordinates (X and Y axes) provided by the visible camera.
  - CentroidTime_PoolId → Datapool variable consisting of two 32-bit unsigned integers with the number of seconds and microseconds when the centroid was calculated in Unix time format.
  - TargetCentroid_PoolId → Datapool variable with the centroid coordinates to be used as reference during the stabilization procedure.
- Generation of the following events to be sent to Ground Station:
  - Event TIPTILT_CALIBRATION_NO_CENTROID sent when the visible camera and framegrabber handler indicates that the centroid provided to the ISS TipTilt Controller is not valid and must be ignored when making the correction in the ISS.
  - Event TIPTILT_ESTIMATOR_LIMIT_REACHED sent when the estimator is active together with the closed-loop control strategies (Pid or PI+I) and the limit of points established in the estimator is reached. In this case, the prediction made by the estimator is not applied anymore to avoid that the system diverges after several iterations with invalid centroids.
  - Event TIPTILT_PLATFORM_OUT_OF_RANGE sent when a limit position is reached in the range of the Tip/Tilt piezo platform. In the case of using S-340 piezo platform, these limit positions correspond to 0 and 2000µrad.
- CALIBRATION and STABILIZATION submodes real tests on the clean room test bench at IRS facilities. Taking into account that the Visible camera could not be used in the tests, simulated centroids were loaded from an external file.

The other planned tests require the centroid coordinates to apply corrections through the ISS closed-loop controllers. Due to an unexpected problem with the installation of its software libraries the PCO camera could not be integrated into the optical lab test bench and the control loop could not be closed, so it was not possible to carry out the rest of planned tests.

9 CONCLUSIONS

Based on the controller design in [ROT00], a PI+I closed-loop controller algorithm and an optional Estimator filter were developed. A basic PID closed-loop controller was also integrated. Due to the limited stability of the initial test bench surface, it could not be determined the best choice for the closed-loop control algorithms. Both algorithms were tested on the bench described at section 3.1 with good results for the PI controller at low frequency disturbances and better results for PI+I controller at higher frequency disturbances. As PI closed-loop controller performed better for low frequency disturbances on the initial test bench, it was decided to grant more flexibility by adding the ability to select one of two closed-loop controllers, PI and PI+I. This way it is possible to carry out different test scenarios with different configurations and find the best approach for the closed-loop controller parameters.

STUDIO software suite is based on the IRS FSFW framework, so the developed closed-loop algorithms were integrated into FSFW as TipTilt Device and TipTilt Controller customized components. Both software components were properly tested without interaction with Visible Camera and Ground Station. Unfortunately, the Visible Camera and Framegrabber set experienced a serious problem with the software libraries, so no closed-loop test could be done.

Once the problem with the Visible Camera and Framegrabber set is solved, the remaining tests from the integration time at Stuttgart (refer to section 8) should be done to verify the suitability of the closed-loop controllers, check the correct interaction of ISS software components with Visible Camera Device and Ground Station and debug possible errors. Taking advantage of the flexibility granted by the availability of two, PI and PI+I, closed-loop controllers with custom parameters, different tests with different closed-loop control parameters are recommended to determine the best option for IRS test bench case (refer to Figure 16).

BIBLIOGRAPHY

[PI02]: Physiks Instrumente (PI) GmbH & Co. KG, Piezo tip/tilt platform S-340, 2021, [Online]. Available: https://static.physikinstrumente.com/fileadmin/user_upload/physik_instrumente/files/datasheets/S-340-Datasheet.pdf

[PI04]: Physiks Instrumente (PI) GmbH & Co. KG, Digital multi-channelpiezo controller E-727.x, E-727.xAP, 2021, [Online]. Available: https://static.physikinstrumente.com/fileadmin/user_upload/physik_instrumente/files/datasheets/E-727.xAP-Datasheet.pdf

[PI03]: Physiks Instrumente (PI) GmbH & Co. KG, E-727 digital multi-channel piezo controller, 2021

[ROT00]: Thomas Roth, Simulation and Controller Design of aClosed-Loop Image Stabilization System for anAstronomical Balloon Platform, 2021

[NI01]: National Instruments, PID Theory Explained, 2021, [Online]. Available: https://www.ni.com/es-es/innovations/white-papers/06/pid-theory-explained.html

[PDH01]: Anthony K., Fundamental of PID Control, 2021, [Online]. Available: https://pdhonline.com/courses/e331/e331content.pdf

[OGA01]: Katsuhiko Ogata, Modern Control Engineering, 1997

[PI05]: Physiks Instrumente (PI) GmbH & Co. KG, PZ281E GCS Commands Manual, 2018

[PI01]: Physiks Instrumente (PI) GmbH & Co. KG, Software Manual PZ281E, 2017

[IRS00]: Institute of Space Systems, IRS Software Git Repository, 2021, [Online]. Available: https://egit.irs.uni-stuttgart.de/